



**HAL**  
open science

# Analyse éléments finis et modèles réduits combinés à des approches flexibles de dynamique multi-corps pour la simulation de transmission par engrenages

Youness Benaïcha

## ► To cite this version:

Youness Benaïcha. Analyse éléments finis et modèles réduits combinés à des approches flexibles de dynamique multi-corps pour la simulation de transmission par engrenages. Autre. Ecole Centrale de Lyon, 2023. Français. NNT : 2023ECDL0018 . tel-04186288

**HAL Id: tel-04186288**

**<https://theses.hal.science/tel-04186288>**

Submitted on 23 Aug 2023

**HAL** is a multi-disciplinary open access archive for the deposit and dissemination of scientific research documents, whether they are published or not. The documents may come from teaching and research institutions in France or abroad, or from public or private research centers.

L'archive ouverte pluridisciplinaire **HAL**, est destinée au dépôt et à la diffusion de documents scientifiques de niveau recherche, publiés ou non, émanant des établissements d'enseignement et de recherche français ou étrangers, des laboratoires publics ou privés.



ÉCOLE  
**CENTRALE LYON**

N° d'ordre NNT : 2023ECDL0018

THESE DE DOCTORAT DE L'UNIVERSITÉ DE LYON OPÉRÉE AU SEIN DE L'ÉCOLE  
CENTRALE DE LYON

SPÉCIALITÉ Mécanique

ÉCOLE DOCTORALE MEGA  
Mécanique - énergétique - génie civil - acoustique

PAR

Youness BENAÏCHA

---

**Finite element method based analysis and  
reduced order models combined with flexible  
multibody dynamics approaches for gear train  
simulations**

---

Devant le jury composé de:

E. MIRONESCU	Professeure	ECL/MI-ICJ	Présidente
A. KAHRAMAN	Professeur	The Ohio State University	Rapporteur
J.-L. DION	Professeur	ISAE-Supméca	Rapporteur
B. GUILBERT	MCF	INSA de Lyon	Examinatrice
F. THOUVEREZ	Professeur	ECL/LTDS	Directeur
J. PERRET-LIAUDET	MCF HDR	ECL/LTDS	Co-encadrant
J.-D. BELEY	Senior director	Ansys Inc	Co-encadrant



## Abstract

---

The research work presented in this dissertation was conducted in the the Laboratory of Tribology and System Dynamics (LTDS) at Centrale Lyon, in collaboration with the company ANSYS. The work is concerned with the efficient solution of gear dynamic contact problem by means of finite element method. Finite element method are often combined with flexible multibody dynamics approaches when geometries are complex and flexible. This is a complicated problem to solve. Indeed, the main reasons are:

- The different scales involved due to micro-geometric modifications, the local behaviour (hertzian-like deformation) at the teeth, and the global behaviour of gear transmission.
- The large range of multi-frequency excitations induced by the meshing process.
- The nonsmooth mechanics caused by occurrences of unilateral contacts.
- And the high number of degrees of freedom arising from a fine mesh which is fundamental to describe accurately the previous cited reasons.

In this dissertation an insight is proposed to overcome the computational limitation experienced in the gear contact dynamics field by combining finite element based analysis with flexible multibody dynamics and model order reduction. The proposed work is applied on spur and helical gear but no assumptions are made, proposed methodologies can be applied to any type of gears. The present work focuses firstly on the definition of accurate 3D gear geometries, capable of integrating micro-geometric modifications. Then, methodologies based on finite element analysis in quasi-static condition are proposed to compute the internal excitations which are the static transmission error and the mesh stiffness. They are able to treat: gear pair with micro-geometric modifications (tip relief, crowning), gear transmission with flexible shafts and thin rimmed, gear pair with thin rimmed and holes and also a complete flexible gearbox (gear pair, shafts, bearings and the housing). An extended strategy in 2D is derived to deal fast with gear with holes. Next, reduced order models are generated using the methodology cited above. Results of gear finite element analysis in quasi-static operating condition provides snapshots of the displacement field and snapshots of the contact forces. The

collection of snapshots of the displacement field enables the generation of a reduced basis using the Proper Orthogonal Decomposition Method (POD), this basis is enhanced with free eigenmodes. The collection of snapshots of the contact force allows the creation of Krylov subspaces. These reduced order models are combined with a flexible multibody framework and the Moreau-jean time-stepping scheme (numerical integration scheme) to compute the dynamic response.

## Acknowledgements

---

This PhD thesis contains the most important results obtained during these years at the Laboratory of Tribology and System Dynamics (LTDS) and the ANSYS company. It goes without saying that this undertaking wouldn't have been possible without the support and encouragements of the people in my environment, both at and outside of work. I want to thank my supervisors from the LTDS laboratory, Prof. Fabrice Thouverez (director) and MCF HDR. Joël Perret-Liaudet (co-director) for their patient guidance and kind support during the whole project. I would like to express my sincere gratitude to Jean-Daniel Beley from ANSYS. You drew my attention to multibody dynamics, numerical methods and continuously inspired me with your ideas. You promoted my work inside the company and gave me the opportunity to join the ANSYS family, thank you for that. I want specially to thank Adrien for our discussions during the day, the night and even the week-end. You were always available to passionately exchange on model order reduction and contact dynamics, it was a pleasure to meet someone as passionate as I am on this field of research.

Last but not least, great thanks to my family members with their priceless love and continuous support, I achieved much more than I was programmed to do.



<b>Contents</b>		<b>vii</b>
<b>List of figures</b>		<b>xi</b>
<b>List of Tables</b>		<b>xvii</b>
<b>I Introduction</b>		<b>1</b>
1	Industrial and research context . . . . .	1
2	Objectives and contributions . . . . .	3
3	Thesis outline . . . . .	6
<b>II Gear transmission: state of the art</b>		<b>9</b>
1	Vibroacoustic behaviour . . . . .	10
2	Origins of the whining noise . . . . .	12
2.1	Definition of the static transmission error and the mesh stiffness . . . . .	13
2.2	Micro-geometry deviations, mounting errors, deformations . . . . .	16
2.3	Multi-scale and multi-frequency problem . . . . .	20
3	Dynamical models . . . . .	23
4	Conclusion . . . . .	28
<b>III Prediction of the quasi-static gear meshing behaviour</b>		<b>29</b>
1	Fundamental equation of motion for contact problems . . . . .	30
1.1	Equation of motion for a continuum contact problem . . . . .	30
1.2	Discretized equation of motion . . . . .	32

2	Existing strategies for the computation of the static transmission error and the mesh stiffness . . . . .	33
2.1	Methods based on the compliance computation . . . . .	33
2.2	In-line computation methods . . . . .	40
3	Proposed methodology: formulation and resolution . . . . .	43
3.1	Contact element definition . . . . .	43
3.2	Frictionless contact formulation . . . . .	45
3.3	Gear simulation with the augmented lagrange formulation . . . . .	48
4	Practical procedure . . . . .	51
4.1	Tooth generation and profile modifications . . . . .	52
4.2	Mesh convergence . . . . .	53
4.3	Time cost reduction . . . . .	56
4.4	Numerical comparison . . . . .	58
5	Conclusion . . . . .	64
<b>IV Application of the proposed methodology</b>		<b>67</b>
1	State of the art: particularity of lightweight gears . . . . .	68
2	Effect of micro-geometry and the flexibility of the transmission . . . . .	69
3	Effect of gear body with holes . . . . .	76
4	2D quasi-static decomposition method . . . . .	79
4.1	Problem formulation . . . . .	79
4.2	Numerical validations . . . . .	82
5	A parametric study of the effect of number and radial position of holes in gear blanks	88
5.1	Problem description . . . . .	88
5.2	Effect of number and radial position of holes . . . . .	89
6	Conclusion . . . . .	90
<b>V Prediction of the dynamic gear behaviour</b>		<b>95</b>
1	Model order reduction . . . . .	96

1.1	Introduction . . . . .	96
1.2	Galerkin projection based method . . . . .	98
1.3	Review of model order reduction techniques . . . . .	101
1.3.1	Modal superposition method . . . . .	101
1.3.2	Component mode synthesis method (CMS) . . . . .	104
1.3.3	Krylov subspace . . . . .	106
1.3.4	Proper Orthogonal Decomposition (POD) . . . . .	108
1.3.5	Proper Generalized Decomposition (PGD) . . . . .	111
1.4	Choice for the gear reduced order models . . . . .	112
2	Stationary dynamic response . . . . .	113
2.1	Computation procedure . . . . .	113
2.1.1	Description of the gearbox's model . . . . .	114
2.1.2	Equation of motion . . . . .	114
2.1.3	Component mode synthesis reduction . . . . .	117
2.2	Numerical strategy in the frequency domain . . . . .	118
2.3	Results and discussion . . . . .	120
3	Transient dynamic response . . . . .	123
3.1	Equation of motion of flexible multibody dynamics . . . . .	124
3.2	Proposed reduced order models . . . . .	131
3.2.1	Proper orthogonal decomposition (POD) enhanced with eigenmodes .	132
3.2.2	Krylov subspace based on the Two level Orthogonal ARnoldi algorithm (TOAR) . . . . .	140
3.3	Integration of the equations of motions for nonsmooth mechanics . . . . .	143
3.3.1	Event-driven schemes . . . . .	144
3.3.2	Time-stepping schemes . . . . .	145
3.3.3	Moreau-Jean time-stepping method . . . . .	145
3.4	Proposed strategy for the contact . . . . .	147
3.4.1	Numerical application . . . . .	149

---

4	Conclusion . . . . .	151
<b>VI General conclusion</b>		<b>155</b>
1	Conclusion . . . . .	155
2	Perspectives . . . . .	157

## List of Figures

---

II.1	Spur gear terminology from [39] . . . . .	11
II.2	Helical gear terminology from [39] . . . . .	11
II.3	Description of the line of action (a) and the plane of action (b). . . . .	13
II.4	Inclination and deviation mounting errors [125] . . . . .	17
II.5	Effect of the misalignment on the load distribution [34]. (a) no misalignment and (b) misalignment . . . . .	18
II.6	Single-flank error graph [39] . . . . .	19
II.7	static transmission error and profile correction . . . . .	21
II.8	Multi-scale problem in gear dynamics. . . . .	22
II.9	Spring-mass model of Tuplin [129] . . . . .	24
II.10	Torsional model with 2 degrees-of-freedom (a) and equivalent mass-spring model with 1 degree-of-freedom on the line of action (b) . . . . .	24
II.11	Example from [38] of lumped parameter description (a) and FE representation of the housing (b). . . . .	26
II.12	Schematic representation of transmitted contact force [128] . . . . .	26
II.13	Static contact equilibrium [15] . . . . .	27
II.14	Example of global contact shapes for the driving gear and the driven gear [15] . . . . .	28
III.1	Schematic representation of bodies in contact submitted to forces and boundary conditions	31
III.2	Non-uniform cantilever beam model of the tooth [30] . . . . .	35
III.3	Gear body induced tooth deformation as [116] . . . . .	36
III.4	Fixed surfaces (—) proposed by (a) Vedmar <i>et al.</i> [133] and (b) Chang <i>et al.</i> [28] . . . . .	37

III.5	(a) Sliced tooth and condensed substructure connection and (b) the associated discretized plane of action [54] . . . . .	40
III.6	FE model of the spur gear used in [35] . . . . .	42
III.7	8 nodes surface-to-surface contact element. . . . .	44
III.8	Description of the pure penalty method. . . . .	47
III.9	Description of the first step. . . . .	50
III.10	Description of the second step. . . . .	50
III.11	Description of the third step. . . . .	51
III.12	Flow chart of the contact procedure . . . . .	52
III.13	Description of linear tip relief deviation (a) where $S$ is the starting point, $D$ is an amount of profile modification at the tooth tip measured as the distance between point $A$ and point $F$ . Longitudinal crowning modification (b) and parameters description from the top (c). $H$ is the maximum depth of crowning. . . . .	53
III.14	(a) the spur gear mesh with low order hexahedron linear element at the tooth and tetra element elsewhere (b) close-up of the tooth mesh with 100 hexa-linear element and an inflation. . . . .	55
III.15	Unloaded transmission error for coarse mesh (50 divisions, —), intermediate mesh (70 divisions, ●) and fine mesh (100 divisions, --). . . . .	56
III.16	The static transmission error for different torque levels $T = [0.5, 15, 30, 50, 80, 100, 150, 250]$ N m and over two mesh periods. Numerical results through ANSYS Mechanical ® solver (a) and the compliance method (b). . . . .	59
III.17	STE for 150 N m with two contact positions named POS1 and POS2 (a). A close-up at the contact POS1 (b) and POS2 (c). . . . .	61
III.18	Comparison of the different peak to peak transmission error (a): —compliance method, and —ANSYS Mechanical ® solver. . . . .	62
III.19	Mesh stiffness for different torque levels $T = [15, 30, 50, 80, 100, 150, 250]$ N m: (a) ANSYS Mechanical ® solver and (b) compliance method. . . . .	63

III.20	(a) Description of the cylindrical contact stress claimed by Hertz theory, (b) shear stress for a torque of $T = 100 \text{ N m}$ and (c) a close-up of the shear stress in Pa at the middle of the tooth width is depicted. . . . .	64
IV.1	Helical gear pair. . . . .	70
IV.2	Fluctuation of the static transmission error over 4 mesh periods for an output torque $T = 115 \text{ N m}$ : (a) helical gear without longitudinal crowning, (b) helical gear with longitudinal crowning of $10 \mu\text{m}$ . . . . .	71
IV.3	Spur gears with thin rim and flexible shafts . . . . .	72
IV.4	Fluctuation of the static transmission error over 4 mesh periods for an output torque of $115 \text{ N m}$ . . . . .	73
IV.5	Contact pressure distribution on the mating teeth in Pa: (a) spur gear with thin rim and flexible shafts, (b) standard spur gear. . . . .	73
IV.6	Characteristics of the gearboxes with long shafts (a) and short shafts (b). . . . .	74
IV.7	FE models of the Gearbox with long shafts (a) and with short shafts (b). . . . .	75
IV.8	Fluctuation of the static transmission error for the two gearboxes and the gear pair only for an output torque of $115 \text{ N m}$ . . . . .	76
IV.9	Spur gear pair with holed gear blanks and large rim (a) and helical gear with holed gear blanks and thin rim (b). . . . .	77
IV.10	Fluctuation of the static transmission error of the gear pair with holes (a) and frequency spectrum (b) for an output torque $T = 115 \text{ N m}$ . . . . .	78
IV.11	Fluctuation of the static transmission error of the helical gear pair with thin rim and holes (a) and frequency spectrum (b) for an output torque $T = 115 \text{ N m}$ . . . . .	79
IV.12	Decomposition of gear pair with holes . . . . .	80
IV.13	Angular deformation retrieved at the centre of "gb" . . . . .	81
IV.14	Flow chart of the decomposition procedure . . . . .	83
IV.15	Test case 1: (a) reverse gear pair with 8 holes on driving and driven gears. Test case 2: (b) reverse gear pair with 10 holes closer to the teeth on the driven gear only. Test case 3: (c) reducer gear pair with 6 holes. . . . .	84

IV.16	Test case 1: time evolution of the STE (a) and the mesh stiffness (b) for an output torque $T = 115 \text{ N m}$ . Amplitude spectrum of STE fluctuation (c) and mesh stiffness fluctuation (d). —decomposition method, —fully flexible multibody method . . . . .	85
IV.17	Test case 2: time evolution of the STE (a) and the mesh stiffness (b) for an output torque $T = 115 \text{ N m}$ . Amplitude spectrum of STE fluctuation (c) and mesh stiffness fluctuation (d). —decomposition method, —fully flexible multibody method . . . . .	85
IV.18	Test case 3: time evolution of the STE (a) and the mesh stiffness (b) for an output torque $T = 115 \text{ N m}$ . Amplitude spectrum of STE fluctuation (c) and mesh stiffness fluctuation (d). —decomposition method, —fully flexible multibody method . . . . .	86
IV.19	Schematic representation of the holed configuration . . . . .	89
IV.20	Time evolution of the STE and the mesh stiffness for an output torque $T = 20 \text{ N m}$ : (a,b) standard gear, (c,d) case 8R34, (e,f) case 10R34, (g,h) case 6R30, (i,j) case 8R30, (k,l) case 8R27. . . . .	92
IV.21	Time evolution of the STE and the mesh stiffness for an output torque $T = 115 \text{ N m}$ : (a,b) standard gear, (c,d) case 8R34, (e,f) case 10R34, (g,h) case 6R30, (i,j) case 8R30, (k,l) case 8R27. . . . .	93
V.1	Description of the tooth contact point. . . . .	100
V.2	Description of the line of action (a) and the plane of action (b). . . . .	116
V.3	(a,b) represents the static transmission error and mesh stiffness fluctuations for the short gearbox (see IV.7b). (c,d) represents the static transmission error and mesh stiffness fluctuations for the long gearbox (see IV.7a). . . . .	122
V.4	Dynamic response of the gearbox for the full model (●) and the CMS reduced model (—) for an output torque $T = 115 \text{ N m}$ . . . . .	123
V.5	Dynamic response of the short gearbox (—) and the long gearbox (—) for an output torque $T = 115 \text{ N m}$ . . . . .	124
V.6	Schematic representation of a multibody system. . . . .	125
V.7	Schematic representation of flexible multibody systems . . . . .	127
V.8	Example of the first contact mode shape ( $f_1 \approx 10^5 \text{ Hz}$ ) . . . . .	133

V.9	Example of the gear body mode shape of a thin rimmed gear with holes ( $f_1 \approx 3270$ Hz)	133
V.10	Example of the displacement field at a given driving angle $\theta_1$ . (a) total displacement, (b) displacement in x direction, displacement in y direction. . . . .	134
V.11	(a) Auto-correlation matrix representation of 100 snapshots (b) POMs energy chart for the output gear. . . . .	137
V.12	Example of the first five POMs. (a) POMs 1, (b) POMs 2, (c) POMs 3, (d) POMs 4 and (e) POMs 5. . . . .	138
V.13	Summary of the strategy for the POD method. . . . .	139
V.14	Example of eigenmodes. . . . .	139
V.15	Example of the field of contact forces for a given position of the driving gear (a) and another position (b) . . . . .	141
V.16	Auto-correlation matrix representation for the contact forces. . . . .	142
V.17	Summary of the strategy for the krylov subspaces. . . . .	144
V.18	Schematic representation of the RBF interpolation of the reduced basis at the contact points. . . . .	149
V.19	Summary of the complete procedure. . . . .	150
V.20	Dynamical gear pair model with the fictitious body. . . . .	150
V.21	Comparison of the fluctuation of the static transmission error of the POD reduced model (—) and the full model (—). . . . .	151
V.22	Fluctuation of the dynamic transmission error for the POD reduced model. . . . .	152



## List of Tables

---

II.1	Frequency content of the static transmission error and the mesh stiffness. . . . .	20
III.1	Characteristics of the spur gear . . . . .	55
III.2	Parametric study on spur gear to reduce the time cost . . . . .	57
III.3	Comparative study on spur gear with Hertz theory . . . . .	65
IV.1	Gear characteristics of the helical gear pairs. . . . .	71
IV.2	Gear characteristics of the spur gear with thin and flexible shafts. . . . .	72
IV.3	Gear characteristics of the spur gear with holed gear blanks. . . . .	77
IV.4	Gear characteristics of the helical gear pair with holed gear blanks and thin rim. . . . .	78
IV.5	Gear characteristics of the different test cases . . . . .	84
IV.6	STE and mesh stiffness comparisons between the fully flexible multibody method and the decomposition method . . . . .	87
IV.7	Gear pairs with holes retained according to the number of holes $N_h$ and their radial position R . . . . .	89
V.1	Characteristics of the radial stiffness elements . . . . .	114





**Contents**

---

1	Industrial and research context . . . . .	1
2	Objectives and contributions . . . . .	3
3	Thesis outline . . . . .	6

---

**1 Industrial and research context**

Gears are used in many systems to transmit the torque and rotational motion generated by the engine. A gear transmission consists of toothed wheels mounted on shafts. These shafts are supported by bearings. All of these mechanical components are usually assembled in a housing that supports the bearings and contains the lubricant. Gears are currently the most suitable technological solution for transmitting high power. They allow to minimize the transmission defects and they have a high efficiency. Geared systems are thus widely spread in the field of transportation.

Research efforts over the last thirty years have led to progress in the understanding of geared mechanisms. Indeed, the vibratory response of gear transmissions is mainly generated by internal excitations which are related to the meshing process. These internal excitations are the transmission (TE) error and the mesh stiffness. The transmission error is defined as the difference between the actual position

of the output gear and the position it would occupy if the gear pair were perfectly conjugate. The mesh stiffness is the result of the periodic variation of the number of pair of teeth in contact. As a consequence, these excitations produce dynamic mesh forces which are transmitted to the housing through wheel bodies, shafts and bearings. The vibratory state of the housing is related to the radiated noise. The gear dynamics remains complex to model as the global behaviour of the whole transmission and the local behaviour at the gear mesh are coupled. It's thus of paramount importance to propose models that enable the inclusion of the gear body, the flexible shafts, the bearing and the housing during the computation of the transmission error and the mesh stiffness.

Additionally, the issues related to energy consumption and air pollution have increased the need for on-board mass reduction. This requirement concerns in particular drivelines equipped with gear transmissions. The proposed solutions to decrease the gear mass consists in using composites or removing material from the gear blanks by employing thin rim or holes. However, mass reduction may compromise the integrity of the structure and the vibroacoustic performances. Thus, it is of paramount importance to verify that adding holes does not increase the gear mesh excitation and the resulting radiated noise.

The work of the PhD is part of a collaboration between the Laboratory of Tribology and System Dynamics (LTDS, <http://ltds.ec-lyon.fr/spip/>) and the publisher of numerical simulation software ANSYS (<http://www.ansys.fr/>). It is to take advantage of the experience of the LTDS team in the field of simulation of mechanical geared systems in a commercial simulation environment developed by ANSYS.

## 2 Objectives and contributions

The main goal of the collaboration is to simulate the temporal dynamic behavior of complete gear transmissions for stationary operating speeds as well as for transient regimes. To do this, we develop modelling strategies based on a coupling between a global multibody transient model at the scale of the complete transmission and local models of the close contact between teeth. These modeling approaches will be based on the numerical tools developed by ANSYS (finite element solver, multi-body dynamics solver). In this context, it will then be necessary to develop temporal integration methods coupled with model reduction methods capable of managing this coupling at different spatial scales. The targeted methodologies must yield reliable results and low computational time.

The first contribution of this work is the development of a complete finite element methodology to characterize the internal excitations which are the static transmission error and the mesh stiffness without any assumption of the contact point locations. Indeed, the instantaneous contact conditions between the gear teeth are determined and solved at each time step. The micro-geometry (of the order of a few micrometers) is directly introduced during the gear geometry generation. This methodology is achieved using the ANSYS Mechanical<sup>®</sup> solver and relies on an augmented lagrangian formulation considering a surface-to-surface contact detection for describing the contact. The methodology has been firstly compared with classical methods on a gear pair and then it was applied to gear pair with thin rimmed and holes and even to complete gearboxes.

The next contribution is the development of a numerical strategy to compute the static transmission error and the mesh stiffness of 2D gears with holed gear blanks. The instantaneous deformation of the holed gear blank and the gear teeth is estimated by decomposing the gear pair with holed gear blanks

into two substructures. a substructure including the gear without holes, with solid wheel bodies, noted 'wh' and a substructure including only the wheel body with holes, without the teeth, noted 'gb'. In particular, the substructure 'wh' represents the gear where the wheel body with holes is replaced by a rigid disk, in order to calculate only the static deformation of the teeth. A non-linear quasi-static analysis is performed over one meshing period, thus a small angular displacement, to evaluate the static deformation of the teeth along the line of action. The contributions of the gears and the wheel body are then summed to obtain the total transmission error

Another contribution is the development of a methodology in the ANSYS environment to compute the dynamic behaviour of large scale geared systems. The proposed methodology relies on the use of a condensed model for the flexible shafts, the bearings and the housing while considering parametric excitations (static transmission error and mesh stiffness) to model the contact between the gear teeth. The numerical strategy consists in solving the equation of motion in the frequency domain using the Harmonic Balance Method (HBM).

Then, last but not least contribution is the development of strategies based on reduced order models coupled to a flexible multibody framework to compute the gear dynamic response. Reduced order models based on POD firstly and then Krylov subspaces are devised. The reduced model is then introduced in a multibody framework for solving the equation of motion. The nonsmooth dynamics is integrated with a Moreau-Jean time stepping scheme and a FE-based contact formulation is considered at each time step using Signorini conditions at velocity level.

The work provided during this Phd has allowed several articles in international journals:

1. Y. Benaïcha, J. Perret-Liaudet, J-D. Beley, F. Thouverez. On a flexible multibody modelling approach using FE-based contact formulation for describing gear transmission error. *Mechanism and Machine Theory*, 167(1142):104505, 2022. <https://doi.org/10.1016/j.mechmachtheory.2021.104505>
2. Y. Benaïcha, A. Mélot, J. Perret-Liaudet, J-D. Beley, E. Rigaud, F. Thouverez. A decomposition method for the fast computation of the transmission error of gears with holes. *Journal of Sound and Vibration*, 532 :116927, 2022. <https://doi.org/10.1016/j.jsv.2022.116927>
3. A. Mélot, Y. Benaïcha, E. Rigaud, J. Perret-Liaudet, F. Thouverez. Effect of gear topology discontinuities on the nonlinear dynamic response of a multi-degree-of-freedom gear train. *Journal of Sound and Vibration*, 516 :116495, 2022. <https://doi.org/10.1016/j.jsv.2021.116495>
4. H. André, Q. Leclère, D. Anastasio, Y. Benaïcha, K. Billon, M. Birem, F. Bonnardot, Z.Y. Chin, F. Combet, P.J. Daems, A.P. Daga, R. De Geest, B. Elyousfi, J. Griffaton, K. Gryllias, Y. Hawwari, J. Helsen, F. Lacaz, L. Laroche, X. Li, C. Liu, A. Mauricio, A. Mélot, A. Ompusunggu, G. Paillot, S. Passos, C. Peeters, M. Perez, J. QI, E.F. Sierra-Alonso, W.A. Smith, X. Thomas. Using a smartphone camera to analyse rotating and vibrating systems: Feedback on the SURVISHNO 2019 contest. *Mechanical Systems and Signal Processing*, 154 :107553, 2021. <https://doi.org/10.1016/j.ymsp.2020.107553>

The works have been presented in international conferences:

1. Y. Benaïcha, J. Perret-Liaudet, J-D. Beley, F. Thouverez, E. Rigaud. Some results about multibody modelling for describing gear dynamics including meshing teeth contact. *International Nonlinear Dynamics Conference*, Roma, Italy, 2019

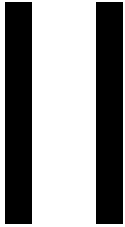
### 3 Thesis outline

The present manuscript is divided into five chapters. The content of each chapter is described as follows:

- The first chapter is this introduction.
- Chapter II is a literature review on the vibroacoustic behaviour of gears with a focus on the whining noise. We introduce the main concepts and the different phenomena in gear dynamical system. Then, dynamical models used to simulated gear dynamics in the literature are described.
- Chapter III provides a review of existing strategies for the computation of the static transmission error and the mesh stiffness. After that, a proposed methodology based on a complete finite element approach is described. The approach uses FE-based contact and augmented lagrange formulation to treat the instantaneous gear teeth contact conditions.
- Chapter IV is an application of the methodology proposed in Chapter III. The application treats the case of lightweight gears (holed gear blanks) and complete gearboxes. Then, a 2D quasi-static decomposition method is derived to accelerate the computation of the static transmission error and the mesh stiffness of gears with holed gear blanks.
- Chapter V starts with the state of the art of model order reduction techniques in a structural dynamic context. Firstly, a model of a complete gearbox is proposed. The gearbox is submitted to the internal excitations (STE and mesh stiffness fluctuations) and the flexible shafts, the

bearings and the housing are condensed using the CMS. The stationary dynamic response is obtained by solving the equation of motion in the frequency domain with the Harmonic Balance Method (HBM). Then, reduced order models based on Proper Orthogonal Decomposition (POD) and Krylov subspaces are devised. A flexible multibody framework is then used to compute the transient gear dynamic response of a gear pair.





## Introduction

---

The objective of this chapter is to present the state of the art of the vibroacoustic behaviour of gears with a focus on the whining noise. The gear dynamic behaviour is responsible for different radiated noise. Firstly, these noises are classified according to the gear dynamic regime. Then, we define and introduce the excitation sources of geared systems and the several gear parameters that influence the excitation sources. The dynamical phenomena occurring in geared systems are detailed. Finally, a clear description of the dynamical models used to simulate the vibratory behaviour of gear transmission is proposed.

---

## Contents

---

1	Vibroacoustic behaviour . . . . .	10
2	Origins of the whining noise . . . . .	12
2.1	Definition of the static transmission error and the mesh stiffness . . . . .	13
2.2	Micro-geometry deviations, mounting errors, deformations . . . . .	16
2.3	Multi-scale and multi-frequency problem . . . . .	20
3	Dynamical models . . . . .	23
4	Conclusion . . . . .	28

---

## 1 Vibroacoustic behaviour

Gears are components used in most types of machinery. They have been used by almost all machine designers since the last three thousand years. They still continue to be an important component in current machines. Besides, gear design aims at constantly improving the efficiency and the power of gear machinery. To this end, designers have to propose ever more lighter and quieter gears. Gears are toothed wheels that transmit rotation and torque from one part of the machinery to another. Gears are used in pairs or more, for e.g. planetary gear train, and each gear is attached to a shaft. The gear meshing process enables the power transmission from the input shaft to the output shaft. Their design can regulate the rotational velocity and the torque of a mechanism. We can thus find different type of gears. The most common gears are spur gears, helical gears, worm gears, bevel gears and hypoid gears. Spur gears are the simplest to design and manufacture (cylindrical shape). The teeth are parallel to the shaft axis and they run straight across the width of the gear face. Worm gears consist of a worm screw and a worm wheel (spur gear). The rotational axis is changed by  $90^\circ$  between the input and the output axis. Helical gears have tooth oriented with an angle to the shaft called the helix angle. As opposed to spur gears, helical gears have contact which starts at one end of a tooth and extends gradually in a diagonal line across the width of the tooth. Bevel gears have straight teeth and they are manufactured on a conical shape rather than a cylindrical shape as used for spur gears. They transmit rotation and torque from one shaft to a nonparallel shaft (mostly perpendicular). Hypoid gears are bevel gears with helical teeth. The straight teeth of spur gears and straight bevel gears tend to make them noisy in operation, since the mating teeth mesh along their whole width all at once. In this manuscript we will focus on spur and helical gears but the proposed method are not restrictive because no assumption is made about the gear type. Thus, an application on bevel gears and hypoid

gears is possible. The gears characteristics of spur and helical gear transmitted power through parallel shafts are described in Fig. II.1 and Fig. II.2.

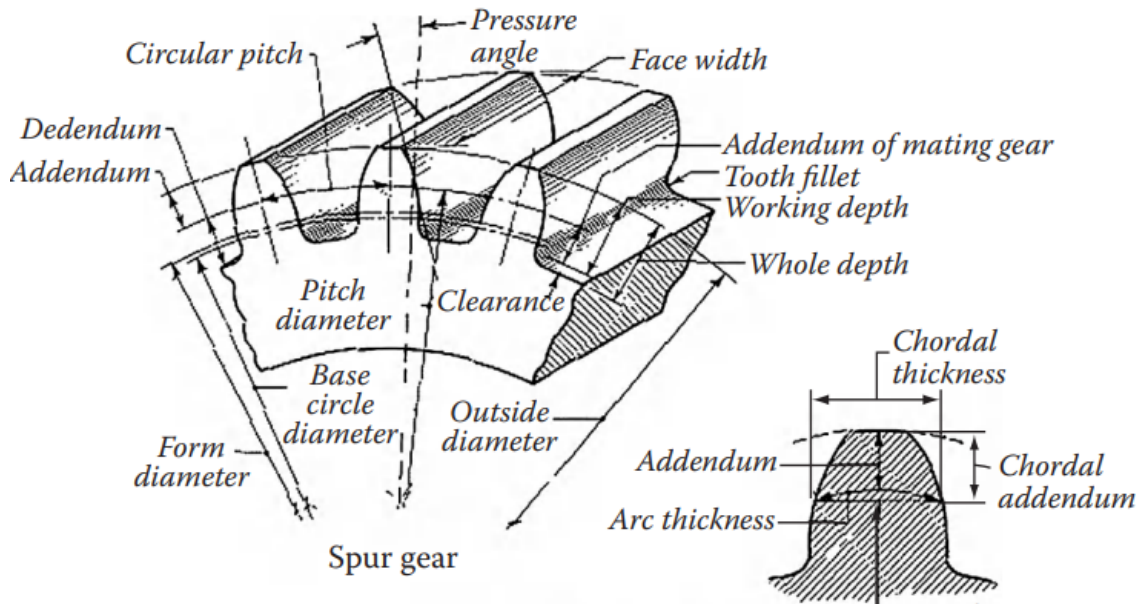


Figure II.1: Spur gear terminology from [39]

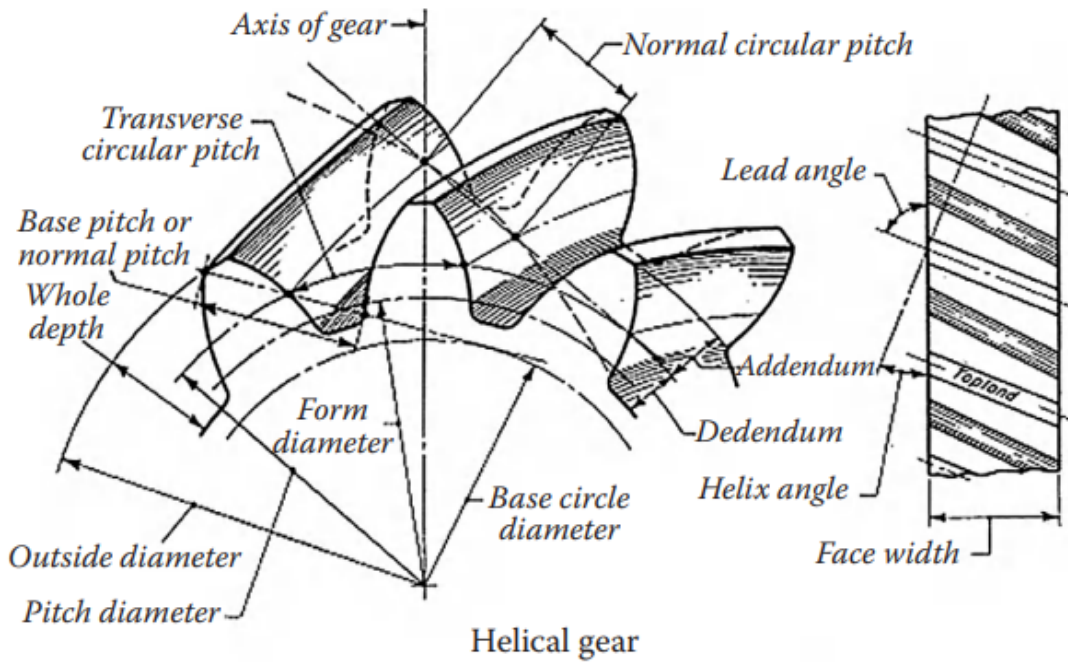


Figure II.2: Helical gear terminology from [39]

In practice, gears are used not only in pairs, but also in more complex mechanisms called gear trains. Gear trains have vibroacoustic behaviours. The vibroacoustic behaviour is related to the operating conditions and the type of the excitation sources. The dominant resulting noise related to the meshing process is the whining noise. Generally, the whining noise constitutes the dominant source of noise [22, 105, 115, 142]. For example, in the transportation industry, the whining noise corresponds to a large part of the noise perceived by passengers as well as the noise perceived outside the vehicle. Gear whining noise is perceived as a tonal noise that is emitted from gears in mesh and the sound is characterized by vibrations at gear mesh frequency and its multiples (harmonics). This is an annoying noise since the human ear is more sensitive to tonal noise.

In this context, one common goal to improve NVH is to obtain quiet gear systems by reducing the whining noise level. This structure-borne noise results from the dynamic mesh force, corresponding to the time varying normal contact force. Vibrations propagate through the gear wheel bodies, the shafts and the bearings to the housing. The objective of the works in this manuscript is to propose modelling approaches for a better computation of the whining noise. In this part we thus focus on the origins and dynamic behaviour of the whining noise.

## 2 Origins of the whining noise

In this section, we describe the origins of the whining noise. During the gear mesh, the gear is submitted to different internal excitation sources. These excitation sources are the static transmission error and the mesh stiffness. It is well known that the STE and the mesh stiffness are responsible for the whining noise. Thus modifications on the STE and the mesh stiffness have an influence on the whining noise. So, the effects of micro-geometry modifications, mounting errors and loaded tooth deformation on the STE and the mesh stiffness are highlighted in the second part of this section. The work of Harris [61], later assisted by Munro [46], deserves to be cited in the references because of its

fundamental contribution to the understanding of the sources of gear meshing vibrations. In his work Harris showed that what he called static error is affected by profile modifications that he introduced deliberately. He investigated the influence of the profile modifications on the static behaviour of the meshing gears.

## 2.1 Definition of the static transmission error and the mesh stiffness

The transmission error is defined as the difference between the actual position of the output gear and the position it would occupy if the gear pair were perfectly conjugate [64, 142]. This physical quantity is usually expressed as an angular error between the input and the output gear or as a displacement along the line of action. The line of action is the line tangent to the base circles along which theoretical contact points are located. The line of action for spur and helical gears and the associated plane of action are described in Fig. II.3.

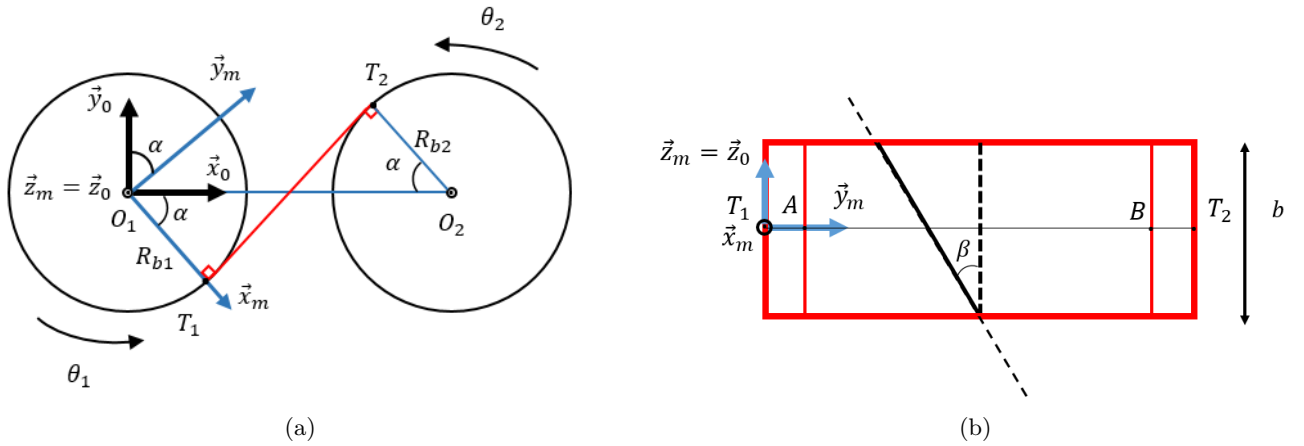


Figure II.3: Description of the line of action (a) and the plane of action (b).

The transmission error can be expressed along the line of action as:

$$\delta(\theta_1) = R_{b2}\theta_2 + R_{b1}\theta_1 \quad (\text{II.1})$$

$\theta_1$  and  $\theta_2$  are respectively the angular position of the input wheel and the output gear.  $R_{b1}$  and  $R_{b2}$  are the base radii of the input wheel and the output gear.  $\alpha$  and  $\beta$  are the operating pressure

angle and the operating helix angle, respectively. The definition in eq II.1 is well suited for two gears meshing together but when a complete gearbox is considered the effects of flexible shafts, bearings and the housing are to be taken into account. For this reason, the transmission error is expressed using a geometrical column vector  $\mathbf{G}$  in the reference frame  $(O_1, \vec{\mathbf{x}}_0, \vec{\mathbf{y}}_0, \vec{\mathbf{z}}_0)$  associated with the gear design parameters. This vector  $\mathbf{G}$  as defined below has 12 non-zero values that couple the 6 degrees-of-freedom of the input gear with the 6 degrees-of-freedom of the output gear:

$$\mathbf{G} = \begin{bmatrix} \sin(\alpha) & \cos(\alpha) & \tan(\beta) & 0 & \frac{-R_{b1}\tan(\beta)}{\cos(\alpha)} & R_{b1} & -\sin(\alpha) & -\cos(\alpha) & -\tan(\beta) & 0 & \frac{-R_{b2}\tan(\beta)}{\cos(\alpha)} & R_{b2} \end{bmatrix} \quad (\text{II.2})$$

the transmission error which takes into account the contribution of all the component of the transmission is expressed as follows:

$$\delta_s(\theta_1) = \mathbf{G}^T \mathbf{x} \quad (\text{II.3})$$

with

$$\mathbf{x} = [x_1 \ y_1 \ z_1 \ \psi_1 \ \phi_1 \ \theta_1 \ x_2 \ y_2 \ z_2 \ \psi_2 \ \phi_2 \ \theta_2] \quad (\text{II.4})$$

where  $[x_1 \ y_1 \ z_1 \ \psi_1 \ \phi_1 \ \theta_1]$  and  $[x_2 \ y_2 \ z_2 \ \psi_2 \ \phi_2 \ \theta_2]$  are the 6 degree-of-freedom of the input and output gear, respectively. Sometime it can be useful to define the transmission error in terms of velocity and acceleration. For that,  $\mathbf{x}$  is replaced by  $\dot{\mathbf{x}}$  and  $\ddot{\mathbf{x}}$  for the velocity and the acceleration, respectively. Actually, the type of analysis will drive the choice of transmission error definition. Indeed, the physical quantity which characterizes correctly the transmission error when the gear pairs operates in static or quasi-static is the position  $\mathbf{x}$ . However, the velocity and the acceleration  $\dot{\mathbf{x}}$  and  $\ddot{\mathbf{x}}$  seems to be more adapted in dynamic operating conditions. It's also difficult to retrieve experimentally the displacement and the velocity, generally we have access to acceleration thanks to accelerometers. So, one can see that the transmission error is characterized by the operating condition regime. A clear description has been proposed over the years. A brief reminder is presented below:

***The kinematic or unloaded static transmission error:*** This kinematic static transmission error considers rigid gears or unloaded gears which operates in static or quasi-static behaviour. So, only the effect of the geometry is accounted for.

***The loaded static transmission error:*** In addition to the kinematic static transmission error, the loaded static transmission error takes into account the teeth flexibility and the teeth are loaded. So, the geometry, the tooth deformation and the global deformation are included.

***The dynamic transmission error:*** Considering the elasto-dynamic properties, the dynamic transmission error is the transmission error in dynamic operating condition.

The static transmission error depends on the instantaneous tooth position and has for origins :

- manufacturing errors (eccentricity, pitch error, profile error) [57, 151].
- intentional micro-geometry deviation (longitudinal crowning, profile correction) [64, 88, 78, 154].
- tooth deformation (hertzian contact, tooth bending and shear), and global deformations of the entire gearbox (housing) which induce shafts misalignment [125].

The STE can be seen as a displacement excitation. These main parameters influencing the STE are detailed in the next section.

Another important element for the whining noise is the internal parametric excitation source generated by the meshing stiffness fluctuation. Indeed, the peak-to-peak amplitude of its periodic variation at the meshing frequency is large. The origin of this periodic variation is due to the variation of the

number of teeth in contact during the meshing process. The periodic variation can reach 65% of its mean value for spur gears, and 40% for helical gears. This internal excitation is deduced from the STE computation as it consists on the slope of the function of the transmitted force versus the STE. This characteristic results from a linear approximation of the transmitted mesh force function. For each driving angular position  $\theta_1$ , the mesh stiffness is defined as the derivative of the transmitted load  $F$  relative to the STE  $\delta(\theta_1)$ :

$$k(\theta_1) = \frac{\partial F}{\partial \delta(\theta_1)} \quad (\text{II.5})$$

The mesh stiffness is a parametric excitation which exhibits the same frequency components as the STE fluctuation. The STE and the mesh stiffness are leading the system to be parametric.

## 2.2 Micro-geometry deviations, mounting errors, deformations

As introduced previously, the transmission error and the mesh stiffness are generated by the tooth deformation. These physical quantities are also impacted by manufacturing errors, micro-geometry deviations and global deformations. The main factors impacting the transmission error and the mesh stiffness are presented below:

***Eccentricity***: the eccentricity is defined as the deviation between the actual axis of rotation and the theoretical. This is a well known defect impacting the transmission error. Many authors showed the effects on the transmission error over the last 30 years considering the eccentricity on one wheel firstly [98], then with an eccentricity on the two wheels [94, 85]. They showed the addition of harmonics at the rotating frequency of the considered wheel  $f_{1,2}$ . Welbourn [142] characterize the eccentricity by the presence in the frequency spectrum of the rotating frequency of the considered wheel  $f_{1,2}$  and sidebands around mesh harmonics  $nf_m \pm f_{1,2}$  with  $f_m$  the mesh frequency and  $n \in \mathbb{N}^*$ .

**Shaft misalignment:** shaft misalignment with respect to the plane of the shafts includes inclination and deviation [125], they are mostly characterized by the angular errors  $\theta_i$  and  $\theta_d$ , for which  $i$  and  $d$  state for inclination and deviation error, respectively. It is due to mounting errors of the wheel, the shafts and the bearings. This defect generates a modification of the contact pattern and the pressure distribution. These modification have a significant influence on the mesh stiffness. Conry *et*

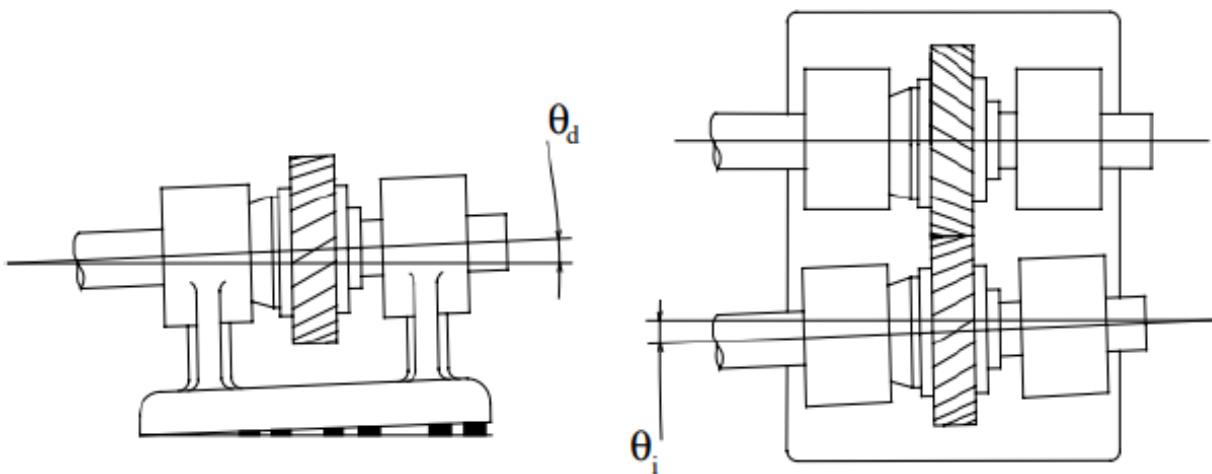


Figure II.4: Inclination and deviation mounting errors [125]

*al.* showed the effect of the misalignment on the pressure distribution [34].

**Pitch error:** pitch error is described as the difference between the angular position of one tooth and its theoretical angular position. Generally, pitch error corresponds to the distance between the actual profile and the theoretical. This error comes from the manufacturing process. Welbourn [142] and Munro [99] represent pitch error by a Gaussian distribution and it appears in the frequency spectrum of the transmission error, an order at the rotating frequency and its harmonics.

**Profile error:** profile error is the deviation of the involute tooth profile from the theoretical involute

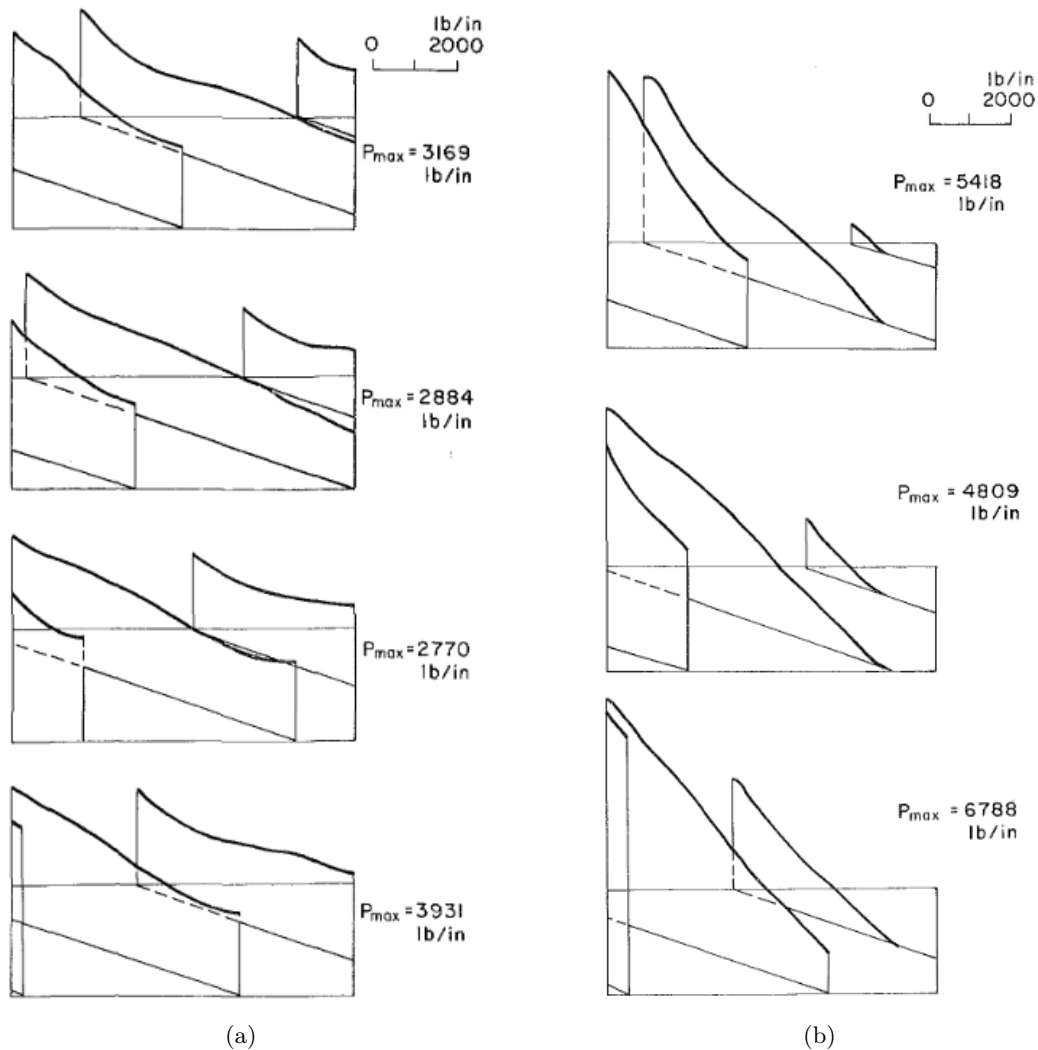


Figure II.5: Effect of the misalignment on the load distribution [34]. (a) no misalignment and (b) misalignment

tooth profile. Munro (1967), Welbourn (1979), Mark (1978) and Randall (1982) identified the presence of profile errors on the gear teeth. Profile errors induce frequency content at the mesh frequency and its harmonics on the transmission error. Fig. II.6 shows an example of profile error measurements for several mesh periods.

The unloaded static transmission error is generated by the previous errors (eccentricity, misalignment, pitch error, center distance error and profile error). This quantity is thus directly connected to the

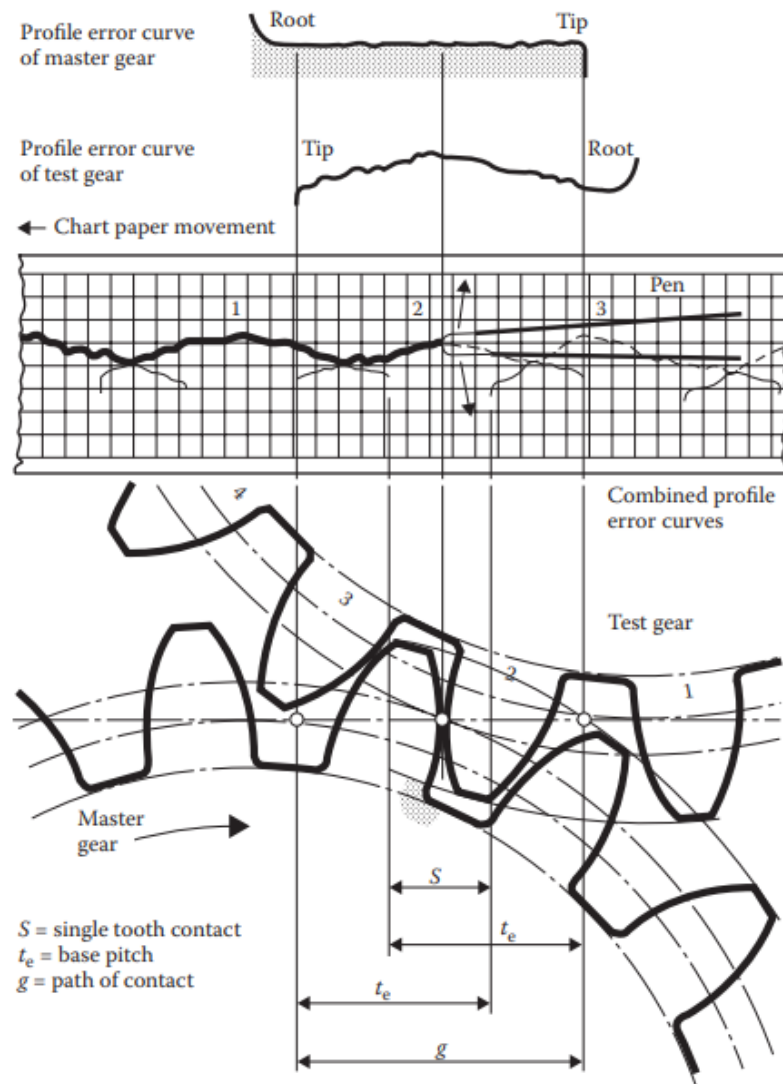


Figure II.6: Single-flank error graph [39]

assembly of the gear transmission and the quality of gear tooth manufacturing. When the gear pair is loaded with a medium or high torque, the deformation of the teeth and the gear body and the global deformation of the transmission including shafts, bearing and the housing are added to the micro-geometric error to form the loaded transmission error. The tooth deformation is the same order of the micro-geometric deviation, typically, for a module  $m = 2\text{mm}$  the micro-geometric deviation is about  $10\mu\text{m}$ . The micro-geometry deviation modifies the position of the contact points. The fluctuations of this transmission error and the mesh stiffness are the excitation sources of the whining

noise. The objective of many studies is therefore to minimize these fluctuations by introducing intentionally optimal micro-geometric deviation. Harris [64] introduced what he called "design load" which represents the torque for which the static transmission error is minimized. Harris showed in Fig. II.7, for a chosen gear pair, the variation of the transmission error by increasing the torque. This "Harris map" enables fundamental contribution to the understanding of the sources of gear meshing behaviour. Additionally, the static transmission error and the mesh stiffness are periodic and related to the instantaneous contact conditions. The frequency content is thus rich and large as shown in Table II.1.

Table II.1: Frequency content of the static transmission error and the mesh stiffness.

Frequencies	Sources
rotating frequency $f_{1,2}$	eccentricity
harmonics of rotating frequency $nf_{1,2}$ with $n \in \mathbb{N}^*$	eccentricity and pitch error
mesh frequency $f_m$ and harmonics	teeth deformation, profile error and misalignment
sidebands around mesh harmonics $nf_m \pm f_{1,2}$	modulation due to eccentricity

At this stage, we can understand the complexity for predicting the whining noise. Indeed, we deal with micro-geometric deviations which are the order of the tooth deformation and at the same time the tooth deformation is coupled with the global deformation of the gear transmission, especially the shafts and the housing. Moreover, a large frequency content has to be considered. The choice of the model for determining the internal excitations (STE and mesh stiffness) is thus of paramount importance.

### 2.3 Multi-scale and multi-frequency problem

Generally, the whining noise constitutes the dominant source of noise. This structure-borne noise results from the dynamic mesh force, corresponding to the time varying normal contact forces. Vibrations propagate through the gear wheel bodies, the shafts and the bearings to the housing.

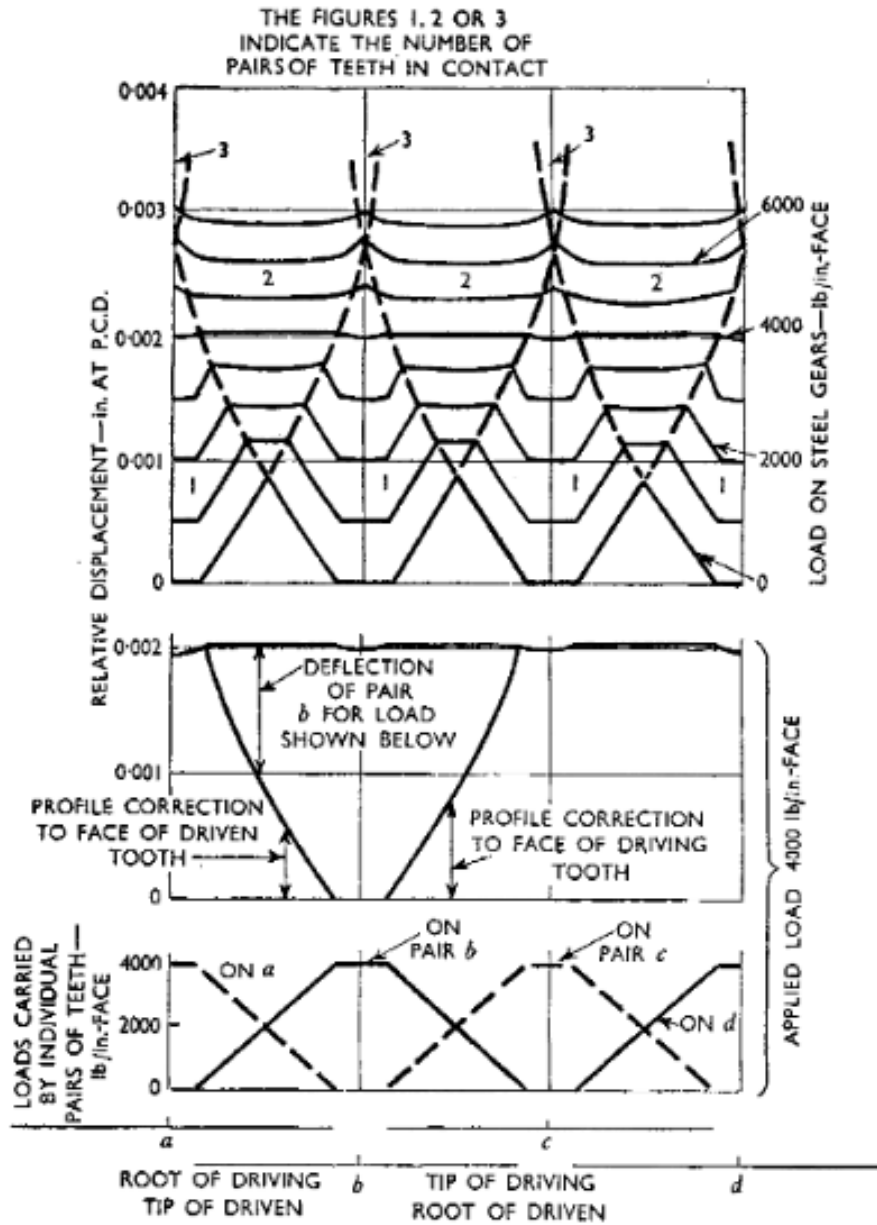


Figure II.7: static transmission error and profile correction

The vibratory state of the latter is responsible for the radiated noise. So, the gear pair (teeth and gear body), shafts, bearing and the housing are involved during vibroacoustic process. Thus, gear dynamic is a multi-scale problem. Fig. II.8 specifies the different scale involved for a gear dynamic operation.

The dynamic behaviour of gear systems is also a multi-frequency problem. As shown in the previous

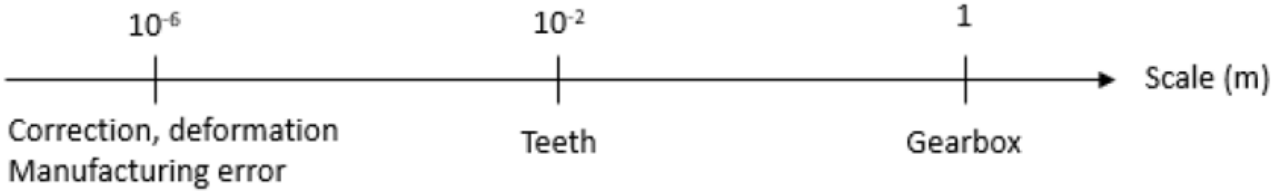


Figure II.8: Multi-scale problem in gear dynamics.

section, the static transmission error and the mesh stiffness are periodic quantities and the study of their spectrum put forward the large frequency range exciting the system. Besides, the convolution of the static transmission error and the mesh stiffness generates additional harmonics in the dynamic response. The vibratory response is thus multi-frequency response for a parametric system submitted to harmonic excitation including a constant static output torque. Additionally, the mesh stiffness is responsible for parametric instabilities (free response) and resonances (forced response). These parametric phenomena consists of an increase of the vibration amplitudes. The parametric instabilities correspond to the free response of the transmission. These instabilities are possible when the mesh frequency is:

$$f_m = \frac{1}{n}(f_i + f_j) \quad (\text{II.6})$$

with  $n \in \mathbb{N}^*$  and  $f_i$  and  $f_j$  the natural frequencies of mode  $i$  and  $j$ , respectively. The parametric resonances correspond to the forced vibratory response. For a given excitation frequency  $f$ , the parametric resonance occur when the mesh frequency is:

$$f_i = f \pm n f_m \quad (\text{II.7})$$

with  $n \in \mathbb{N}^*$  and  $f_i$  the natural frequencies of mode  $i$ . Similarly to parametric resonances, an increase of the vibration amplitudes can occur for critical operating regime and critical modes. The critical modes which are the modes for which the strain energy contribution at the mesh is maximum are governed by the mean value of the mesh stiffness and the compliance of the other component of the

transmission.

So, the different scale involved in the meshing process and the large frequency content of the response makes the gear dynamic complex to model. Below, a brief presentation of the dynamical models mostly used in the literature for cylindrical gears are presented.

### 3 Dynamical models

This section reminds the dynamical models used over the year in the literature to simulate the vibratory behaviour of cylindrical gear transmission. Modeling gear transmission has been studied for many years and fundamental studies (Özgüven [156], Rémond [114], Wang [140]) attest to the numerous works done on the subject. It is necessary to complete them with more recent works, in particular on the modeling by finite elements. It appears from these literature syntheses that several levels of modeling have been considered to simulate the dynamic behavior of a transmission according to the needs of the study and the simulation means. For instance, simulate the root stress, the hertzian shear stress in the contact, the tooth wear, the vibrations and the acoustic radiation.

One of the first relevant model were introduced by Tuplin [129] in 1950's. This model considers only the flexibility of the teeth. Indeed, the input and output gears are modelled by rigid masses and a constant stiffness is used to represent the teeth flexibility (see Fig. II.9). Tuplin's model has been improved until pure torsional models (2 degrees-of-freedom) and its equivalent mass-spring model on the line of action (1 degree-of-freedom). These models (see Fig. II.10) neglect the "bending - torsion" couplings. They are limited to studies in the plane of action of the gear. The pure torsion model corresponds to 2 degrees of freedom where the two wheels are represented by two rotational inertia linked by a torsional stiffness. These models are still widely used in the literature.

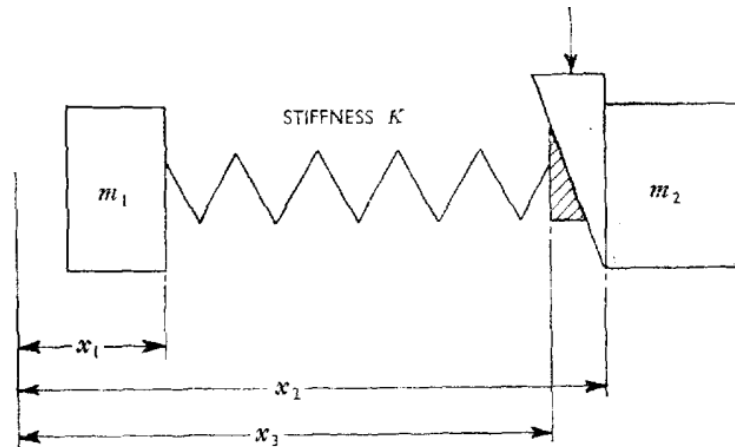


Figure II.9: Spring-mass model of Tuplin [129]

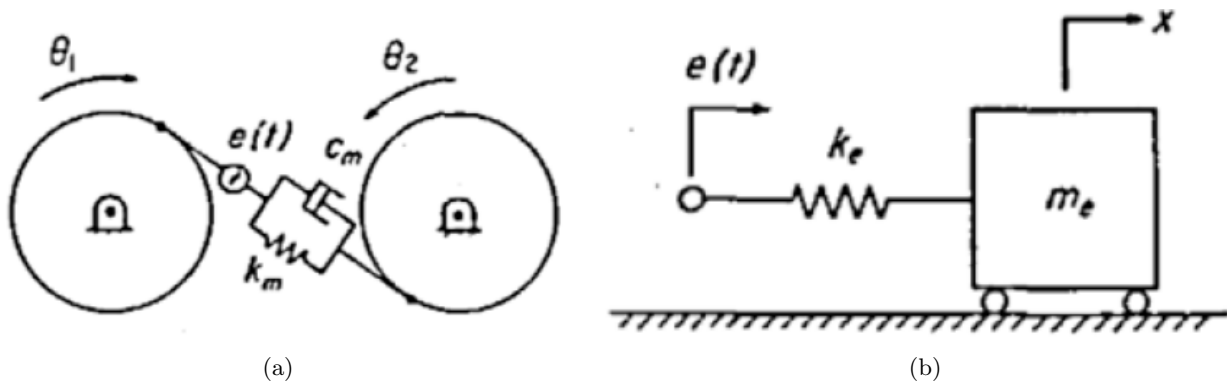


Figure II.10: Torsional model with 2 degrees-of-freedom (a) and equivalent mass-spring model with 1 degree-of-freedom on the line of action (b)

In the literature, nobody deals directly with the continuum mechanics for modelling gears. Most of the time finite element method are used to discretized the equation of motion. From the 60's with the increase of the computational resources, some more general models appear. These models tried to take into account the flexibility of the shafts, the bearings and the housing. These models can be classified as lumped parameter models and models combining lumped parameter with finite elements.

Lumped parameter models include the flexibility of other components: These are models with a small number of degrees of freedom which are relatively convenient to implement and fast to compute. As opposed to pure torsional model, these models increased the number of degree of freedom to

represent the desired phenomena. In this type of simplified modeling, a large part of the work lies in the definition of the coupling between the wheels. Several approaches are possible. The first one consists in modeling the coupling by a constant stiffness. This approach used by Vinayak [136, 137] or Kahraman and Singh [79] allows to determine the natural frequencies of a transmission by considering an average mesh stiffness. An application to planetary gear is proposed by Kahraman [77]. Planetary gears have been the subject of other works such as those of Lin and Parker [93]. However, considering the mesh stiffness as constant is very limiting because it means neglecting an important source of internal excitation. Improved models used therefore time varying mesh stiffness for the coupling.

Models combining lumped parameter with finite elements: These models make it possible to overcome the deficiencies of the pure lumped models presented previously by taking into account all the degrees of freedom of the transmission and thus the couplings between the bending and torsional vibrations of the shafts and their supports. In addition, these models allow the introduction of all the elements of the transmission such as shafts and bearings to reproduce more precisely the deformations as well as the interactions between them and the gears as shown in Fig. II.11. Examples include the models used Kahraman and Ozguven [81], Perret-Liaudet [108] and Rigaud [112]. In general, gears are modeled by rigid solids and their motion is parametrized by 6 degrees of freedom. The mesh stiffness is introduced to couple the degrees of freedom of the gears and integrates the deformations of the teeth. Flexible shafts and the housing are modeled by finite elements and bearings can be introduced as additional stiffness to couple shafts and the housing. To reduce the computational cost, models based on substructuring emerge. Thouviot *et al.* [128] propose a condensed description using CMS (Component Mode Synthesis) for gear pair coupled with an analytical contact. So, the problem can be divided into two main parts. The first one deals with the deformation of the flexible meshing gears. Then, the author treats the contact analytically to avoid to consider all the nodes in the tooth flank

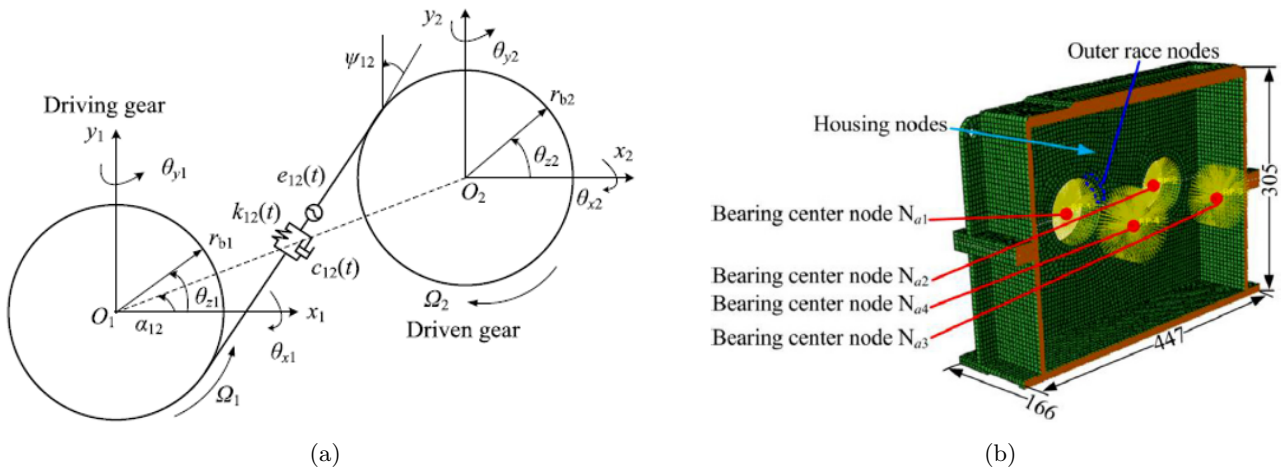


Figure II.11: Example from [38] of lumped parameter description (a) and FE representation of the housing (b).

as master nodes. Thus, one master node by teeth is considered at base radius position but the contact force is acting on the tooth flank. So, an equivalent contact force is transmitted at the master node.

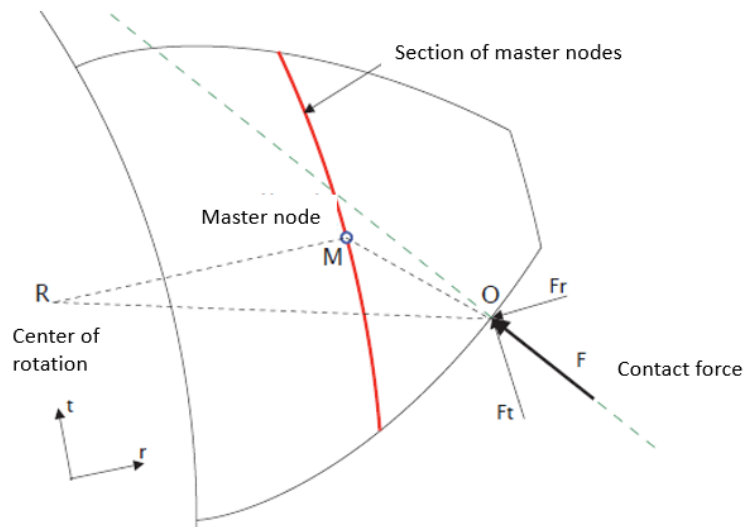


Figure II.12: Schematic representation of transmitted contact force [128]

Other authors use multibody models with model order reduction. For instance, Virlez *et al.* [138] propose the use of CMS with a multibody description. However, when the mesh of the teeth is fine enough to represent micro-geometric modifications and the stresses under layers, the number of master

nodes on the tooth flank is high. This large number of master node makes the contact resolution time consuming. Blockmans *et al.* [15] use also a multibody representation of the gear pair. To reduce the model, the author propose a novel parametric model order reduction technique. This method can be seen as an extension of the CMS. The reduced basis is a constant set of eigenvectors augmented with a parameter-dependent set of global contact shapes. These global contact shapes represent deformation patterns of the interacting bodies obtained from a series of static contact analyses. The global contact shapes are the parametric part of the reduced basis. Indeed, contact patterns are obtained for successive angle of the rotation of the driving gear. The interpolated contact shape  $\Psi_c(\theta_j^1)$  for a  $\theta_j^1$  angle position of the driving gear is expressed as follows:

$$\Psi_c(\theta_j^1) = (1 - p(\theta_j^1))\Psi_c(\theta_{j-1}^1) + p(\theta_j^1)\Psi_c(\theta_{j+1}^1) \quad (\text{II.8})$$

where  $p(\theta_j^1)$  is a linear parameter depending of the actual position of the driving gear. This proposed

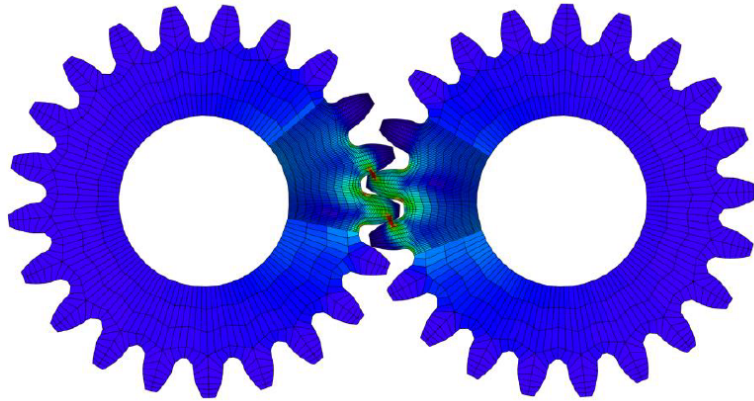


Figure II.13: Static contact equilibrium [15]

reduced basis modify the equation of motion. the parametric aspect of the basis generate additional terms in the equation of motion. This is made the implementation complex. In addition, the sample of global contact shapes has to be large to obtain a relevant interpolation as expressed by the equation II.8. The model proposed by Blockmans *et al.* is the most advanced model in the literature according to my knowledge. To this day, this model has been applied only on gear pair, the inclusion of shafts,

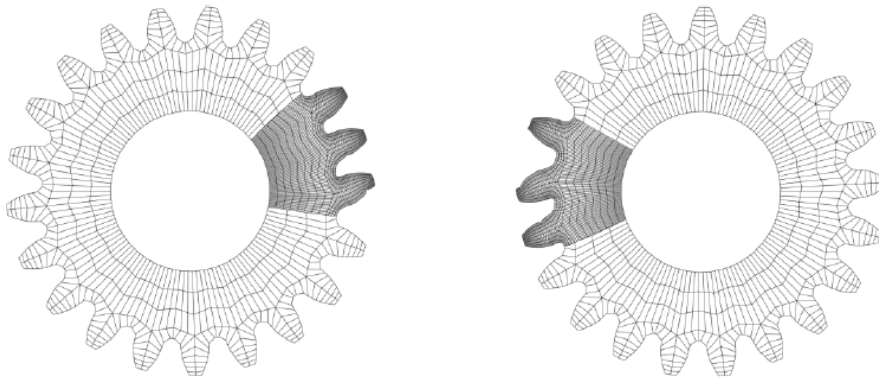
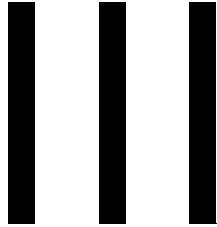


Figure II.14: Example of global contact shapes for the driving gear and the driven gear [15]

bearings and the housing is not yet achieved.

## 4 Conclusion

This chapter aims at introducing the gear dynamical problem. It shows the complexity and the challenge to predict the vibroacoustic behaviour of gears. Indeed, the resulting whining noise (induced by the vibratory state of the housing) is mainly caused by the static transmission error and the mesh stiffness. These internal excitations are periodic at the mesh period and they are impacted by the eccentricity, the micro-geometry defects, the misalignment and the deformation (local and global). Thus, the gear problem is a multi-scale and multi-frequency problem. The dynamic response is rich since the content is dense. Potentially, parametric resonances and instabilities can occur. Finally, we proposed a description of main dynamical models present in the literature.



# Prediction of the quasi-static gear meshing behaviour

---

## Introduction

---

The objective of this chapter is to propose a model that enables the prediction of the whining noise. For this reason, we focus on the characterization of the static transmission error and the mesh stiffness fluctuations. The proposed model must be able to account for the deformation and the micro-geometric defects. For this purpose, a complete modeling of the gear transmission is used and the description of the contact is based on an augmented Lagrangian formulation considering a surface-to-surface contact detection. The proposed methodology is performed through the ANSYS Mechanical ® solver and results are benchmarked against the results obtained from the well-known compliance approach (classical approach).

---

## Contents

---

1	Fundamental equation of motion for contact problems . . . . .	30
1.1	Equation of motion for a continuum contact problem . . . . .	30
1.2	Discretized equation of motion . . . . .	32
2	Existing strategies for the computation of the static transmission error and the mesh stiffness . . . . .	33
2.1	Methods based on the compliance computation . . . . .	33
2.2	In-line computation methods . . . . .	40
3	Proposed methodology: formulation and resolution . . . . .	43
3.1	Contact element definition . . . . .	43
3.2	Frictionless contact formulation . . . . .	45
3.3	Gear simulation with the augmented lagrange formulation . . . . .	48

---

---

4	Practical procedure . . . . .	51
4.1	Tooth generation and profile modifications . . . . .	52
4.2	Mesh convergence . . . . .	53
4.3	Time cost reduction . . . . .	56
4.4	Numerical comparison . . . . .	58
5	Conclusion . . . . .	64

---

## 1 Fundamental equation of motion for contact problems

In this section the theoretical background of the continuum mechanics is presented. The governing equations of flexible multibody dynamics with respect to the contact equations are derived and the Galerkin projection based method is then used to reduce the finite element model.

### 1.1 Equation of motion for a continuum contact problem

Let us consider the evolution over the time interval  $\mathbf{I} = [0, T]$  of the flexible body noted  $\Omega$  with  $T$  the final time of the motion.  $\Omega$  is the collection of bodies. For instance, for two flexible bodies  $\Omega_1$  and  $\Omega_2$ ,  $\Omega = \Omega_1 \cup \Omega_2$ . This flexible body is submitted to a field of volume density of forces  $\mathbf{f}_v$ , a field of surface density of forces  $\mathbf{f}_s$  on  $\Gamma_f$ . We can introduce  $\mathbf{u}$  the displacement field inside  $\Omega$ ,  $\boldsymbol{\sigma}$  the stress tensor,  $\boldsymbol{\varepsilon}$  the strain tensor and  $\mathbf{u}_0$  the imposed displacement field on  $\Gamma_u$ .

$$\left\{ \begin{array}{l} \rho \ddot{\mathbf{u}} = \text{div}(\boldsymbol{\sigma}) + \mathbf{f}_v \text{ on } \Omega \\ \boldsymbol{\sigma}_{ij} = \mathbf{R}_{ijkl} \boldsymbol{\varepsilon}_{kl} \text{ on } \Omega \\ \mathbf{u} = \mathbf{u}_0 \text{ on } \Gamma_d \\ \boldsymbol{\sigma}_{ij} \mathbf{n}_i = \mathbf{f}_s \text{ on } \Gamma_f \end{array} \right. \quad (\text{III.1})$$

$\boldsymbol{\sigma}_{ij}$  and  $\boldsymbol{\varepsilon}_{kl}$  are linked by the Hooke's law which is represented by  $\mathbf{R}_{ijkl}$ . For a given space  $\mathbf{W}$ , we represent the application  $L^2(\mathbf{I}, \mathbf{W})$  as:

$$L^2(\mathbf{I}, \mathbf{W}) = \left\{ \begin{array}{l} w : \mathbf{I} \rightarrow \mathbf{W} \\ \int_{\mathbf{I}} \|w\|_{\mathbf{W}}^2 dt < +\infty \end{array} \right.$$

and  $\|\cdot\|_{\mathbf{W}}$  a norm on  $\mathbf{W}$ . Then, we consider the Sobolev space  $\mathbf{H}^1(\Omega)$ :

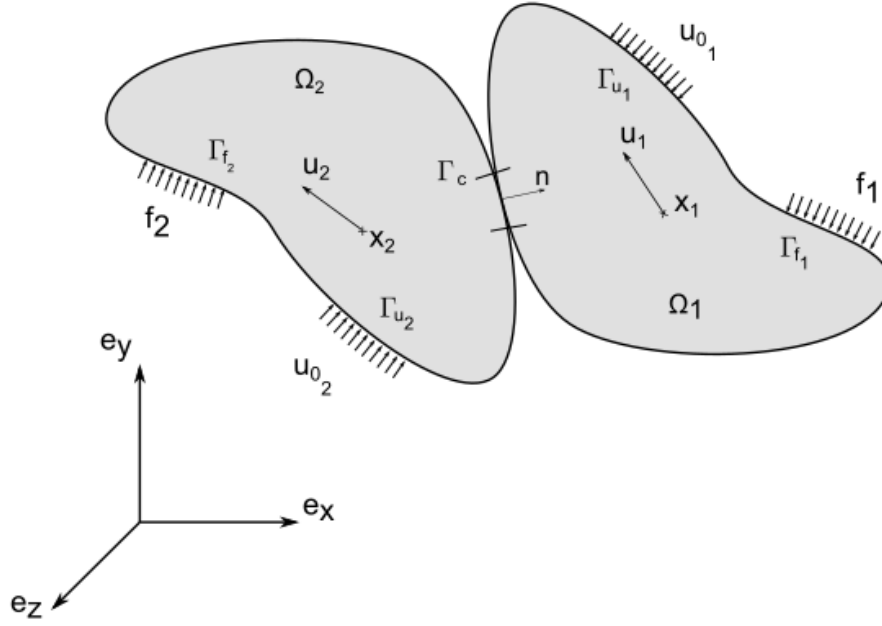


Figure III.1: Schematic representation of bodies in contact submitted to forces and boundary conditions

$$\mathbf{H}^1(\Omega) = \left\{ w \in L^2(\Omega), \delta w \in L^2(\Omega) \right\}$$

We introduce  $\mathbf{W}_0$  such as:

$$\mathbf{W}_0 = \left\{ w \in \mathbf{H}^1(\Omega), w = 0 \text{ on } \Gamma_d \right\} \quad (\text{III.2})$$

Solving the (III.1) is equivalent to solving the following weak primal formulation:

$$\begin{cases} \text{Find } \mathbf{u} \in \mathbf{W}_0 \\ \forall \mathbf{w}^* \in \mathbf{W}_0, a(\mathbf{u}, \mathbf{w}^*) = l(\mathbf{w}^*) \end{cases}$$

with  $\mathbf{w}^*$  the virtual displacement and where the virtual works of the internal and external forces are:

$$\forall (\mathbf{u}, \mathbf{w}^*) \in \mathbf{W}_0 \times \mathbf{W}_0, a(\mathbf{u}, \mathbf{w}^*) = \int_{\Omega} \boldsymbol{\sigma}(\mathbf{u}) : \boldsymbol{\varepsilon}(\mathbf{w}^*) d\Omega \quad (\text{III.3})$$

$$\forall \mathbf{u} \in \mathbf{W}_0, l(\mathbf{w}^*) = \int_{\Gamma_u} \boldsymbol{\sigma}(\mathbf{u}) \mathbf{n} u_0 d\Gamma_u + \int_{\Omega} \mathbf{f}_v \mathbf{w}^* d\Omega + \int_{\Gamma_f} \mathbf{f}_s \mathbf{w}^* d\Gamma_f + \int_{\Gamma_c} \mathbf{F}_n \mathbf{d}^* d\Gamma_c \quad (\text{III.4})$$

where  $\mathbf{F}_n$  stands for the contact forces and  $\mathbf{d}^*$  represents the virtual distance between the potential bodies in contact. The strain tensor  $\boldsymbol{\varepsilon}$  is also linked to the displacement field by:

$$\boldsymbol{\varepsilon}(\mathbf{u}) = \frac{1}{2}(\nabla\mathbf{u} + (\nabla\mathbf{u})^T + (\nabla\mathbf{u}) \cdot (\nabla\mathbf{u})^T) \quad (\text{III.5})$$

This quadratic equation enables the inclusion of large deformation bodies. For our gear problem, the deformation are small compared to the size of the gear body. So in practice, the quadratic term  $(\nabla\mathbf{u}) \cdot (\nabla\mathbf{u})^T$  can be omitted. It appears that the problem can be divided into two main parts: the first deals with the deformation of the flexible bodies 1 and 2 corresponding to the meshing gears. The second deals with the contact between the bodies. The main objective is to determine the forces generated by the contact on the gear teeth while considering the flexibility of bodies.

## 1.2 Discretized equation of motion

The continuum forms of the weak primal formulation have just been defined. However, in the approach developed hereafter, an approximation of the displacement field is needed. The most popular method is the finite element method and this is what we used in this manuscript. This discretized method consists in decomposing the displacement field into a product of functions of space and time:

$$\mathbf{u}(\xi, t) \approx \mathbf{N}(\xi)\mathbf{x}(t) \quad (\text{III.6})$$

$\mathbf{N}(\xi)$  represents the finite element shape functions and  $\mathbf{x}$  contains the generalised displacement of each degree-of-freedom. In practice,  $\mathbf{x}$  is associated to the nodes of the mesh. Thus, the discretized equation of motion reads:

$$\mathbf{M}\ddot{\mathbf{x}} + \mathbf{C}\dot{\mathbf{x}} + \mathbf{K}\mathbf{x} + \mathbf{F}_{nl}(\mathbf{x}) = \mathbf{F}_{ext} \quad (\text{III.7})$$

$\mathbf{M}$ ,  $\mathbf{K}$  and  $\mathbf{C}$  are respectively the mass, damping and stiffness matrices.  $\mathbf{F}_{ext}$  is the vector of external forcing and  $\mathbf{F}_{nl}$  is the nonlinearity vector representing the contact between bodies. The general form

of the discretized equation of motion are used in the section 3 to derived the proposed methodology but first the existing strategies for the computation of the static transmission error and the mesh stiffness are presented. This review of the main strategies used in the literature enables to find out the benefit of method proposed in the section 3.

## 2 Existing strategies for the computation of the static transmission error and the mesh stiffness

In the last decades, a large variety of strategies have been proposed in the literature to compute the static transmission error and the mesh stiffness. This section provide a description of the main existing strategies used for the computation of the static transmission error and the mesh stiffness.

For the computation of the static transmission error and the mesh stiffness, methods can be classified as methods based on the computation of the compliance of the gear (teeth and gear body) beforehand and methods that computes at the same time the compliance and the instantaneous contact conditions (in-line methods). Methods based on the computation of the compliance of the gear differ by the compliance is computed. For instance, it can be analytically, semi-analytic, by finite element ...

### 2.1 Methods based on the compliance computation

In this section, the main methods in the literature for the computation of the compliance beforehand are presented.

*Methods based on mesh stiffness expression:* Welbourn [142] provides a constant indicative value of the mesh stiffness for spur gears made of steel equal to  $14 \cdot 10^9 \text{N/m}$ . Umezawa [132] firstly introduced a formula to describe the mesh stiffness fluctuation of helical gears considering a rotational vibration system. The definition is based on the theoretical deflection on the line of action of the

loaded teeth. The resulting mesh stiffness is a combination of exponential functions. Cai and Hayashi [19] in 1994 propose a mesh stiffness analytical expression for the linear approximated equation of vibration of a pair of spur gear. The formula takes into account the effects of the static load, the time varying stiffness and the profile modification. The expression is given by:

$$k_m(\theta_1) = \frac{\bar{k}}{0.85\epsilon} \left( \frac{-1.8}{(\epsilon\theta_z)^2} \theta_1^2 + \frac{1.8}{\epsilon\theta_z} \theta_1 + 0.55 \right) \quad (\text{III.8})$$

where  $\bar{k}$  is the mean value of mesh stiffness,  $\theta_z$  is the angular mesh period and  $\epsilon$  is the contact ratio. Later, Cai [17] introduced a modified mesh stiffness function to support helical gears and results are in good agreement with those predicted using the theoretical calculation of Umezawa. More recently, Mark *et al.* [97] developed formulations to take into account the tooth elastic deformation including the mesh stiffness contribution. The geometric deviations of the working surfaces from the perfect involute tooth profile was also added.

**Method based on Castigliano principle:** in [30, 31, 29, 118, 149, 152], the transmission error and the mesh stiffness fluctuations are obtained with the Castigliano principle. The tooth is modelled as a non-uniform cantilever beam for describing bending, shear and axial deformation. The tooth is described in Fig. III.2.

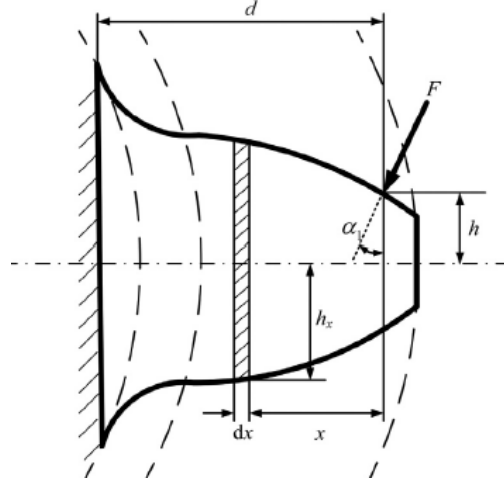


Figure III.2: Non-uniform cantilever beam model of the tooth [30]

The bending, shear and axial compressive stiffness in the same direction under the load  $F$  are  $k_b$ ,  $k_s$  and  $k_a$ , respectively. These quantities can be expressed as follows:

$$\frac{1}{k_b} = \int_0^d \frac{3(x \cos(\alpha_1) - h \sin(\alpha_1))^2}{2E h_x^3 b} dx \quad (\text{III.9})$$

$$\frac{1}{k_s} = \int_0^d \frac{1.2 \cos^2(\alpha_1)}{2G h_x b} dx \quad (\text{III.10})$$

$$\frac{1}{k_a} = \int_0^d \frac{\sin^2(\alpha_1)}{2E h_x b} dx \quad (\text{III.11})$$

with  $E$ ,  $G$  the Young modulus and shear modulus.  $b$  represents the tooth face width. The hertzian-like deformation is accounted for by introducing the hertzian contact stiffness  $k_h$  as:

$$\frac{1}{k_h} = \frac{4(1 - \nu^2)}{\pi E b} \quad (\text{III.12})$$

with  $\nu$  the Poisson ratio. Beneath the tooth, the gear body deformation modifies the gear tooth stiffness. Some authors studied the influence of an elastic gear body on the tooth flexibility and the STE fluctuation. Weber and Banascheck [141] proposed a model to estimate the gear body-induced tooth deflection. The tooth is assumed to be rigid and the wheel body is modeled as an elastic half plane. Sainsot [116] extended the previous model by developing a semi-analytical formula for which

the elastic half plane is replaced by a solid disk. The gear body induced tooth bending displacement is given by:

$$\frac{1}{k_f} = \frac{\cos^2(\alpha_1)}{bE} \left[ L^* \left( \frac{u}{S} \right)^2 + M^* \frac{u}{S} + P^* \left( 1 + Q^* \tan^2(\alpha_1) \right) \right] \quad (\text{III.13})$$

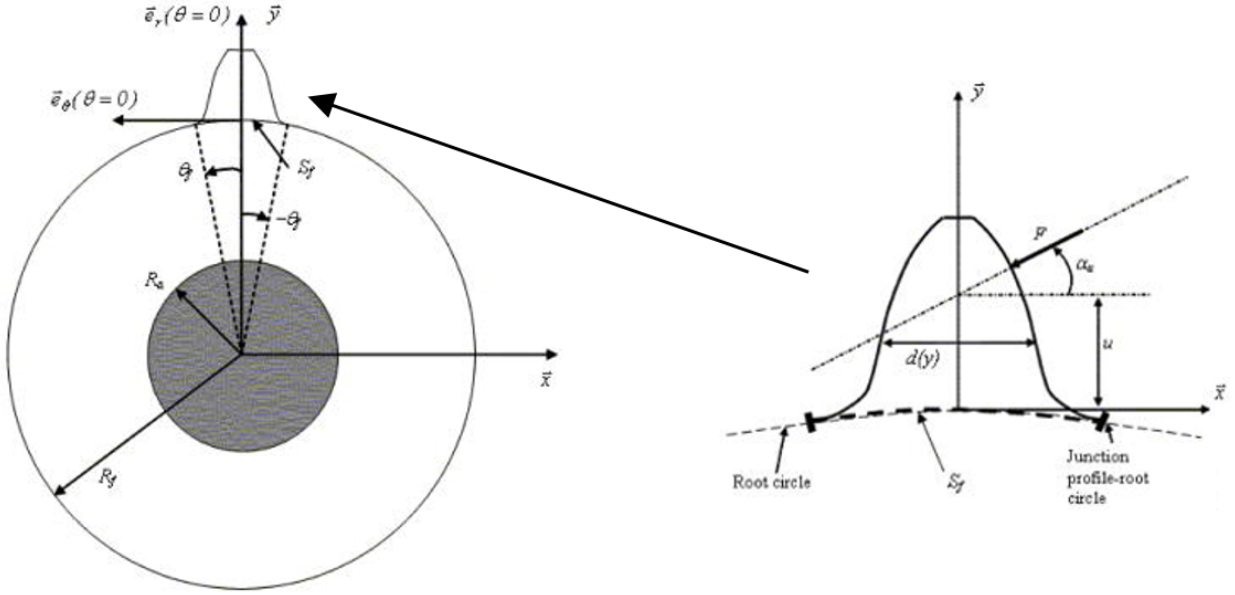


Figure III.3: Gear body induced tooth deformation as [116]

$L^*$ ,  $M^*$ ,  $P^*$  and  $Q^*$  are polynomial functions depending on  $\theta_f$  and the length ratio  $R_f/R_a$ . Their polynomial coefficients are identified using values proposed by Sainsot *et al.* in [116]. The deformation of the adjacent teeth is not taking into account with the work of Sainsot *et al.* Some improvement have been made by Xie *et al.* to add the adjacent loaded teeth [150]. The equivalent mesh stiffness  $k_m$  is finally obtained:

$$\frac{1}{k_m} = \frac{1}{k_{b1}} + \frac{1}{k_{s1}} + \frac{1}{k_{a1}} + \frac{1}{k_{f1}} + \frac{1}{k_{b2}} + \frac{1}{k_{s2}} + \frac{1}{k_{a2}} + \frac{1}{k_{f2}} + \frac{1}{k_h} \quad (\text{III.14})$$

where the subscript 1 and 2 state for the input and output gear, respectively. A summary of the computation process is described in Fig. III.4. The use of analytical expressions is an efficient way to quickly predict optimized tooth deviations for reducing transmission error fluctuations. However

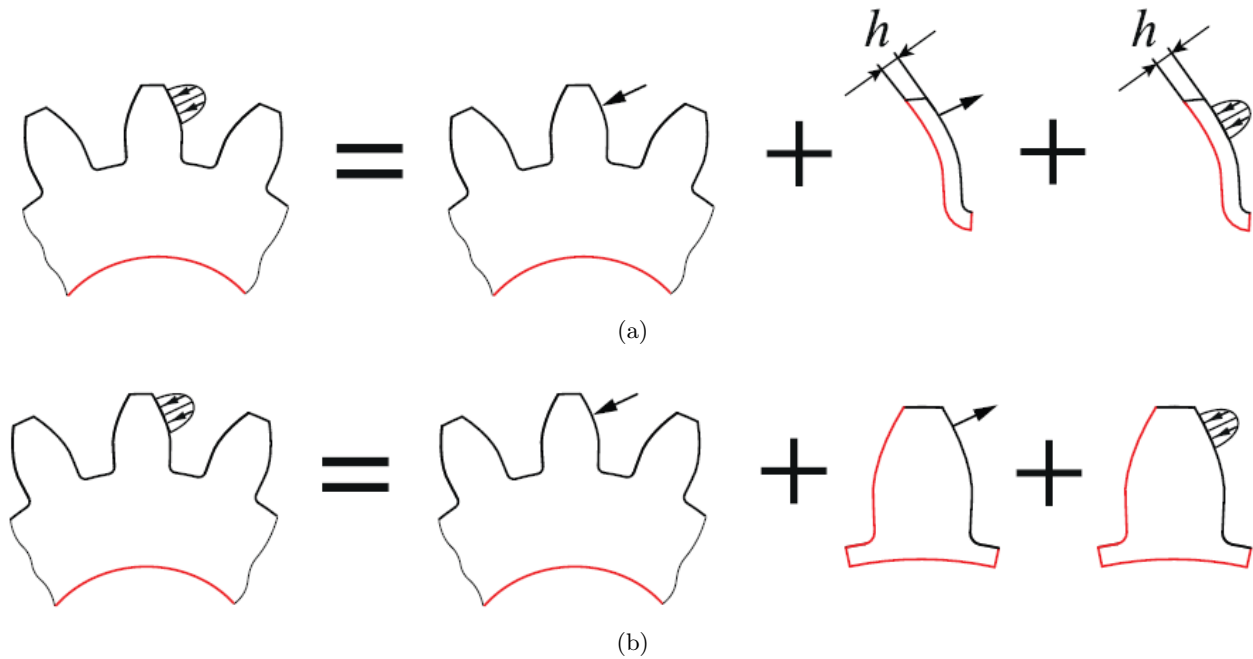


Figure III.4: Fixed surfaces (—) proposed by (a) Vedmar *et al.* [133] and (b) Chang *et al.* [28]

the flexibility of the main components of a gearbox are not considered. Indeed, most of the time, the flexibility of shafts, bearings and the housing are not taken into account. Additionally, analytical expressions have been developed for spur and helical gears with restrictive assumptions, for instance: helical gear with narrow faced width and there is no expression to analyze more complex geometric gears like spiral bevel gears. The limited assumptions leads thus to an overestimation of the transmission error and the mesh stiffness.

**Methods off-line of the finite element analysis:** in the compliance method [21, 67, 102, 127], the contact problem is solved off-line of the finite element analysis including the gear transmission. The contact lines are assumed to be located in the theoretical action plane and the gear static equilibrium is then modelled by separating the gear compliance and the local contact equations along the contact lines [156, 7, 18, 112]. Thus, the gear tooth compliance is preliminary computed by a finite element analysis or by some alternative analytical tooth bending models using for example Ritz-Galerkin interpolation

[42]. Generally, the nonlinear hertzian-like deformation is independently introduced either with an exact or approximate formulation. Furthermore, the potential contact lines located on the theoretical action plane are discretized in small segments where constant punctual forces are applied. Considering the driving angle  $\theta_1$ , a symmetric semi-positive compliance matrix  $\mathbf{H}(\theta_1)$  is introduced for representing the relation between force and displacement at each discretized segment. An initial gap vector, here referred to as  $\mathbf{e}(\theta_1)$ , describing the initial distance between the teeth on each segment is introduced in order to take into account the tooth flank modifications and manufacturing errors. The misalignment between shafts and the deviation between teeth, induced by the global deformation of the entire transmission, are introduced at this stage. As the static transmission error, noted  $\delta(\theta_1)$ , fluctuates with the driving angle  $\theta_1$  for a given transmitted normal load  $F$ , input data (matrix  $\mathbf{H}(\theta_1)$ , vector  $\mathbf{e}(\theta_1)$ ) are iterated for successive position  $\theta_1$ , most of the time along a meshing period, involving a kinematic analysis of the meshing process. For each position  $\theta_1$ , the matrix equation representing the mesh contact conditions can be formulated as the following problem:

$$\begin{cases} \mathbf{H}(\theta_1) \cdot \mathbf{p}(\theta_1) = \delta(\theta_1) \cdot \mathbf{1} - \mathbf{e}(\theta_1) \\ \mathbf{1}^T \cdot \mathbf{p}(\theta_1) = F \end{cases} \quad (\text{III.15})$$

under the following constraints:

$$\begin{cases} -\sum_j H_j(\theta_1) p_j(\theta_1) + \delta(\theta_1) \geq e_j(\theta_1) \\ p_j \geq 0 \end{cases} \quad (\text{III.16})$$

In this equation under constraints, the unity column vector  $\mathbf{1}$  has all its components equal to 1, the column vector  $\mathbf{p}$  is the unknown distributed load to be solved and the scalar function  $\delta(\theta_1)$  represents the unknown STE, also to be solved. Different algorithms can be used to obtain the solution ( $\mathbf{p}(\theta_1)$ , and  $\delta(\theta_1)$ ), the most popular one is based on a modified simplex method [34]. The mesh stiffness is computed by a numerical derivation of the transmitted load  $F$  relative to the STE. This method requires an analysis to obtain the global displacement field including the local singularity induced by the applied punctual load. Then, a partial model of the tooth is used to quantify and remove this

singularity. These compliance methods are similar to the approach used in the software LDP [67] and it is well adapted for cylindrical gears with parallel shafts but are more complex to implement in the case of other geometries as, for example, spiral bevel gears. Some variants were investigated by other authors depending on the boundary conditions considered during the compliance computation as shown in Fig. III.4.

***Sliced tooth method:*** The teeth are divided into multiple slices along its width. Each slice is considered as rigid, and therefore a lumped parameter model is used to describe the tooth. The contact occurs on the theoretical contact lines and the flexibility of the gear teeth is described through several independent stiffness elements distributed along the line of action. Most of the time, each slice are considered independent to their nearby slice. However, an additional stiffness can be employed between each slice to couple the different slices. An hybrid modular model was proposed by Guilbert *et al.* [55, 53, 54] where the sliced tooth method is combined with a condensed substructure of the gear body. More precisely a component mode synthesis considering free interface modes was retained. The one dimensional model associated to the sliced tooth method is then linked to the condensed element using a mortar based contact as depicted in Fig. III.5.

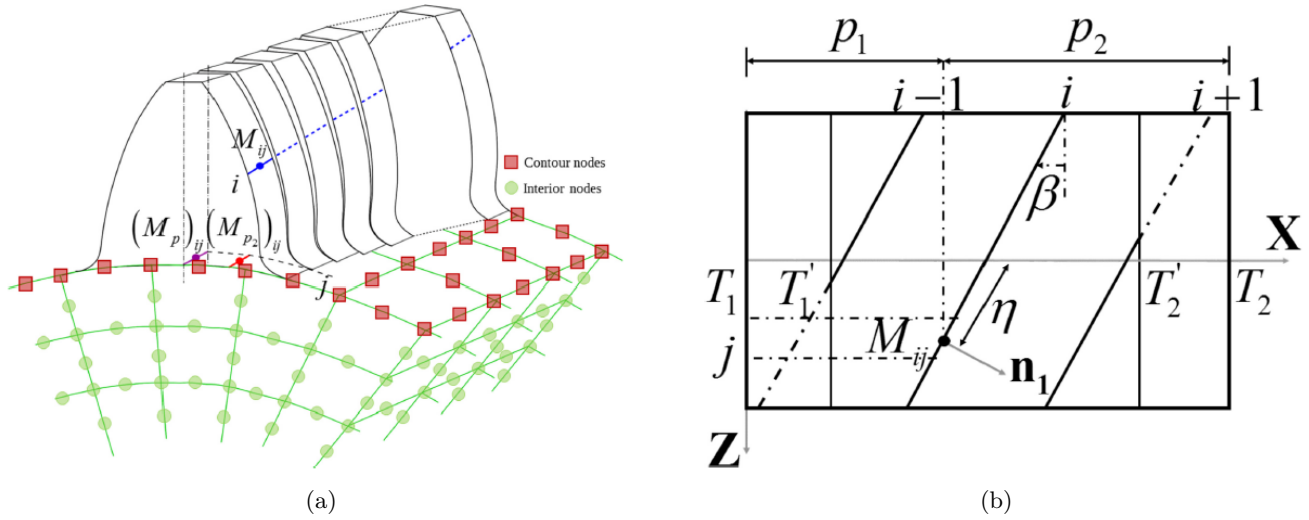


Figure III.5: (a) Sliced tooth and condensed substructure connection and (b) the associated discretized plane of action [54]

The hybrid FE-analytical approaches presented here are the most popular in the literature due to their usage convenience. They provide better results than analytical expressions. The contact occurs on the theoretical contact lines for the compliance method and the sliced tooth method. These approaches are well suited for spur and helical gears with parallel shafts but much more complex to implement when dealing with off-line contact or spiral bevel gears for which theoretical contact lines are difficult to determine a priori. Additionally, the surface integral approach does not consider micro-geometry modifications and the compliance and sliced tooth method treat the micro-geometry as a gap function. This has no influence on the global gear flexibility but it changes the contact characteristics.

## 2.2 In-line computation methods

In this section, methods that compute directly the gear compliance and the instantaneous contact conditions are presented.

**Surface integral method:** Vijayakar [135] combined FE and surface integral methods for solving the analytical contact and the FE solution at surfaces. The finite element model predicts the deformation

far away from the contact area but in the contact zone a surface integral form of Boussinesq solution is used to estimate the relative displacement of body points. Then, a "matching interface" is employed to combine the finite element solution and the surface integral solution. The displacement field is then estimated by the following least square problem:

$$\min_{q \in \Gamma} \int_{\Gamma} [u(r_{ij}, r) - (u^{si}(r_{ij}, r) - u^{si}(r_{ij}, q) + u^{fe}(r_{ij}, q))]^2 \quad (\text{III.17})$$

where  $u(r_{ij}, r)$  is the displacement of a field point  $r$  due to a load in  $r_{ij}$ ,  $q$  is a location within the body. The *si* and *fe* superscripts state respectively for the surface integral solution and the finite element solution. Although the approach requires a less detailed FE model compared with fully FE-based contact simulations, the procedure of matching the Boussinesq solution and FE solutions is computationally demanding. Additionally, the approach introduced by Vijayakar predicts the size of the contact area assuming an elliptic area as claimed by Hertz theory and this is usually not the case due to the variation of the curvatures at the contact surfaces

**Fully FE-based methods:** The use of fully FE-based models provide a better accuracy but the computational time increase. Some authors considered a FE-based contact for describing the transmission error and the mesh stiffness. Arafa et al. [9] investigated the computation of single tooth mesh compliance using a FE method without considering the adjacent teeth. Cooley *et al.* [35] used a finite element model of a spur gear as shown in Fig. III.6 to determine the mesh stiffness based on a series of nonlinear static simulations performed over a mesh period. Similarly, Korta *et al.* [86] proposed a refined model introducing tip relief modification for optimizing the tooth geometry.

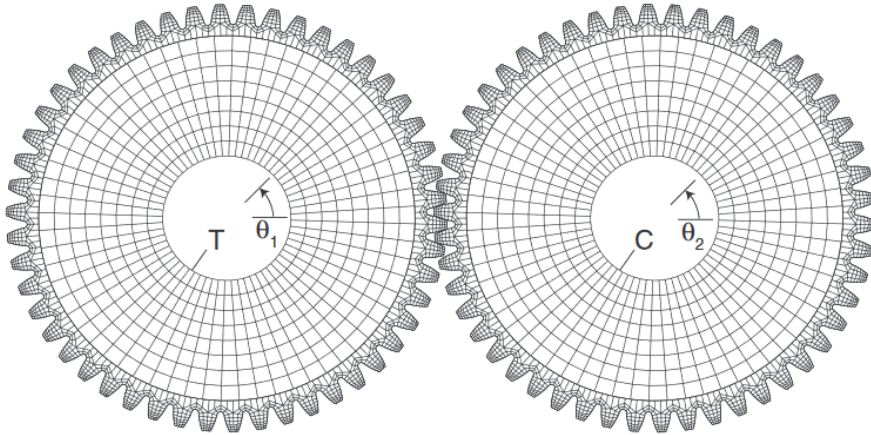


Figure III.6: FE model of the spur gear used in [35]

The existing fully FE-based models for describing the static transmission error and mesh stiffness rely on a series of nonlinear (contact) static analyses where the gear pair is manually positioned for each angular step. Therefore, the global deformation of other gear components (for instance: flexible shafts) generated by the motion of the operating gears is not properly taken into account. The methods used have been established exclusively on a gear pair without micro-geometric modifications. Additionally, the mesh in the contact area is not refined enough to retrieve the normal contact characteristic claimed by Hertz's theory.

In the next part of this chapter, we are looking for a general solution (much more general than all of the above mentioned solutions). We propose thus a methodology based on a fully FE-based method to compute the static transmission error and the mesh stiffness. The methodology is described in detailed (FE models used and algorithms). The objective of the next section is to evaluate the feasibility of a fully FE-method. For this purpose, validations are performed for different loading conditions, for different micro-geometry modifications and considering the time cost. Normal contact characteristics are also assessed with respect to Hertz's theory.

### 3 Proposed methodology: formulation and resolution

Solving non-linear problems by finite element analysis remains a challenge due to the contact and the nonsmooth mechanics induced by possible contact losses [148, 146, 147, 145]. The contact formulation needs an accurate contact detection algorithm and an appropriate time integration scheme to deal with large stiffness variations during the contact treatment. Thus, two particular conflicts have to be addressed for describing properly a FE-based contact. It corresponds to the increased difficulty in the implementation compared with a classical FE analysis. Then it's the large number of degrees of freedom involved induced by the refinement of the contact zone.

The proposed methodology relies on a flexible finite element (FE) contact analysis considering the quasi static behaviour of the gear transmission. The flexibility of the gear body, shafts, bearings and the housing can be taken into account during the contact treatment. The numerical methods used for the gear contact finite element analysis are presented hereafter.

#### 3.1 Contact element definition

In a general contact analysis, the size and shape of the contact area is not known in advance and detecting accurately bodies' interaction is essential for an efficient contact analysis. In the case of gears, tooth profile deviations and hertzian-like deformations are of the order of a few micrometers which requires a very fine mesh element size of the tooth surface. A coarse mesh can support small deformations, but cannot represent tooth profile deviations properly. Thus, the contact detection has to be extremely precise. As shown in Fig. III.7, a 8-noded quadrilateral linear contact element intended for 3D geometries and flexible-flexible contact analysis is used. This contact element is retained to speed up the contact treatment compared with quadratic element for which quadratic shape functions are assessed during the contact. Usually, quadrilateral linear element are well suited

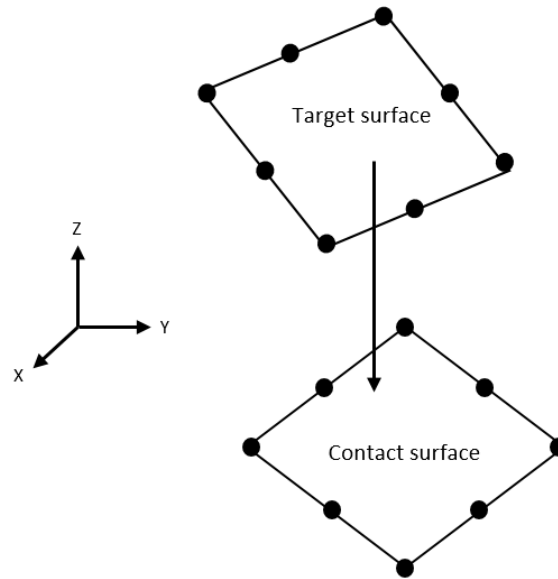


Figure III.7: 8 nodes surface-to-surface contact element.

to represent displacement fields but stresses evolve with an order lower than the element order. So, hexa linear elements lead to constant stresses per element. We need thus to model the gear teeth with a mesh sufficiently fine to obtain smooth stresses from one element to another.

Most of the time when dealing with contact analysis the surface of one body is conventionally taken as a contact surface and the other one as a target surface considering that both surfaces are associated with flexible bodies. There are several approaches to model the contact detection, namely: node-to-node, node-to-segment, segment-to-segment, node-to-surface and surface-to-surface approaches. In this proposed methodology, a surface-to-surface contact element is privileged in order to take account of the tooth micro-geometry as opposed to the other contact elements for which only target nodes are constrained to prevent penetration into the contact surface. Indeed, for the other contact element formulation, the contact conditions are introduced so that each target node interacts with a projected point on the contact surface. Consequently, contact conditions involve a single node and

it concentrates the force at this node. So, node-to-surface, node-to-segment and segment-to-segment facilitate penetration during the contact detection and it leads to less precise stress and pressure. In contrast, the target surface can penetrate into the contact surface for the surface-to-surface element and this interpenetration tolerance has to be adjusted in regards to the tooth profile modifications. This surface is projected on the contact surface and the contact detection points are the integration points which are either nodal points or gauss points [27]. Contact inequalities are expressed at integration points and gauss points represent sampled discrete points on the surface element. 4 gauss points on the surface contact element are considered. Gauss points are integrated on the surface using corresponding weight factors. The node values are then obtained with shape functions using the value of the nearest corresponding gauss points. The interpenetration is handled on the target surface and its integration points along the normal direction [26]. The surface-to-surface element involves more nodes during the contact treatment which has a smooth effect on the stress and the pressure. Indeed, contact forces do not jump when a contact node slide off the edge of a target surface because contact forces are computed even when it is only partially in contact. The surface-to-surface element provides thus a more accurate computation of contact stresses for the contacting elements considered.

### 3.2 Frictionless contact formulation

In this thesis, we focus on frictionless contact because vibroacoustic phenomena in gear transmission are mainly caused by the fluctuation of the normal contact force at the gear pair [22, 116]. If one is interested in power losses, friction and therefore tangential contact forces, should be considered [84, 134].

Considering a flexible gear pair discretized by FE method, to every contact node or gauss point  $i$  associated to mesh elements corresponds a gap function  $d_i$  measuring the signed distance between the

contact and the target surfaces along the normal direction.  $F_i$  is the contact force acting on the target surface. The unilateral constraints used to represent the nonsmooth mechanics of the contact between the gear teeth are modeled with the Signorini conditions [145, 146, 147]:

$$\begin{cases} d_i \geq 0 \\ F_i \geq 0 \\ d_i F_i = 0 \end{cases} \quad \forall i, \quad (\text{III.18})$$

The constraints  $d_i \geq 0$  and  $d_i F_i = 0$  represent the impenetrability and complementarity conditions. The contact forces  $F_i \geq 0$  are generated only when the gear tooth contact occurs ( $d_i = 0$ ), while the contact forces are zero ( $F_i = 0$ ) when the gear tooth contact is lost ( $d_i > 0$ ).

Several contact algorithms are associated with the contact element depicted in Fig. III.7. These contact algorithms are based on different strategies to model and evaluate the contact force  $F_i$ . Since the surface-to-surface contact element enables the detection of the possible contact locations thanks to the evaluation of the gap function  $d_i$ , the enforcement of the contact conditions into the equation of motion has to be performed. To this end, the pure penalty method, augmented lagrangian method and pure lagrange multiplier method are commonly used in FE softwares and particularly in the ANSYS Mechanical® solver. The different formulations can be classified into two categories corresponding to penalty methods and lagrangian methods. A brief description of the different formulations is presented below:

**Pure penalty method:** the pure penalty method consists in adding a penalty term represented by a nonphysical (or mathematical) contact stiffness called the penalty stiffness as shown in Fig. III.8.

The contact force  $F_i$  acting on the target surface is thus defined by:

$$F_i = \kappa d_i \quad (\text{III.19})$$

where  $\kappa$  is the penalty stiffness coefficient. A finite amount of penetration is required to reach the equilibrium. The penalty stiffness drives the contact, a small value correspond to soft contact and a large value is associated to stiff contact. The pure penalty method does not overconstrains the problem since no additional DOF are added. However, the global stiffness matrix of the system depends on the penalty stiffness coefficient retained.

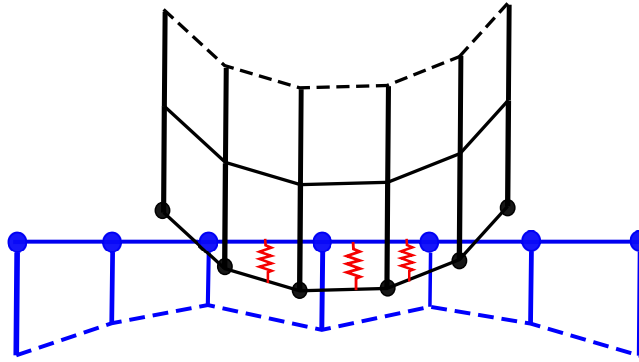


Figure III.8: Description of the pure penalty method.

**Pure lagrangian method:** the pure lagrangian method uses a Lagrange multiplier as an added degree of freedom. The FE model becomes larger and the contact force  $F_i$  acting on the target surface is thus defined by:

$$F_i = \lambda_i \quad (\text{III.20})$$

where  $\lambda_i$  is the Lagrange multiplier associated to the contact node  $i$ .

The pure penalty method received a larger approval in the literature due to its implementation convenience. The main drawback is that the amount of penetration between the two surfaces depends on this stiffness [45, 126, 117]. For this reason, the penalty formulation can lead to ill-conditioned problems and inaccurate solutions.

The pure lagrangian method enforces zero penetration. It does not require additional stiffness but

it needs more iterations to reach contact conditions convergence and therefore it is computationally demanding [109]. Also this method is not working well with iterative solvers and some direct solvers due to the zero diagonal block that it generates. This method can also lead to inaccurate solutions because the method overconstrains the model. Another method named the *Augmented lagrange multiplier method* [124, 91] has been developed to keep the advantages of the two previous contact formulations. The approach is an iterative combination of the penalty method and lagrange multiplier formulation. Compared to the penalty method, the augmented lagrangian method usually leads to better conditioning and is less sensitive to the magnitude of the contact stiffness coefficient. The impenetrability is thus achieved while improving the convergence. The contact force  $F_i$  acting on the target surface is defined by:

$$F_i^j = \kappa d_i^j + \lambda_i^j \quad (\text{III.21})$$

$\kappa$  is the penalty stiffness coefficient,  $\lambda_i^j$  is the iterative lagrange multiplier associated to the contact node  $i$  at the iteration  $j$  which is updated until  $d_i^j$  is sufficiently small (i.e  $d_i^j \leq \epsilon$ , typically  $\epsilon = 10^{-2}$ ) [91, 124]. The augmented lagrangian formulation is thus retained for the proposed methodology to solve the gear contact problem using a 8 noded quadrilateral linear surface-to-surface contact element.

### 3.3 Gear simulation with the augmented lagrange formulation

The Signorini conditions must have been included in the discretized equation of motion representing the gear system. The problem to solve the gear dynamics is expressed as follow:

$$\begin{cases} \text{III.18} + \text{III.21} \\ \mathbf{M}\ddot{\mathbf{x}} + \mathbf{C}\dot{\mathbf{x}} + \mathbf{K}\mathbf{x} + \mathbf{F}_{nl}(\mathbf{x}) = \mathbf{F}_{ext} \end{cases} \quad (\text{III.22})$$

where  $\mathbf{x}$  contains the generalised degree-of-freedom and  $\mathbf{M}$ ,  $\mathbf{C}$ ,  $\mathbf{K}$  are respectively the mass, damping and stiffness matrix.  $\mathbf{F}_{nl}$  is the contact force obtained by applying the Signorini conditions and solving the augmented lagrangian formalism iteratively.  $\mathbf{F}_{ext}$  is the vector of external forces which correspond to the output torque applied to the driven wheel. The approach presented here focuses on the quasi-

static behaviour of the gear pair. Indeed, the dynamic equation (III.22) is solved for a slow rotation of the driving gear (1 rpm) and the dynamical effects are needed only to make the matrix definite positive. It improves the convergence during the gap covering phase.

We deal directly with flexible multibody analysis in quasi-static operating conditions for evaluating the transmission error, especially to show complex effects of the gear mesh process. Indeed, the contact treatment phase (contact detection and contact force computation) is solved in real operating conditions. So, specific gear mesh behaviour is brought to light compared to hybrid FE-analytical methods. The multibody modelling approach aims at providing a generic model that can be used as a reference for meshing settings, contact settings and loading conditions. The proposed methodology intends to accurately identify the gear internal excitation. For this purpose, the procedure, the implementation and the results precision are evaluated. As mentioned in the previous section, a fine mesh is of paramount importance to highlight the influence of the load level but also to take into account the hertzian-like deformation and the micro-geometry. Knowing that the tooth deformation takes account of tooth deflection (potentially gear body, shafts ...) and local hertzian-like deformation induced by the contact, the mesh has to be refined accordingly in the contact area. Moreover, a nonlinear analysis must be carried out for various levels of output torque to show the effect of load on the tooth deformation. To achieve the simulation, three steps have to be set up:

- firstly, the gear backlash is covered by a rotation of the driving wheel in order to establish the contact at an initial state as shown in Fig III.9. This step enables therefore the detection of the initial contact locations induced by possible mountings errors, shafts misalignment and global deformation of the whole gear transmission.
- Then, while the rotation of the driving wheel is fixed, the output torque is applied on the driven

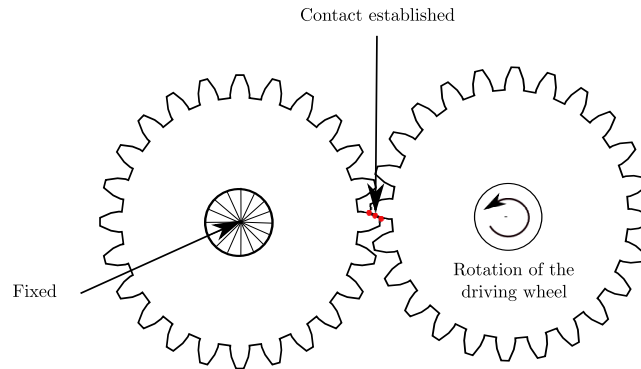


Figure III.9: Description of the first step.

wheel as shown in Fig III.10. The requested output torque is thus reached for a quasi-static equilibrium of the gear pair.

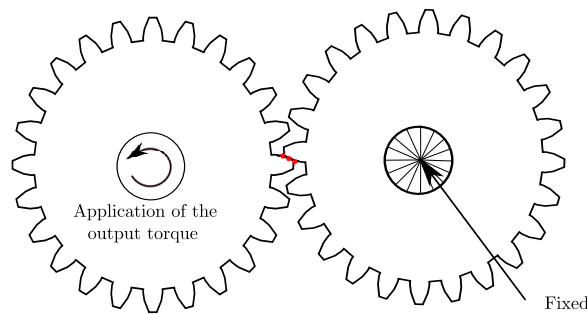


Figure III.10: Description of the second step.

- Finally, a rotation of the driving wheel is performed over a period corresponding to the fundamental period of the static transmission error (at least one mesh period). This allows for an effective computation of the static transmission error while recovering the root stress, the shear stress and the contact characteristics. The third step is described in Fig III.11.

A control node is defined at each gear centre to apply boundary conditions and to measure the time varying input and output gear angles. There is a spider-web type of mesh to connect this control node with the web. Constraint relations are used between them. The static transmission error  $\delta(\theta_1)$  is then computed along the line of action and the mesh stiffness  $k(\theta_1)$  is approximated by a numerical differentiation of the transmitted load  $F$  versus  $\delta(\theta_1)$ . The discretization of the angular position of

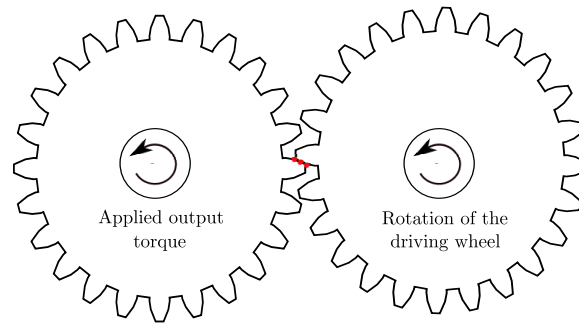


Figure III.11: Description of the third step.

the driving wheel has to be finely defined for describing properly the sudden variation of the STE. At least 40 points over one mesh period are considered in the proposed methodology. In addition, to avoid numerical errors, the differentiation of the mesh stiffness is achieved by taking a centred differentiation step equal to 15% of the load and the STE. The contact procedure used in the flexible multibody approach is summarized in Fig. III.12.

The proposed methodology can be applied to any types of gears, even for spiral bevel gears for which theoretical contact lines are geometrically complex to determined. The flexibility of the whole components of a gear transmission (shafts, bearings and housing) can also be included during the application of the procedure.

## 4 Pratical procedure

This section describes how to apply efficiently the proposed methodology using the ANSYS Mechanical ® solver. Elements of validations are presented in terms of static transmission error, mesh stiffness and hertzian shear stresses. Additionally, the proposed methodology is assessed with respect to its time cost-effectiveness.

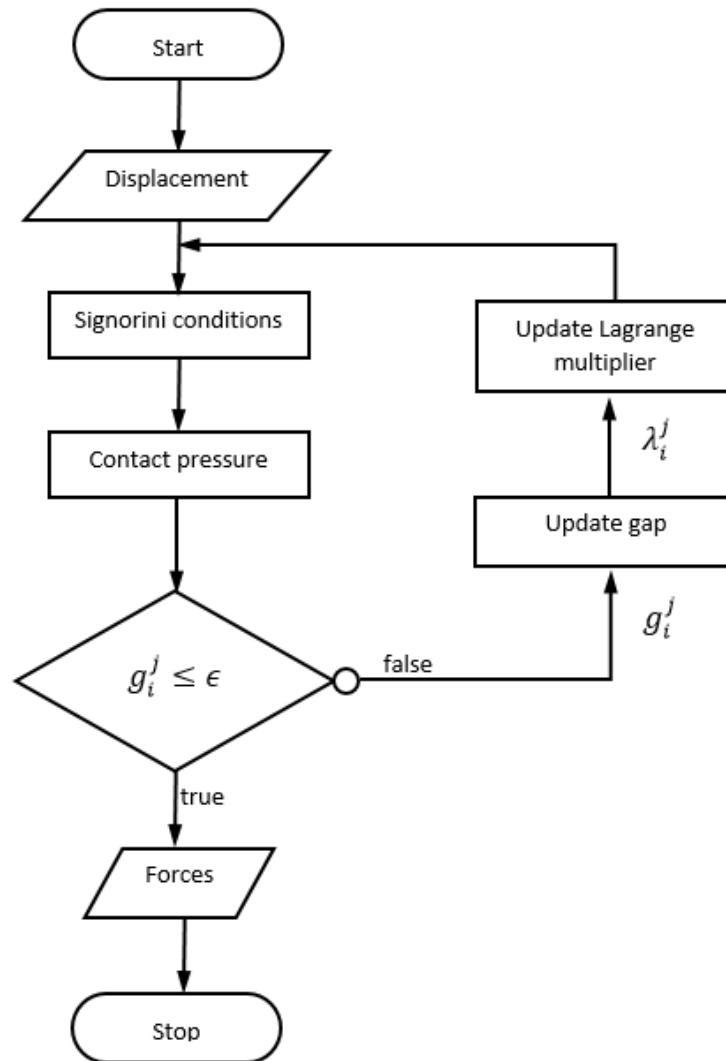


Figure III.12: Flow chart of the contact procedure

#### 4.1 Tooth generation and profile modifications

In this thesis, we focus on spur and helical gears transmitting power between parallel shafts even if the proposed methodology is not limited to these situations. The tooth geometry definition received a particular attention. As mentioned in the first chapter, tooth profile deviation from the theoretical involute tooth profile is of the order of a few micrometers. Therefore an accurate geometry generation is needed. Indeed, the generation is performed using high order Non-Uniform Rational Basis Splines (NURBS) with a high control point number. Compared to splines for which the curve is generated

using polynomial shape functions, NURBS use fractional polynomial shape functions. It is shown in [119, 130] that NURBS lead to better accuracy for contact problems without considering profile deviation.

Here, we introduced two types of tooth deviations from the theoretical involute tooth profile: a longitudinal crowning (see Fig. III.13b) and a linear tip relief (see Fig. III.13a). They are intentional removal of material from gear tooth flanks. They help reducing dynamic loadings and compensate for shafts misalignment and deflections. Longitudinal crowning is generally introduced to maintain the contact at the tooth flank centre and linear tip relief smoothens the meshing transition process. The equations of the longitudinal crowning and the linear type relief are directly introduced in the equation of the involute tooth profile.

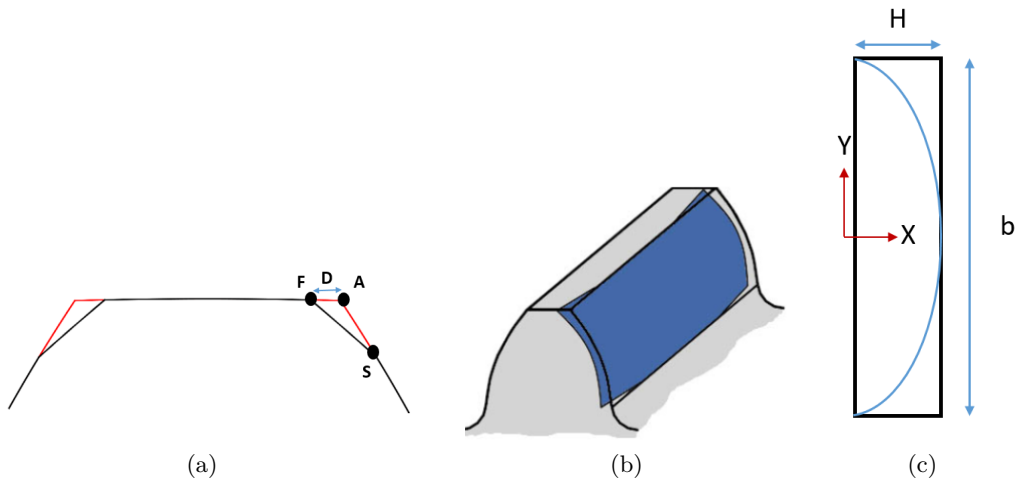


Figure III.13: Description of linear tip relief deviation (a) where  $S$  is the starting point,  $D$  is an amount of profile modification at the tooth tip measured as the distance between point  $A$  and point  $F$ . Longitudinal crowning modification (b) and parameters description from the top (c).  $H$  is the maximum depth of crowning.

## 4.2 Mesh convergence

As explained above, micro-geometry deviations (namely tip relief and longitudinal crowning) are included directly in the 3D geometry, and the hertzian-like deformation induced by the contact between the gear teeth has to be quantified during the application of the proposed methodology.

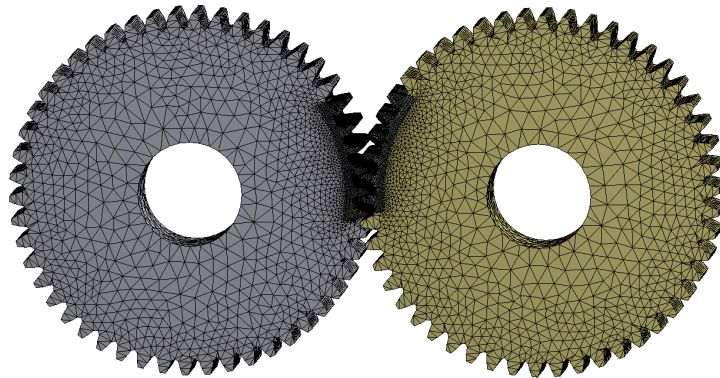
For this purpose, we pay a particular attention to the mesh used and a convergence study on the FE mesh along the tooth was carried out. The procedure is applied for validation on a spur gear pair considering the following gear characteristics (Table III.1). We consider three meshes corresponding to 50, 70 and 100 low order hexahedron elements along the involute profile. It corresponds to a mesh element size of 70  $\mu\text{m}$ , 50  $\mu\text{m}$  and 38  $\mu\text{m}$ , respectively. For these three cases, an equal inflation of 30 layers for the bulk and up to 30 elements along the tooth width (with 0.6 mm length) are introduced. The inflation measures 900  $\mu\text{m}$  with a depth of each layer equal to 30  $\mu\text{m}$ . At the pitch contact point, an estimated shear stress [75] beneath the surface at 900  $\mu\text{m}$  is less than 15% of the maximum value. Additionally, for the different mesh considered, the estimated contact width predicts 3 to 6 elements along this width. This dense mesh size makes us confident to capture edge effects and hertzian-like deformation. Validations will be established by comparing with analytical formula of Hertz theory.

At this stage, our objective is to evaluate and capture the effect of the micro-geometry. So, firstly, we compute the unloaded transmission error for the three meshes.

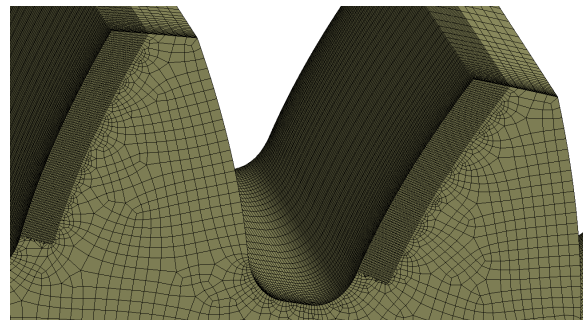
The mesh generation with about 700000 nodes and about 2 million degrees-of-freedom is presented in Fig. III.14 with a close-up (see Fig. III.14b) in the teeth region. The proposed methodology is carried out for a low output torque  $T = 0.5 \text{ N m}$  in order to identify the micro-geometry. The associated unloaded STE is presented in Fig. III.15 for different levels of detail of the tooth mesh. The shape of the curves follows the long tip relief of 5  $\mu\text{m}$  only for an element size lower than 50  $\mu\text{m}$ . The comparison of the unloaded transmission error exhibits the importance of dealing with a specific mesh. With a precision lower than 1  $\mu\text{m}$ , 70 divisions in the involute profile is a necessary condition. We will verify that this condition is sufficient to take into account transmission error under load including global deformation and hertzian-like deformation.

Table III.1: Characteristics of the spur gear

Name	Designation	Gear 1	Gear 2	Unit
Module	$m_n$	2		mm
Number of teeth	$Z$	50	50	-
Pressure angle	$\alpha$	20		deg
Contact ratio	$\epsilon_\alpha$	1.512		-
Base radius	$r_b$	46.985	46.985	mm
Profile shift coefficient	$x$	0	0	-
Addendum	$h_a$	2	2	mm
Dedendum	$h_f$	2.5	2.5	mm
Face width	$b_f$	20	20	mm
Center distance	$a'$	100.5		mm
Tip relief modification				
Starting radius	$r_S$	50.26	50.26	mm
Depth	$D$	5	5	$\mu\text{m}$
Longitudinal crowning modification				
Maximum depth	$H$	0	0	$\mu\text{m}$



(a)



(b)

Figure III.14: (a) the spur gear mesh with low order hexahedron linear element at the tooth and tetra element elsewhere (b) close-up of the tooth mesh with 100 hexa-linear element and an inflation.

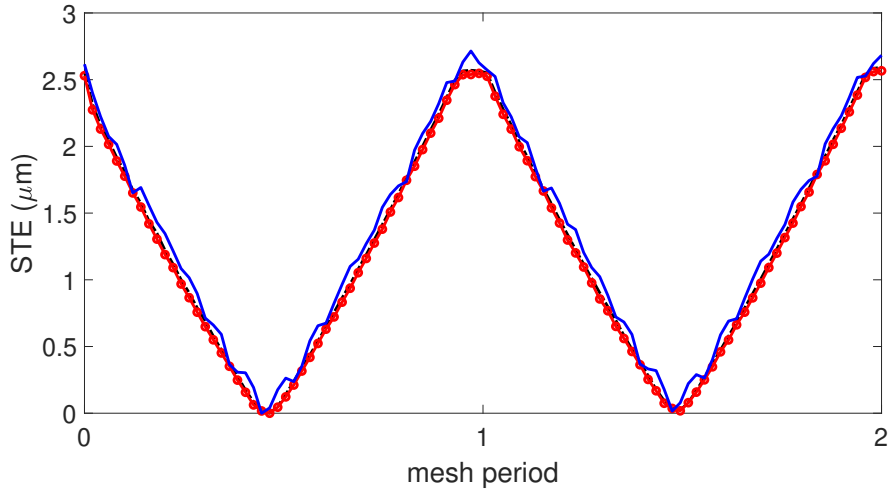


Figure III.15: Unloaded transmission error for coarse mesh (50 divisions, —), intermediate mesh (70 divisions, ●) and fine mesh (100 divisions, - -).

### 4.3 Time cost reduction

The Guyan condensation also called static condensation [56] is largely used in solid mechanics for solving the static analysis of contacting structures. The approach provides an exact solution of nonlinear problems while improving the time cost compared with a direct solving. The idea is to consider two sets of degrees of freedom (DOF), one for active  $u_A$  (contact nodes here) and another complementary  $u_C$ . The DOF separation using the bloc Schur complement of the  $K$  matrix allows the identification of a linear relationship between the two sets of DOF:

$$\mathbf{u}_C = -\mathbf{K}_{CC}^{-1} \mathbf{K}_{CA} \mathbf{u}_A \quad (\text{III.23})$$

where the finite element stiffness  $K$  is split into four blocks:

$$\begin{bmatrix} \mathbf{K}_{AA} & \mathbf{K}_{AC} \\ \mathbf{K}_{CA} & \mathbf{K}_{CC} \end{bmatrix} \quad (\text{III.24})$$

Considering our gear model, about 6000 contact nodes are possibly involved during the contact treatment. A refinement of the mesh at the contact interface leads to full matrices after the condensation on the nonlinear degrees of freedom which are the contact nodes. As a consequence, the matrix

operation shown in the equation (III.23) becomes computationally demanding. To overcome this difficulty, we investigate a direct resolution of the full system using domain decomposition.

Domain decomposition is a parallel computation technique widely used in computational mechanics [83, 103, 153]. It consists in the division of the whole domain in several partitions. The mechanical problem is solved partially on each partition and an update of the interfaces enables communication between the partitions. Herein, we apply a domain decomposition on a cluster using CPU resources (1 computer node = 16 cores, 2.6 GHz and 64 GB RAM) in order to achieve the three steps presented in Fig. III.9, III.10, III.11 . A parametric study on the case presented in Table III.2 is conducted by increasing the CPU resources from 16 cores (1 computer node) to 96 (6 computer nodes). The simulations are benchmarked against the results obtained with the Guyan condensation.

Table III.2: Parametric study on spur gear to reduce the time cost

Simulations	Time cost (s)	Time reduction (%)	Number of cores
REF (Guyan)	144000	-	-
1	53224	63%	16
2	18303	87%	32
3	15286	89%	64
4	19226	86%	96

Table III.2 displays the time cost for simulations over two mesh periods. Figures in Table III.2 show that 64 cores is the best choice for solving the gear contact analysis. Constantly increasing the domain discretization is not leading to a proportional constant time reduction. Indeed, for 96 cores the time reduction percentage (86%) is less than for 64 cores. This is induced by the large number of information transfers needed to communicate between domains. The proposed methodology is thus performed in the following sections by solving the full nonlinear system using 64 cores instead of using Guyan condensation.

#### 4.4 Numerical comparison

The objective of this section is to evaluate the main differences between the proposed multibody methodology and the compliance method described in the first section and based on the eq. (III.15) and (III.16). This compliance approach is implemented in a software named TERRA [102, 112] developed by the joint laboratory "gear dynamics laboratory LADAGE". For this code, the compliance matrix  $H(\theta)$  is computed either with an analytical thick plate model to evaluate the tooth strain energy and a Ritz-Galerkin approximation to evaluate the tooth deflection [42] or a FE model where the line of action is discretized and a constant punctual load is applied. The assessment is made in terms of static transmission error and meshing stiffness fluctuations. The gear transmission presented in Table III.1 is retained for the comparison. The study is performed for various output torques in order to obtain relevant comparative results. Then, the potential effects on the dynamic behaviour are discussed.

##### *Static transmission error:*

A series of nonlinear analyses are carried out for different output torques and a map of the static transmission error is built. Fig. III.16a and Fig. III.16b are respectively the maps of the STE using the proposed methodology and the compliance method. The gear mesh procedure is properly handled by the proposed methodology and the periodicity of the STE is well represented. Fig. III.16a and Fig. III.16b show a good match between the transmission curves for an output torque from 0.5 N m to 50 N m. Indeed, the tip relief of  $5\mu\text{m}$  is clearly identified by both approaches. However, for a torque level up to 50 N m, the compliance method underestimates the mean values of the STE while the STE shapes have a smoother variation using the proposed methodology. In fact, the transition from one tooth pair to another is progressively handled as shown in Fig. III.17. Indeed, in Fig. III.16b, a

sudden variation of the STE is visible for a torque equal to 50 N m which can be explained by a brutal transition of the number of teeth pair involved during the contact treatment. This phenomenon is amplified as the torque is increased. In the compliance method, the contact lines positions and orientations and therefore the contact ratio of the gear pair (expressed as  $\epsilon_\alpha = g_\alpha/p_b$  while  $g_\alpha$  is the length of path of contact and  $p_b$  is the base pitch) are determined a priori. This explains the brutal variation of the STE.

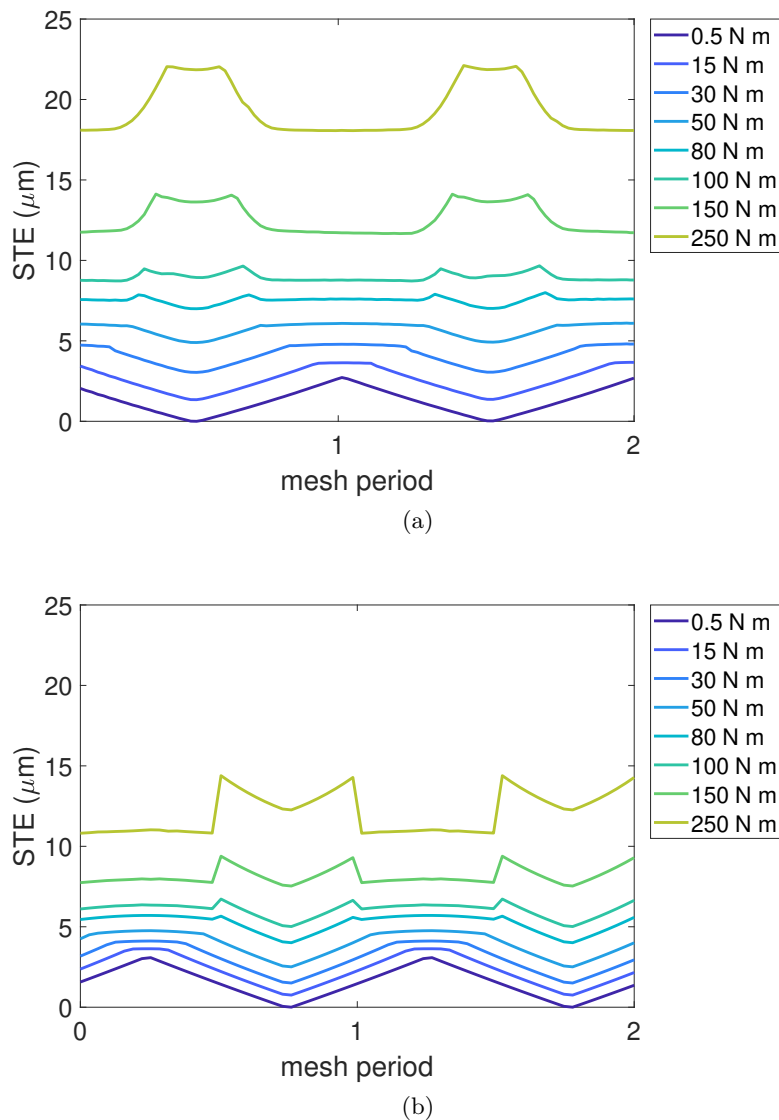


Figure III.16: The static transmission error for different torque levels  $T = [0.5, 15, 30, 50, 80, 100, 150, 250]$  N m and over two mesh periods. Numerical results through ANSYS Mechanical  $\text{\textcircled{R}}$  solver (a) and the compliance method (b).

Moreover, the map brings to light the nonlinear variation of the STE with respect to the load. The peak to peak transmission error (PPTE) is measured from the STE map for the proposed methodology (Fig. III.16a) and the compliance method (Fig. III.16b) in order to highlight the relation between load and deformation. The variations of the PPTE presented in Fig. III.18 allow an estimation of an optimal torque. Indeed, the PPTE amplitude of the compliance method decreases until a minimum value for an output torque close to  $T = 70 \text{ N m}$ , whereas for the proposed methodology the minimum value is reached for an output torque  $T = 100 \text{ N m}$ . The optimal torque ranges for the compliance method and the proposed methodology are respectively  $[80, 150] \text{ N m}$  and  $[60, 110] \text{ N m}$ . Differences in the estimation of the optimal torque and the mean value of the STE can be explained on the one hand by the method retained in the classical strategy for the computation of the compliance matrix  $H(\theta)$  and on the other hand by the number of teeth detected during the contact treatment as mentioned above. These differences can lead to an imprecise micro-geometry optimization when using hybrid FE-analytical methods.

### *Mesh stiffness:*

The different mesh stiffness are evaluated for the output torques  $T = [0.5, 15, 30, 50, 80, 100, 150, 250] \text{ N m}$  over two mesh periods. The mean value and the fluctuations of the mesh stiffness of the proposed methodology and the compliance method are both governed by the output torque as shown in Fig. III.19. It appears three ranges of variation corresponding to: low torque  $[15, 50] \text{ N m}$ , medium torque  $[50, 100] \text{ N m}$  and high torque  $[100, 250] \text{ N m}$ .

The mean values of the different mesh stiffness computed through the proposed methodology are half of the ones obtained with the compliance method. The critical modes which are the modes for which the strain energy contribution at the mesh is maximum are governed by the mean value of the mesh

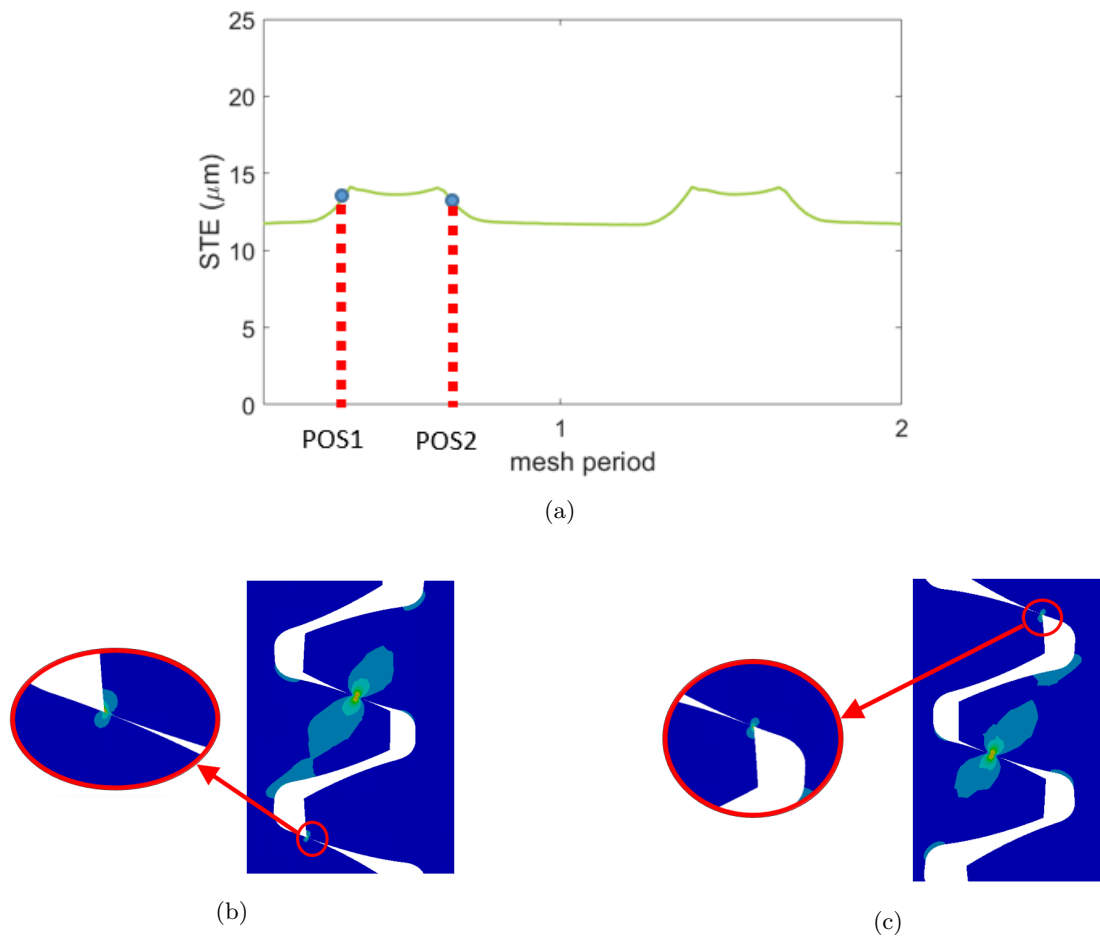


Figure III.17: STE for 150 Nm with two contact positions named POS1 and POS2 (a). A close-up at the contact POS1 (b) and POS2 (c).

stiffness. The critical frequencies of the system are thus re-ordered. This change affects the critical operating speeds of the system. In addition to this, as shown in Fig. III.19, the fluctuations of the different mesh stiffness are also half of the ones obtained for the proposed methodology compared with the compliance method. Obviously, the mean values of the different mesh stiffness are different since the flexibility of the gear body is not taken into account in the compliance method. However, differences are also related to the fact that the compliance method does not allow a good description of the contact treatment between the gear teeth and also the hertzian-like deformation. In contrast, the proposed approach based on a multibody description and a surface-to-surface contact element

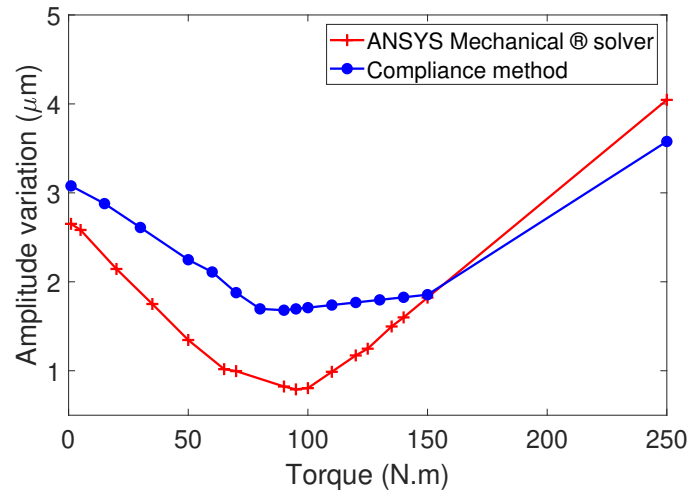


Figure III.18: Comparison of the different peak to peak transmission error (a): — compliance method, and — ANSYS Mechanical ® solver.

allows an accurate contact treatment since no assumption are made on the contact point locations and the global and local deformation are taken into account. The large variation observed modifies the parametric phenomena and the amplitude of resonance of the dynamic response [131].

#### *Normal contact characteristics of mating gear teeth:*

It is of paramount importance to evaluate the normal characteristics of mating gear teeth. The local contact behaviour is often modelled with Hertz theory [75]. It is an efficient way to approximate local deformations and to predict contact areas. Herein, the proposed methodology through ANSYS Mechanical ® solver provides stress, contact pressure and contact area with no assumption of the contact curvature. The objective of this section is thus to compare the physical quantities determined and quantified with the proposed methodology and those obtained with analytical formula of Hertz theory for two infinite cylinders under load [75].

The cylindrical hertzian contact stress theory for two infinite cylinders under load is based on the

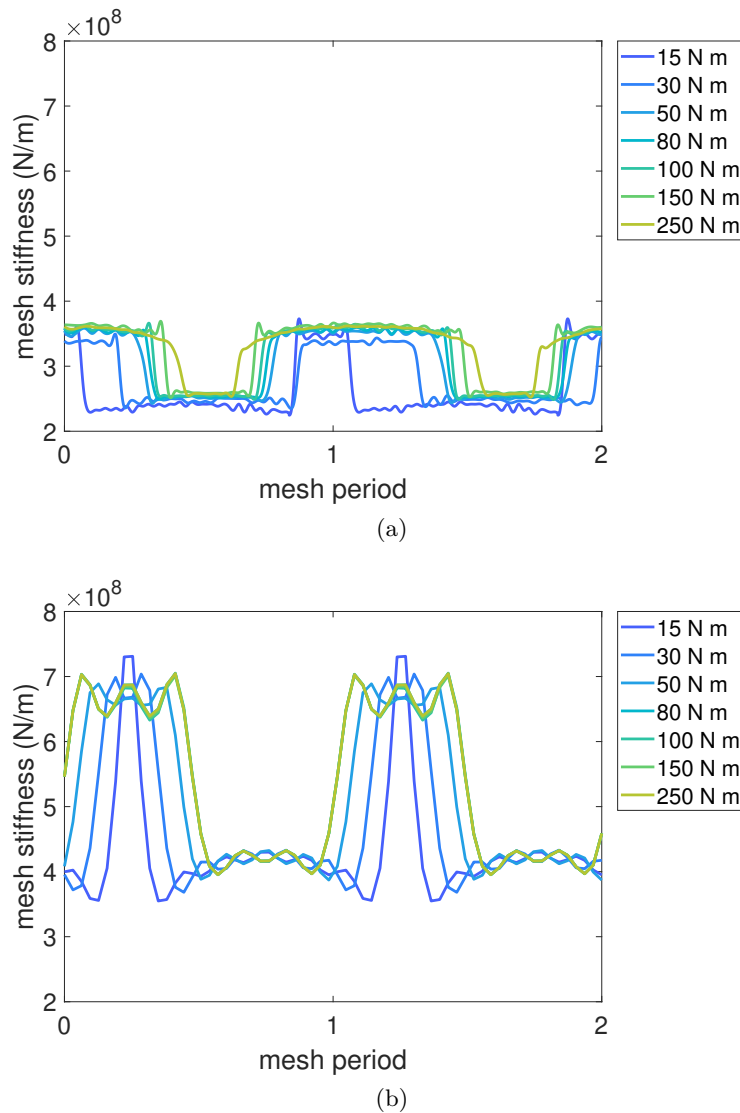


Figure III.19: Mesh stiffness for different torque levels  $T = [15, 30, 50, 80, 100, 150, 250]$  N m: (a) ANSYS Mechanical<sup>®</sup> solver and (b) compliance method.

following assumptions:

- the surfaces are continuous and non-conforming.
- Each interacting body is considered as an elastic half-space with small strains.
- It is a frictionless contact.
- The contact areas are small compared to the size of the radii of curvature of surfaces.

The curvature radii at the contact point of two cylinders are represented in gears by the tangential

segments of the base radii connected to the contact point. For a contact point close to the pitch radius, the contact width  $h$ , the contact depth  $z_0$ , the maximum pressure  $P_0$  and the maximum shear stress  $\tau$  as described in Fig. III.20 are compared with the proposed methodology (see Table III.3). The contact width is accurately approximated with the proposed methodology. Indeed, as shown in Table III.3, the approach generates  $229\mu\text{m}$  of contact width and  $204\mu\text{m}$  is accounted for Hertz theory. Additionally, the contact analysis converged in terms of maximum pressure and maximum shear stress as depicted in Table III.3 where only 20 MPa of differences with Hertz are measured. The results obtained with the proposed approach are thus in good agreement with the those acquired by Hertz theory. In contrast, these physical quantities cannot be retrieved directly with a compliance method. It requires additional analyses.

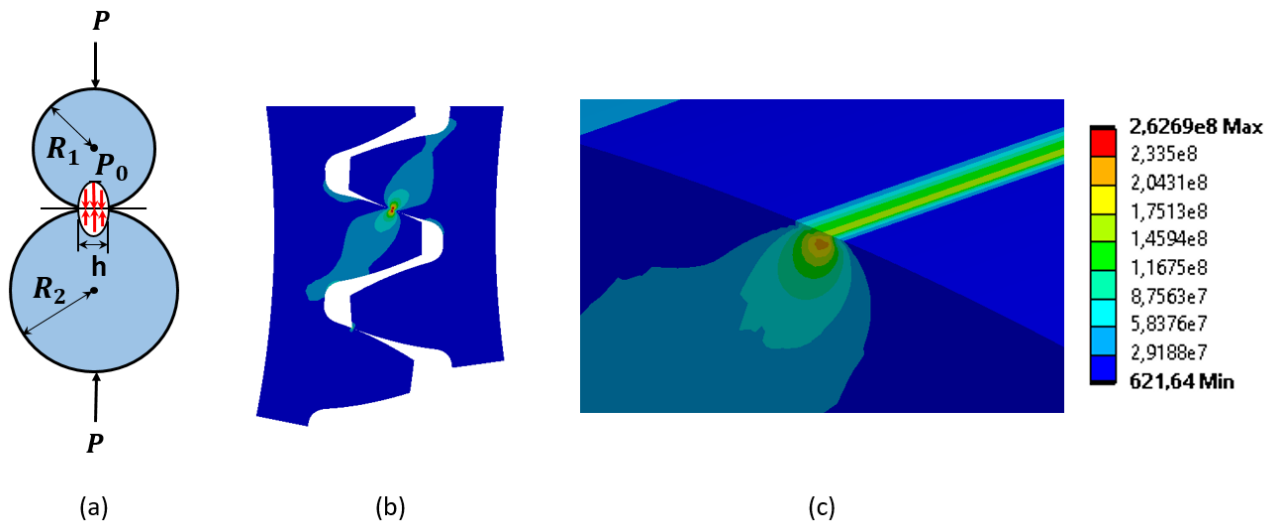


Figure III.20: (a) Description of the cylindrical contact stress claimed by Hertz theory, (b) shear stress for a torque of  $T = 100\text{ N m}$  and (c) a close-up of the shear stress in Pa at the middle of the tooth width is depicted.

## 5 Conclusion

This chapter introduces a fully FE-based method to compute the static transmission error and the mesh stiffness. The proposed methodology deals with gear mesh contact and is based on a fully flexible

Table III.3: Comparative study on spur gear with Hertz theory

Physical quantities	Analytical results of Hertz theory	Proposed approach	Difference (%)	Unit
$h$	204	229	12	$\mu\text{m}$
$P_0$	663	643	3	MPa
$\tau$	199	221	11	MPa
$z_0$	79.5	98.3	23	$\mu\text{m}$

multibody description considering a surface-to-surface contact algorithm. The contact is solved by combining Signorini conditions and an augmented lagrangian formulation.

Elements of validation have been established in terms of mesh settings, contact settings and loading conditions. Additionally, a domain decomposition is used to enable the computation of the static transmission error and the mesh stiffness in reasonable time as opposed to Guyan condensation.

The main contributions of the proposed methodology are to consider a FE-based contact without assumptions about the contact lines positions and orientations, to detect with precision the micro-geometry using NURBS and a fine mesh, to capture the local hertzian-like deformation of the loaded tooth during the meshing process, to recover instantaneously static transmission error, mesh stiffness, root stress and normal contact characteristics of the tooth, and to take into account the flexibility of many mechanical components of a gear transmission.

It was demonstrated that the investigated method can simulate large sort of gears. Besides, quasi-static numerical results of spur and helical gears showed differences in terms of static transmission and mesh stiffness compared with the compliance method. Indeed, a smoother transition from one tooth to another is identified. The mean values and the fluctuations of the different mesh stiffness are half of those obtained with the compliance method. These results have significant influences on the

vibroacoustic behaviour of gears. The differences are mainly due to the multibody description and the contact element used in the proposed methodology.

The objective of the next chapter is to show the potential of the proposed methodology to compute the static transmission and the mesh stiffness of gears including shafts, bearings and the housing. The methodology will be also applied to lightweight gear in order to put forward specific phenomena that cannot be identified with hybrid FE-analytical approaches.

# IV

## Application of the proposed methodology

---

### Introduction

---

The objective of this chapter is to show the capability of the proposed methodology detailed in the previous chapter. For this purpose, several gear transmissions are evaluated. Cases of spur and helical gears transmitting power between parallel shafts are studied. Gear transmissions with flexible shafts, bearings and the housing are also considered. A particular attention is devoted to gear with holed gear blanks for which an original 2D method is derived and assessed to reduce the computational time.

---

### Contents

---

1	State of the art: particularity of lightweight gears . . . . .	68
2	Effect of micro-geometry and the flexibility of the transmission . . . . .	69
3	Effect of gear body with holes . . . . .	76
4	2D quasi-static decomposition method . . . . .	79
	4.1 Problem formulation . . . . .	79
	4.2 Numerical validations . . . . .	82
5	A parametric study of the effect of number and radial position of holes in gear blanks	88
	5.1 Problem description . . . . .	88
	5.2 Effect of number and radial position of holes . . . . .	89
6	Conclusion . . . . .	90

---

## 1 State of the art: particularity of lightweight gears

The issues related to energy consumption and air pollution have increased the need for on-board mass reduction. This requirement concerns in particular drivelines equipped with gear transmissions. The proposed solutions to decrease the gear mass consists in using composites [24, 25] or removing material from the gear blanks by employing thin rim or holes.

If we assume identical teeth, axisymmetric gear bodies, no eccentricity and no pitch errors, the STE exhibits periodic fluctuation at the mesh frequency  $f_m$ . If only one wheel presents eccentricity defect or a holed gear blank, the fundamental frequency corresponds to the rotating frequency of the considered wheel  $f_1$  or  $f_2$ . If both driving and driven wheels have eccentricity defects or holes, the fundamental frequency of the STE  $f_0$  is associated to the period  $T_0$  needed to re-establish contact between a particular tooth of the driving wheel and a particular tooth of the driven wheel.

$$f_0 = \frac{1}{T_0} = \frac{f_m}{Z_1 Z_2} = \frac{f_1}{Z_2} = \frac{f_2}{Z_1} \quad (\text{IV.1})$$

The classical approaches presented in the previous chapter are not adapted for dealing with a variation of material in the gear blank. However, some improvements have been made in the last few years in order to include lightweight gear bodies in the static transmission error analysis. Guilbert *et al.* [53, 54, 55] proposed a condensed finite element sub-structure connected to a lumped parameter model. They paid attention to the mesh interface model to connect a lumped parameter with a FE model. The contact occurs on the theoretical contact lines and the flexibility of the gear teeth is described through several independent stiffness elements distributed along the line of action. The effects of a thin rim wheel or holes in the gear blanks were assessed [52]. The presence of holes modulates the STE. Additionally, Shweiki [122] used several nonlinear FE simulations with high detailed model of the meshing gears to estimate the STE fluctuations. Cappellini [20] and Shweiki [123] also combined a

FE approach and an analytical representation of the gear mesh stiffness to investigate the behaviour of lightweight gears. The total deformation of the gear induced by the gear mesh contact is modelled as a global contribution coming from the tooth deflection, mainly bending and shear, and a local nonlinear hertzian-like deformation. Active tooth pair are divided into multiple slices along the width and the contact points are considered to lie on the rigid involute profile. They also decreased the computation time of the global deformation by performing a model order reduction obtained from a series of linear static analyses where a normal load is applied on selected nodes belonging to theoretical contact lines [20]. Hou *et al* [66] investigated the effect of thin rimmed gears on the NVH performance. Similarly to Rigaud, Hou *et al* showed that thin rim in the gear blanks modifies the mean and the peak-to-peak value of the STE. This modification is used to optimize the thin-rimmed gears and to reduce the gear mass about 25% and the dynamic mesh forces about 68%. Harris *et al* [62, 63] proposed a gear blank tuning by performing two analyses. The first analysis considers the gear mesh between two holes whereas the second analysis considers the gear mesh over hole. This process is carried out on each design iteration in order to select an optimized design for the both analyses. The optimized gear blank geometry leads to a decrease in sound power of 10 dB compared to a standard gear. In the first part of this chapter, we evaluate the transmission error for well-known examples but also for a complete gearbox in order to couple the global deformation of the gearbox and the contact at the gear teeth. The second part is dedicated to holed gear blanks and the original approach proposed to accelerate the simulation.

## 2 Effect of micro-geometry and the flexibility of the transmission

The study carried out in this section, applies the proposed multibody approach to several gear transmissions in order to show the large possibility of the method and to bring to light some phenomena. The gear pairs are classified in several test cases. The first case compares a gear pair with a longitudinal

crowning to a gear pair without. Then, the effect of thin rim and flexible shafts on spur gear is evaluated. In addition, complete gear transmissions are considered including flexible shafts, additional stiffness for bearings and the housing.

**Effect of crowning:** The reverse helical gear pair with longitudinal crowning, also defined for a 100 N m nominal torque, is described in Table IV.1 and its geometry is reported in Fig. IV.1. This gear pair is compared with the same helical gear pair without crowning modification. A control node is defined at each gear centre to apply boundary conditions. Translations of the gear pair are prevented for each control node. Control nodes of the driving and the driven gears are used to apply the driving rotation  $\theta_1$  and the output torque  $T$ . Fig. IV.2 displays the STE fluctuations of the helical gear pairs. The longitudinal crowning modifies the shape of the STE and it appears a larger curvature as shown in Fig. IV.2b. The peak to peak amplitude increases significantly until it reaches  $2\mu\text{m}$  compared with the standard helical gear pair (see Fig. IV.2a). These effects on the STE are explained by the fact that the contact force is localized at the tooth flank center.

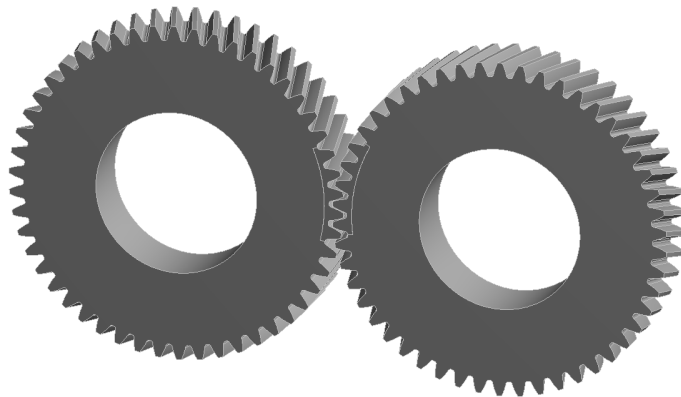


Figure IV.1: Helical gear pair.

**Effect of thin rim and flexible shafts:** This section analyzes the influence of a thin rim wheel and flexible shafts on the STE fluctuations. The thin rim is located in the midplane of the gears but the gears are not at the center of the shafts in order to accentuate possible rotation of the tooth flank in

Table IV.1: Gear characteristics of the helical gear pairs.

Name	Designation	Gear 1	Gear 2	Unit
Module	$m_n$	2		mm
Number of teeth	$Z$	50	50	-
Pressure angle	$\alpha$	20		deg
Helix angle	$\beta$	15		deg
Total contact ratio	$\epsilon_t$	2.275		-
Base radius	$r_b$	48.439	48.439	mm
Profile shift coefficient	$x$	0		-
Addendum	$h_a$	2		mm
Dedendum	$h_f$	2.5		mm
Face width	$b$	20		mm
Center distance	$a'$	104		mm
Tip relief modification				
Starting radius	$r_S$	52.024	52.024	mm
Depth	$D$	5	5	$\mu\text{m}$
Longitudinal crowning modification				
Maximum depth	$H$	10	10	$\mu\text{m}$

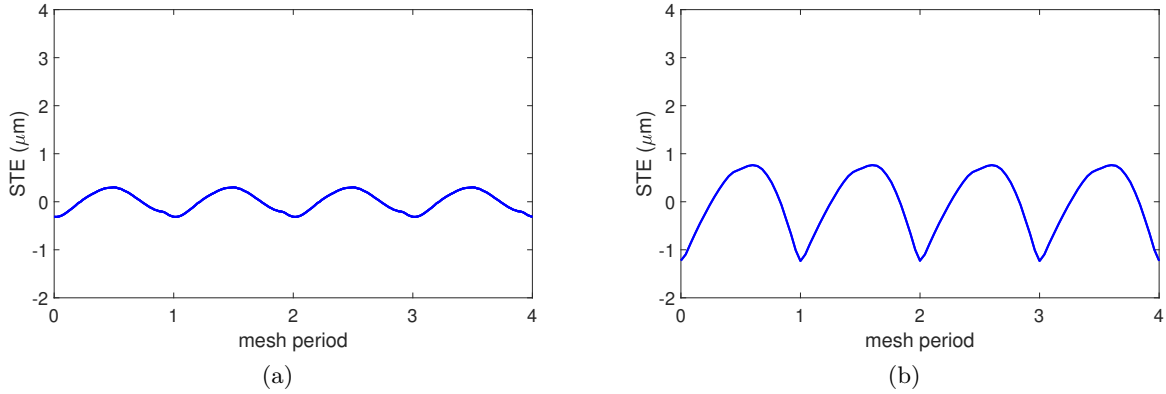


Figure IV.2: Fluctuation of the static transmission error over 4 mesh periods for an output torque  $T = 115 \text{ N m}$ : (a) helical gear without longitudinal crowning, (b) helical gear with longitudinal crowning of  $10 \mu\text{m}$ .

the plane of action. The Table IV.2 described in detail the micro and macro geometry and the gear pair is depicted in Fig IV.3. A control node is defined at each face centre of the driving and driven shafts to apply boundary conditions and prevent the translation of the shafts. The control nodes of the driving and the driven shafts are used to apply the driving rotation  $\theta_1$  and the output torque  $T$ .

The STE fluctuations are compared with those presented in Fig. III.18, for which a spur gear without thin rim and shafts is considered. The shape of the curve is modified and the peak to peak amplitude is increased from  $1 \mu\text{m}$  (see Fig. III.18) to  $4 \mu\text{m}$  (see Fig. IV.4).

Table IV.2: Gear characteristics of the spur gear with thin and flexible shafts.

Name	Designation	Gear 1	Gear 2	Unit
Module	$m_n$	2		mm
Number of teeth	$Z$	50	50	-
Pressure angle	$\alpha$	20		deg
Contact ratio	$\epsilon_\alpha$	1.512		-
Base radius	$r_b$	46.985	46.985	mm
Profile shift coefficient	$x$	0	0	-
Addendum	$h_a$	2	2	mm
Dedendum	$h_f$	2.5	2.5	mm
Face width	$b$	20	20	mm
Center distance	$a'$	100.5		mm
Tip relief modification				
Starting radius	$r_S$	50.26	50.26	mm
Depth	$D$	5	5	$\mu\text{m}$
Rim wheel dimension				
Rim width	$b_w$	8	8	mm
Shaft dimension				
Shaft length	$L$	300	300	mm

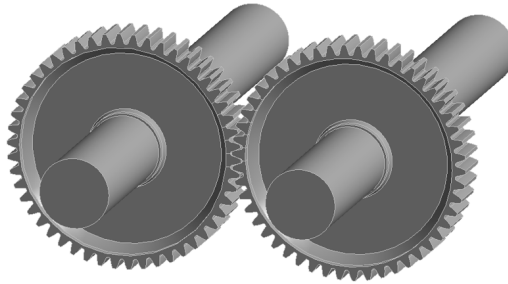


Figure IV.3: Spur gears with thin rim and flexible shafts

Moreover, the deformation of the shafts induces a misalignment as shown in Fig. IV.5a. Indeed, the contact pressure is partially distributed on the tooth flank when the gear teeth are in contact. This particularity is accounted in-line with the multibody approach which is not the case for a classical

approach for which the contact is based on the theoretical contact lines. All couplings of the gear transmission are taken into account during the STE computation and this affects significantly the contact pressure distribution and the STE fluctuations. The proposed approach based on FE contact allows an accurate description of the contact condition without additional geometrical consideration and taking into account micro-geometry deviations.

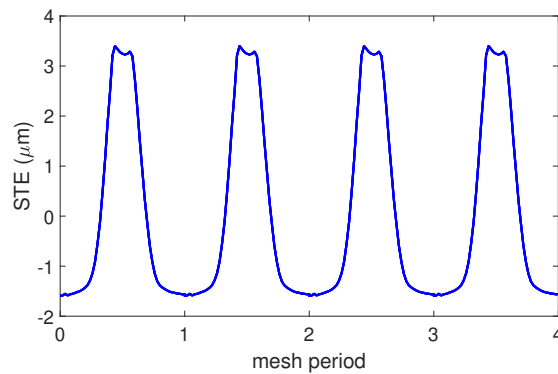


Figure IV.4: Fluctuation of the static transmission error over 4 mesh periods for an output torque of 115 N m.

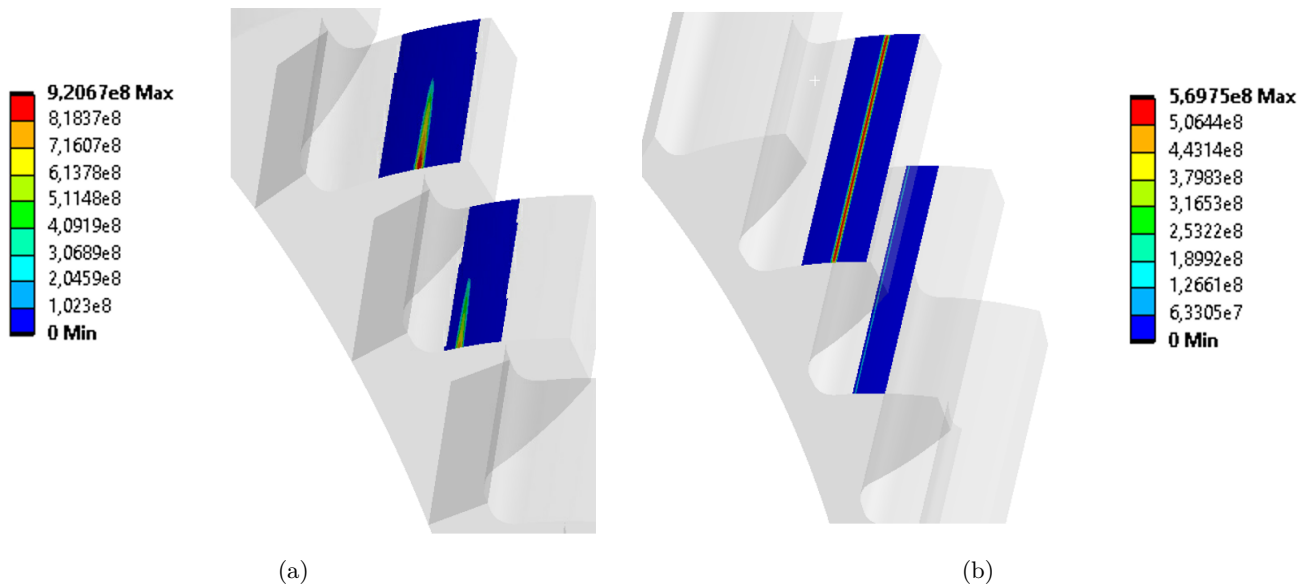


Figure IV.5: Contact pressure distribution on the mating teeth in Pa: (a) spur gear with thin rim and flexible shafts, (b) standard spur gear.

***Effect of flexible shafts, bearing and the housing:*** The objective of this section is to show the

influence of the flexible shafts, bearings and the housing on the static transmission error. To this end, two gearboxes of spur gears have been build (see Fig. IV.6). The first one with long shafts and the second one with short shafts. The global deformation of shafts induces misalignment. For the model with short shafts, the gear pair are at the center of the shafts which is not the case for the model with long shafts. The gearbox with long shafts will induce more misalignment. Gears, shafts and the housing are modelled as 3D finite elements. For the sake of simplicity, the bearing are linearized at the output torque of  $T = 115 \text{ N m}$  and considered as additional stiffness in the gearbox model. The values of the bearing stiffness are obtained from a commercial software named Romax.

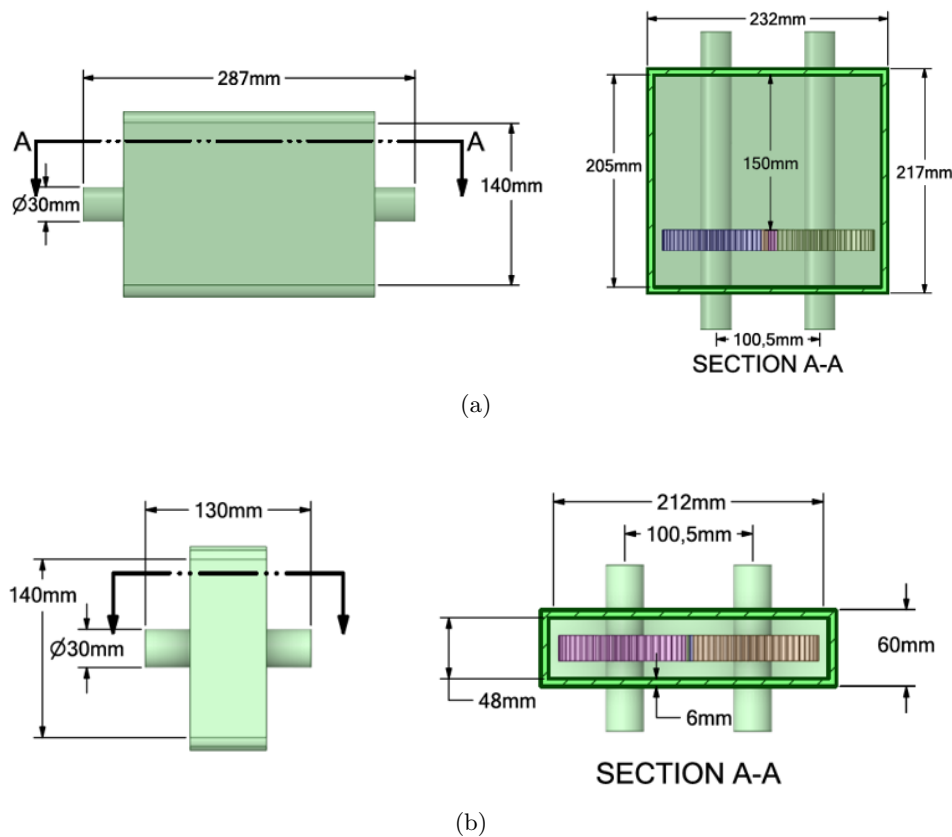


Figure IV.6: Characteristics of the gearboxes with long shafts (a) and short shafts (b).

For the gearboxes, shafts, bearings and the housing are modelled as a condensed substructure using a static condensation of Guyan as detailed in section 4.3. At this stage, the Guyan condensation is

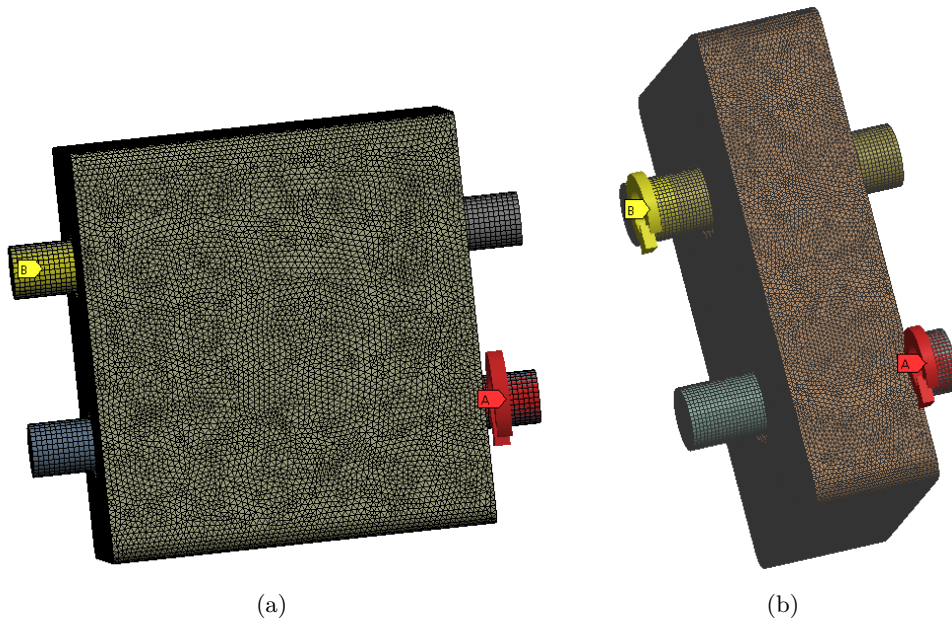


Figure IV.7: FE models of the Gearbox with long shafts (a) and with short shafts (b).

useful since the contribution of shafts, bearings and the housing are accounted for a small number of active nodes as opposed to the use in section 4.3. Indeed, here, the active nodes are represented by control nodes located at the center of the input/output gear and nodes at the location of the boundary condition. Moreover, the Guyan condensation gives an exact solution of the model since no approximation of the solution is made. The input rotation and the output torque of  $T = 115 \text{ N m}$  are applied on the input/output shafts, respectively. The two housing are fixed at their ground to prevent the motion of these faces. The finite element model of the long and short gearbox (see Fig. IV.7) are about 2.8 millions of DOF and 2.2 millions of DOF, respectively. Results are presented in Fig. IV.8. The peak-to-peak amplitudes for the gear pair only, the gearbox with short and long shafts are respectively  $1 \mu\text{m}$ ,  $2 \mu\text{m}$  and  $4 \mu\text{m}$ . We can see that the STE of the gearboxes is modified for both, short and long shafts. Indeed, the shape of the STE is lightly affected but the peak-to-peak amplitude is clearly increased compared to the STE of the gear pair. The misalignment induced by the long shafts are have a significant influence on the STE fluctuations.

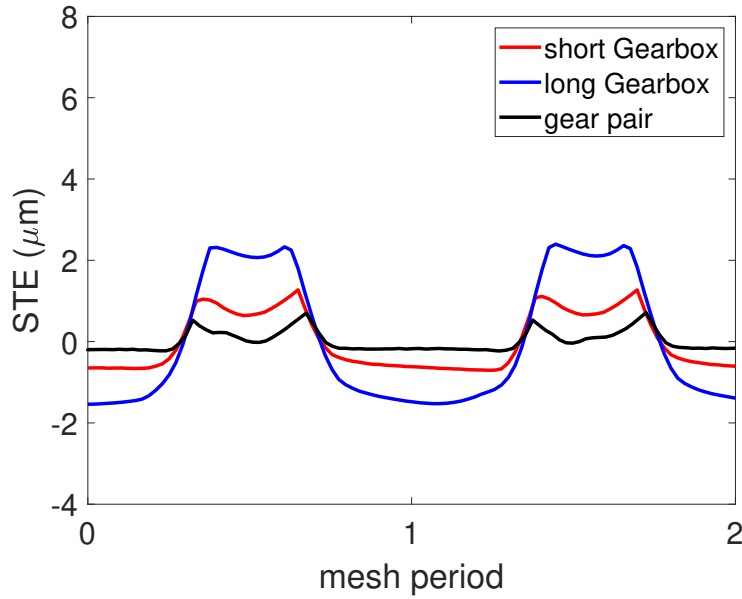


Figure IV.8: Fluctuation of the static transmission error for the two gearboxes and the gear pair only for an output torque of 115 N m.

### 3 Effect of gear body with holes

This part investigates the influences of holed gear blanks on the STE fluctuations. For this purpose, we consider two gear pairs, a spur gear with 8 holes on each gear bodies and a large rim (see Fig. IV.9a) and a helical gear with 8 holes and a center thin rim (see Fig. IV.9b). The gear characteristics for the spur and helical gear are depicted in the the Tables IV.3 and IV.4, respectively.

A control node is defined at each gear centre to apply boundary conditions. The translations of the gear pair are prevented for each control node. The control nodes of the driving and the driven gears are used to apply the driving rotation  $\theta_1$  and the output torque  $T$ .

Fig. IV.10 and IV.11 displays STE fluctuations and the frequency spectrum of the spur and helical gear. Holes in gear blanks are responsible for additional harmonic components, especially at low frequency. Indeed, a harmonic corresponding to the number of holes is created and this amplitude exceeds the mesh harmonic (see Fig. IV.10b and Fig. IV.11b).

The harmonic content show also the existence of sidebands. Considering  $H_Z$  and  $H_{N_H}$  which are

respectively the mesh harmonic and the harmonic of holes, we can identify sidebands as  $H_{sb} = H_Z \pm H_{N_H}$ . For example on the Fig. IV.10b and IV.11b we see the harmonics  $H_{42}, H_{50}$  and  $H_{58}$ .

So, changes in gear blank topology increase the harmonic content of the STE. This phenomena is not properly handled within the classical strategies.

Table IV.3: Gear characteristics of the spur gear with holed gear blanks.

Name	Designation	Gear 1	Gear 2	Unit
Module	$m_n$	2		mm
Number of teeth	$Z$	50	50	-
Pressure angle	$\alpha$	20		deg
Contact ratio	$\epsilon_\alpha$	1.512		-
Base radius	$r_b$	46.985	46.985	mm
Profile shift coefficient	$x$	0	0	-
Addendum	$h_a$	2	2	mm
Dedendum	$h_f$	2.5	2.5	mm
Face width	$b_f$	20	20	mm
Center distance	$a'$	100.5		mm
Tip relief modification				
Starting radius	$r_S$	50.26	50.26	mm
Depth	$D$	5	5	$\mu\text{m}$
Lightweighting				
Number of holes	$N_H$	8	8	-
Radius of holes	$r_H$	20	20	mm

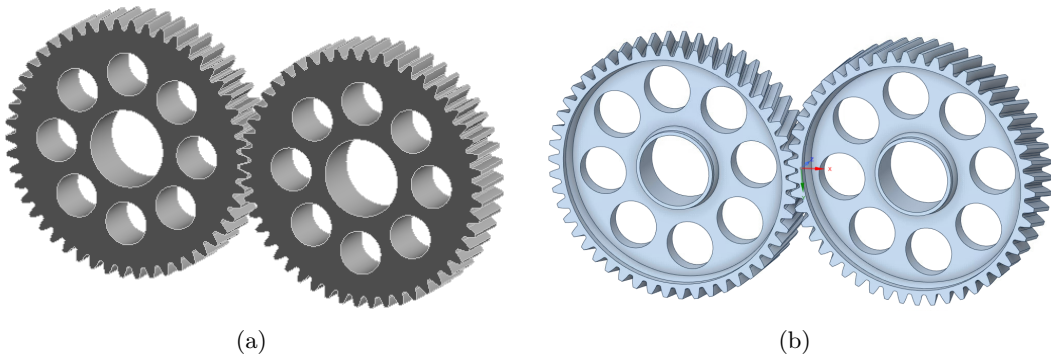


Figure IV.9: Spur gear pair with holed gear blanks and large rim (a) and helical gear with holed gear blanks and thin rim (b).

The analysis of such systems is computationally demanding mainly due to the large size of the finite

Table IV.4: Gear characteristics of the helical gear pair with holed gear blanks and thin rim.

Name	Designation	Gear 1	Gear 2	Unit
Module	$m_n$	2		mm
Number of teeth	$Z$	50	50	-
Pressure angle	$\alpha$	20		deg
Helix angle	$\beta$	15		deg
Total contact ratio	$\epsilon_t$	2.275		-
Base radius	$r_b$	48.439	48.439	mm
Profile shift coefficient	$x$	0		-
Addendum	$h_a$	2		mm
Dedendum	$h_f$	2.5		mm
Face width	$b$	20		mm
Center distance	$a'$	104		mm
Tip relief modification				
Starting radius	$r_S$	52.024	52.024	mm
Depth	$D$	5	5	$\mu\text{m}$
Lightweighting				
Number of holes	$N_H$	8	8	-
Radius of holes	$r_H$	20	20	mm
Rim wheel dimension				
Rim width	$b_w$	8	8	mm

element model used to describe the system and the nonlinear behaviour arising from the contact between the gear teeth. To reduce computation time, we propose an original 2D decomposition method. This method is derived in the following section.

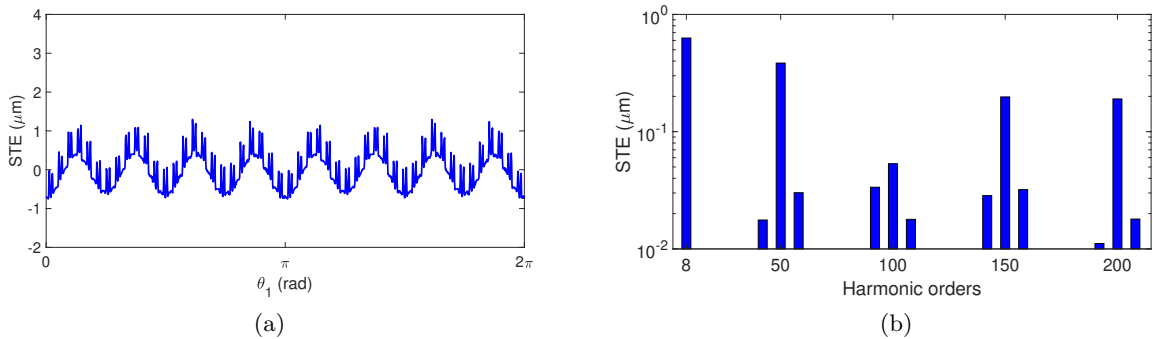


Figure IV.10: Fluctuation of the static transmission error of the gear pair with holes (a) and frequency spectrum (b) for an output torque  $T = 115 \text{ N m}$ .

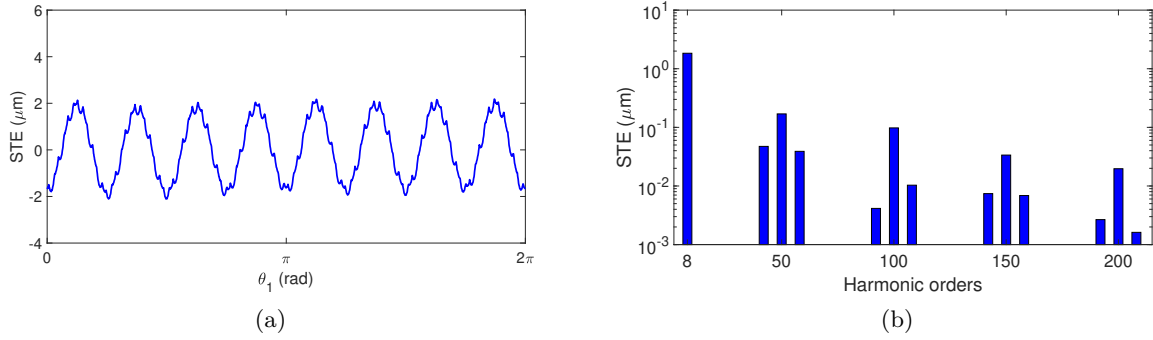


Figure IV.11: Fluctuation of the static transmission error of the helical gear pair with thin rim and holes (a) and frequency spectrum (b) for an output torque  $T = 115 \text{ N m}$ .

## 4 2D quasi-static decomposition method

### 4.1 Problem formulation

This section describes the strategy used to decompose the deformation of the gear body with holes and the deformation induced by the contact between gear teeth. The proposed method is mostly based on the assumption that the tooth deflection is not coupled to the deformation of the gear body, so that its behaviour can be accounted for with an additional flexibility. The following developments present the substructuring of gears with identical and equidistant holes in the gear blanks. The objective is to estimate the instantaneous deformation of the holed gear blank and the gear teeth. The system is decomposed into two substructures as shown in Fig. IV.12. The first one referred to as "gb", represents only the elastic holed gear body with a radius  $R_w$ . The second one, labelled "wh", is the complementary part of the gear pair where the holed gear blank is replaced by a rigid wheel.

The decomposition method presented in this section takes only into account rotation around shaft axis which means that a possible twist of the tooth flank in the plane of action is neglected. This constitutes the main limitation of the proposed method, although it can be extended to 3D rotations with additional research. It still provides a significant computational time reduction when studying gears without thin-rimmed bodies.

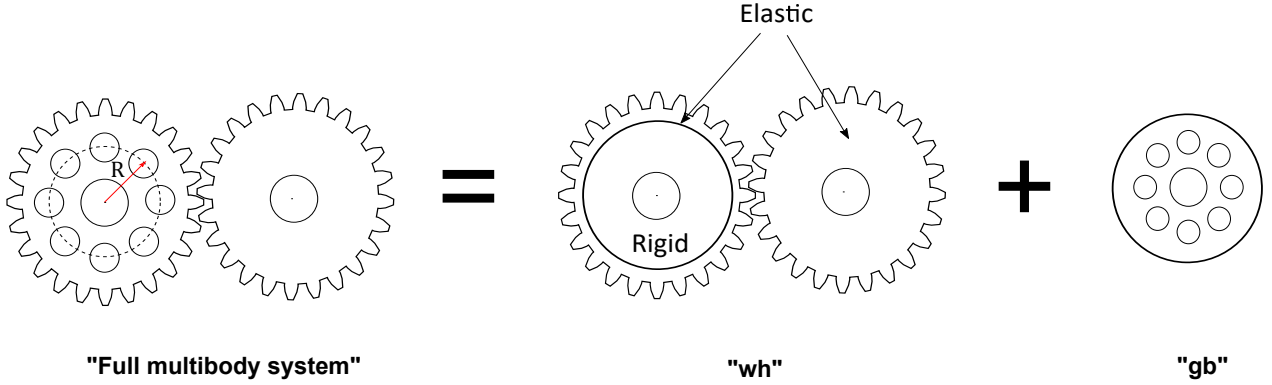


Figure IV.12: Decomposition of gear pair with holes

The decomposition method is thus structured as follows:

- Firstly, the fully finite element approach described in section 3 is applied to the second substructure "wh". For this substructure, the simulation is performed over one mesh period since the holed gear blank is not considered. The substructure is discretized by the FE method. The equation of motion of substructure "wh" is expressed as follows:

$$\mathbf{M}_{wh}\ddot{\mathbf{u}}_{wh} + \mathbf{C}_{wh}\dot{\mathbf{u}}_{wh} + \mathbf{K}_{wh}\mathbf{u}_{wh} + \mathbf{F}_{wh}^{nl}(\mathbf{u}_{wh}, \theta_1) = \mathbf{f}_{wh}^{ex} \quad (\text{IV.2})$$

The resulting static transmission error named  $\delta_{wh}(\theta_1)$  is:

$$\delta_{wh}(\theta_1) = R_{b2}\theta_2^{wh} - R_{b1}\theta_1^{wh} \quad (\text{IV.3})$$

$\theta_1^{wh}, \theta_2^{wh}$  are respectively the angular displacement measured at the centre of the driving and driven gears.

- Next, the quasi-static motion of the full multibody system shown in Fig IV.12 corresponding to an amplitude  $2\pi/N_h$  is discretized in 16 angular positions. For each angular position, the fully multibody method is applied and the tangential displacement field at the interface between "wh" and "gb" is extracted. This displacement is then introduced as an imposed displacement on the substructure "gb" while applying the output torque at the centre. Considering  $\mathbf{u}_{gb}^{in}$  and  $\mathbf{u}_{gb}^{ed}$ , the

displacements of the DoF located inside and at the interface of "gb", the deformation of "gb" is obtained by using the static relationship:

$$\begin{bmatrix} \mathbf{K}_{in,in} & \mathbf{K}_{in,ed} \\ \mathbf{K}_{ed,in} & \mathbf{K}_{ed,ed} \end{bmatrix} \begin{pmatrix} \mathbf{u}_{gb}^{in} \\ \mathbf{u}_{gb}^{ed} \end{pmatrix} = \begin{pmatrix} \mathbf{f}_{gb}^{in} \\ \mathbf{0} \end{pmatrix} \quad (\text{IV.4})$$

So,

$$\mathbf{u}_{gb}^{in}(\theta_{1,2}) = \mathbf{K}_{in,in}^{-1} (\mathbf{f}_{gb}^{in} - \mathbf{K}_{in,ed} \mathbf{u}_{gb}^{ed}(\theta_{1,2})) \quad (\text{IV.5})$$

For each angular position, the angular deformation at the centre of "gb" referred to as  $\theta^{gb}(\theta_{1,2})$  is retrieved. We assume that this displacement is periodic at  $2\pi/N_h$ .  $\theta^{gb}(\theta_{1,2})$  is thus formulated as a periodic function:

$$\theta^{gb}(\theta_{1,2}) = A + \sum_{p=1}^{\infty} B_p \cos\left(\frac{p2\pi\theta_{1,2}}{N_h} + \phi\right) \quad (\text{IV.6})$$

For our studied cases, as we can see later, the frequency content is dominated by the fundamental frequency leading to:

$$\theta^{gb}(\theta_{1,2}) \approx A + B \cos\left(\frac{2\pi\theta_{1,2}}{N_h} + \phi\right) \quad (\text{IV.7})$$

The curve is displayed in Fig. IV.13.

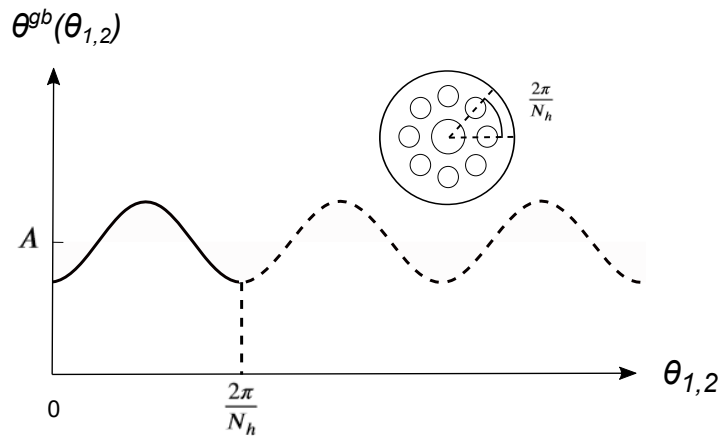


Figure IV.13: Angular deformation retrieved at the centre of "gb"

The resulting contribution along the line of action of the gear body with holes  $\delta_{gb}(\theta_{1,2})$  is defined

as:

$$\delta_{gb}(\theta_{1,2}) = R_b \theta^{gb}(\theta_{1,2}) \quad (\text{IV.8})$$

- Finally, substructures "wh" and "gb" allow the computation of the deflection  $\delta_{wh}(\theta_1)$  and  $\delta_{gb}(\theta_1)$ , respectively. The static transmission error of the gear pair with holes  $\delta_h(\theta_1)$  is computed as:

$$\delta_h(\theta_1) = \delta_{wh}(\theta_1) + \delta_{gb}(\theta_{1,2}) \quad (\text{IV.9})$$

The mesh stiffness of the gear pair with holes  $k_h(\theta_1)$  is obtained with a numerical differentiation of the transmitted load  $F$  versus  $\delta_h(\theta_1)$ .

The decomposition procedure allows the computation of the STE for a large variety of holed gear blanks. The computational time reduction comes from the fact that it is not necessary to solve the gear mesh contact over a fundamental period of the STE. The estimation of the deformation of the holed gear blank apart of the full multibody system is the key. It permits to keep the resolution of the nonlinear analysis over a mesh period. Figure IV.14 outlines the decomposition procedure, which can be extended to deal with a gear pair design with holes in both gear blanks by adding another substructure.

## 4.2 Numerical validations

The decomposition procedure is applied on three different test cases in order to show the large variety of gears that can be analyzed. The STE and mesh stiffness fluctuations are validated by comparing results with those obtained using the fully finite element simulation described in section 3. The gear characteristics of the different test cases are presented in Table IV.5. The first corresponds to a reverse gear pair with the same number of holes in the driving and driven wheels. The second corresponds to a gear pair with holes only in the driven wheel. The third corresponds to a reducer gear pair with holes only in the driven wheel. Designs of the different test cases are shown in Fig. IV.15. Gear

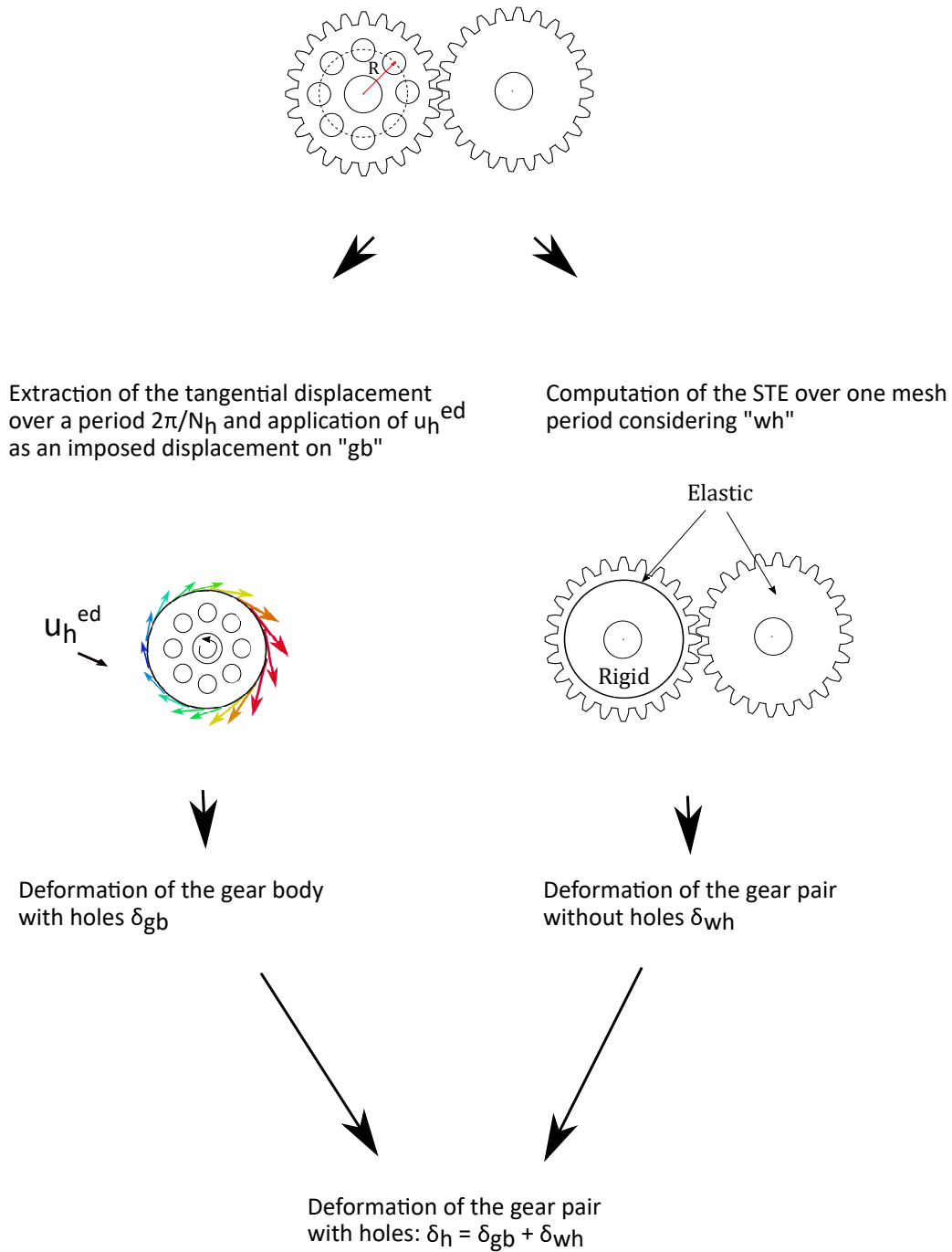


Figure IV.14: Flow chart of the decomposition procedure

pairs have also intentional removal of material along the tooth profile corresponding to a linear tip relief with length  $L = 1.75$  mm and amount  $A_m = 5\mu\text{m}$ . This micro-geometric tooth modification is introduced to minimize the STE for an output torque  $T = 115$  N m for the reverse gear pairs and  $T = 160$  N m for the reducer gear pair.

Table IV.5: Gear characteristics of the different test cases

Name	Designation	Case 1		Case 2		Case 3		Unit
-	-	Gear 1	Gear 2	Gear 1	Gear 2	Gear 1	Gear 2	-
Module	$m$	2		2		2		mm
Number of teeth	$Z$	50	50	50	50	29	85	-
Pressure angle	$\alpha$	20		20		20		deg
Base radius	$R_b$	46.984	46.984	46.984	46.984	27.251	79.874	mm
Profile shift coefficient	$x$	0	0	0	0	0	0	-
Addendum	$h_a$	2	2	2	2	2	2	mm
Dedendum	$h_d$	2.5	2.5	2.5	2.5	2.5	2.5	mm
Face width	$b_f$	20	20	20	20	20	20	mm
Center distance	$a$	100.5		100.5		118.5		mm
Tip relief modification								
Length	$L$	1.75	1.75	1.75	1.75	1.75	1.75	mm
Amount	$A_m$	5	5	5	5	5	5	$\mu\text{m}$
Lightweighting								
Number of holes	$N_h$	8	8	-	10	-	6	-
Radius of holes	$r_h$	10	10	-	7.5	-	17.5	mm

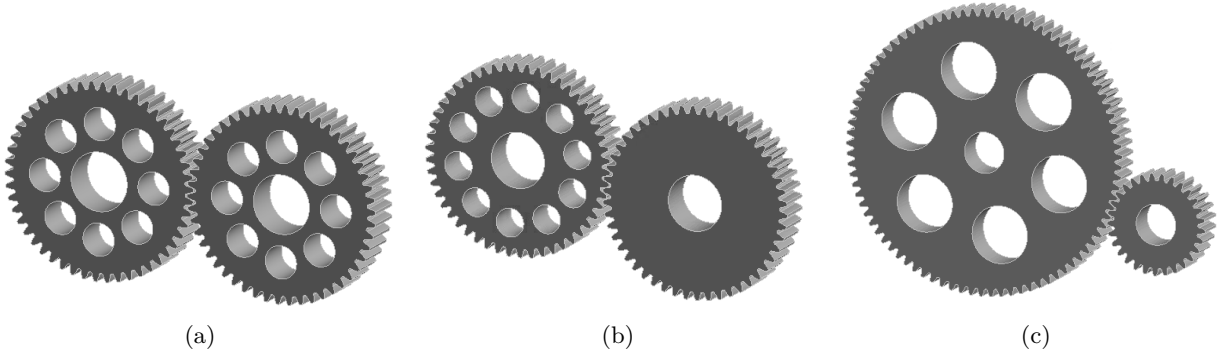


Figure IV.15: Test case 1: (a) reverse gear pair with 8 holes on driving and driven gears. Test case 2: (b) reverse gear pair with 10 holes closer to the teeth on the driven gear only. Test case 3: (c) reducer gear pair with 6 holes.

Figures IV.16, IV.17 and IV.18 displays the time evolutions and the amplitude spectra of STE and mesh stiffness for the three test cases. The harmonic orders  $H_n$  are identified with respect to the output frequency. Amplitude spectra of STE and mesh stiffness show components at the mesh frequency  $H_{Z_2}$  and its harmonics  $H_{kZ_2}$ . They also show component at harmonic  $H_{N_h}$  induced by holes designed in the driven wheel. For the reverse gear corresponding to the test case with holes in the driving gear, no

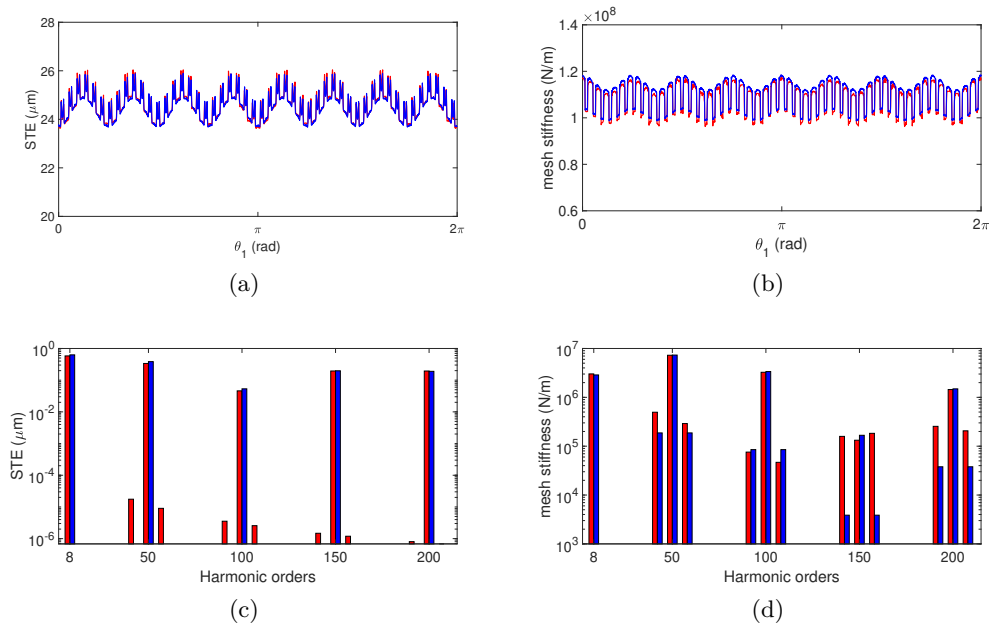


Figure IV.16: Test case 1: time evolution of the STE (a) and the mesh stiffness (b) for an output torque  $T = 115$  N m. Amplitude spectrum of STE fluctuation (c) and mesh stiffness fluctuation (d). —decomposition method, —fully flexible multibody method

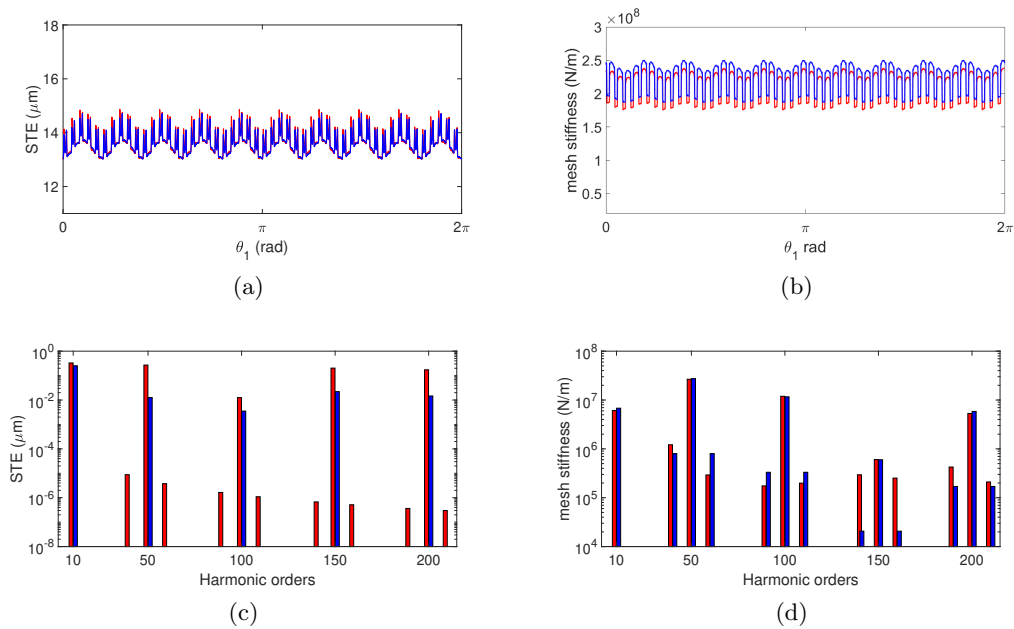


Figure IV.17: Test case 2: time evolution of the STE (a) and the mesh stiffness (b) for an output torque  $T = 115$  N m. Amplitude spectrum of STE fluctuation (c) and mesh stiffness fluctuation (d). —decomposition method, —fully flexible multibody method

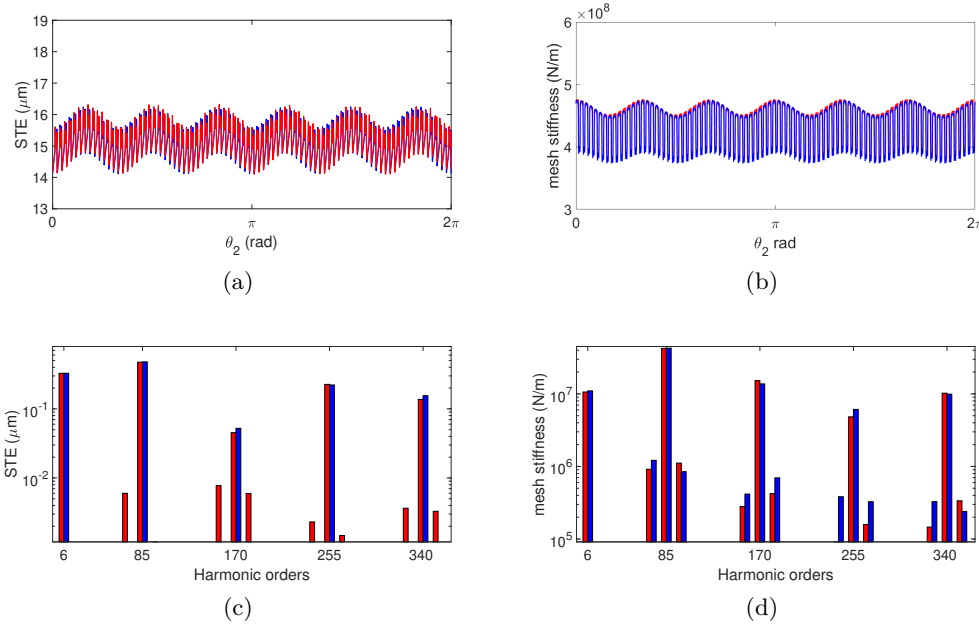


Figure IV.18: Test case 3: time evolution of the STE (a) and the mesh stiffness (b) for an output torque  $T = 115$  N m. Amplitude spectrum of STE fluctuation (c) and mesh stiffness fluctuation (d). —decomposition method, —fully flexible multibody method

additional component is observed because the number of holes is the same as those of the driven wheel.

Amplitudes of components are identical for the fully elastic multibody method and the decomposition method.

Spectra also show sidebands around harmonics of the mesh frequency,  $H_{kZ_2 \pm 1N_h}$ , for the fully elastic multibody simulation because the number of holes  $N_h$  is not a submultiple of the number of teeth  $Z_2$ , but their amplitudes are negligible compared to those of  $H_{N_h}$  and  $H_{kZ_2}$ . These sidebands are not observed for the STE spectra computed with the decomposition method. Nevertheless, they arise from the mesh stiffness spectra because this one is computed from a numerical differentiation of the transmitted load  $F$  relative to STE.

Finally, Fig. IV.16, IV.17 and IV.18 confirm that the results obtained with the decomposition method are similar to those obtained with the fully flexible multibody approach. Shapes of time evolutions, mean and root mean square values and peak to peak amplitude are very close as reported in Table IV.6.

Table IV.6: STE and mesh stiffness comparisons between the fully flexible multibody method and the decomposition method

Test case 1	Fully FE-based method	Decomposition method	Error (%)	Unit
STE mean value	24.587	24.534	0.2	$\mu\text{m}$
STE rms value	0.572	0.523	8.5	$\mu\text{m}$
STE peak-to-peak amplitude	2.408	2.216	8	$\mu\text{m}$
mesh stiffness mean value	1.088e8	1.103e8	1.4	N/m
mesh stiffness rms value	6.358e6	6.356e6	0.03	N/m
mesh stiffness peak-to-peak amplitude	2.101e7	1.984e7	5.5	N/m
Test case 2	Fully FE-based method	Decomposition method	Error (%)	Unit
STE mean value	13.651	13.587	0.5	$\mu\text{m}$
STE rms value	0.418	0.365	12	$\mu\text{m}$
STE peak-to-peak amplitude	1.843	1.688	8.4	$\mu\text{m}$
mesh stiffness mean value	2.130e8	2.239e8	5	N/m
mesh stiffness rms value	2.210e7	2.263e7	2.4	N/m
mesh stiffness peak-to-peak amplitude	6.367e7	6.394e7	0.4	N/m
Test case 3	Fully FE-based method	Decomposition method	Error (%)	Unit
STE mean value	15.103	15.093	0.1	$\mu\text{m}$
STE rms value	10.468	0.466	0.4	$\mu\text{m}$
STE peak-to-peak amplitude	2.222	2.129	4.4	$\mu\text{m}$
mesh stiffness mean value	4.347e8	4.325e8	0.5	N/m
mesh stiffness rms value	3.456e7	4.345e7	1.5	N/m
mesh stiffness peak-to-peak amplitude	1.017e8	1.018e8	0.1	N/m

**Time cost reduction:** Comparisons of STE and mesh stiffness fluctuations for the different test cases prove the accuracy of the decomposition method. Besides, high computational resources are required to compute the STE and mesh stiffness fluctuations with a fully flexible multibody method. Indeed, the method requires a fine mesh for all the gear teeth and 40 computation points over a mesh period, which means that  $40 \times Z_2$  final computation points are used to describe precisely the STE. On the other hand, for the decomposition method, only teeth covering the angle  $2\pi/N_h$  need a fine mesh and 16 computation points are retained to reconstruct the trigonometric angular deformation of the substructure "gb". Moreover, 40 computation points are added to the latter for the computation of the STE of the substructure "wh". As a consequence, with the fully multibody method, the elapsed

computing time is 15 hours for the reverse gear pair and 40 hours for the reducer. Whereas, for the decomposition method, 30 minutes (30 times faster) are needed for the reverse gear pair and 40 minutes (60 times faster) for the reducer.

## 5 A parametric study of the effect of number and radial position of holes in gear blanks

The time cost reduction associated with the decomposition procedure allows parametric analysis. In the following section, the objective is to analyze the influence of number and radial position of holes on the static transmission error and mesh stiffness fluctuations.

### 5.1 Problem description

A standard gear without holes is considered as a reference test case. It consists of a spur gear with characteristics  $Z_1 = Z_2 = 50$ ,  $m = 2$  mm,  $\alpha = 20^\circ$ ,  $b_f = 20$  mm and  $a = 100.5$  mm. A tip relief modification with amount  $A_m = 5\mu\text{m}$  and length  $L = 1.75$  mm is introduced in the tooth profile to smooth the gear meshing. It leads to a minimization of the STE fluctuation for an operating output torque  $T_{opt} = 115$  N m. Fig. IV.21 shows that the corresponding peak-to-peak amplitude is  $STE_{pp} = 1\mu\text{m}$ . Fig. IV.20 shows that the peak-to-peak amplitude is larger for a lower output torque ( $STE_{pp} = 2\mu\text{m}$  for  $T_{low} = 20$  N m). Then, the holed configurations are created from the standard gear by designing holes in the driven gear body to reduce the gear mass by 25% as presented in the Fig IV.19. For instance, a configuration with  $N_h$  eight holes at a radial position  $R = 34$  mm from the centre of the gear is labelled 8R34. A holed gear blank is introduced only for the driven gear to reduce the number of suitable configurations. The size of holes is defined to maintain a constant mass for all designed gear pairs. The radial position and the number of holes are chosen to preserve the structural integrity of the gear pair. The selected gears are then labelled by (✓) and notified in Table IV.7.

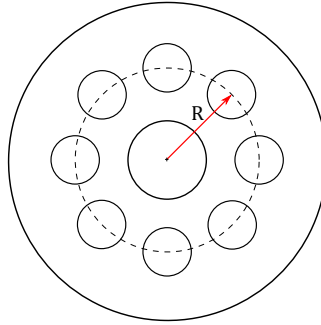


Figure IV.19: Schematic representation of the holed configuration

Table IV.7: Gear pairs with holes retained according to the number of holes  $N_h$  and their radial position  $R$ 

$R$ (mm) \ $N_h$	6	8	10
27	✗	✓	✗
30	✓	✓	✗
34	✗	✓	✓

## 5.2 Effect of number and radial position of holes

The decomposition procedure is applied on the previous configurations for a low output torque  $T_{low} = 20$  N m and an optimal output torque  $T_{opt} = 115$  N m established for the standard gear pair.

As expected and compared with the standard gear pair, Fig. IV.20 and Fig. IV.21 show that STE and mesh stiffness fluctuations present an additional low frequency component  $H_{N_h}$  for all the other configurations. The amplitude of this component  $H_{N_h}$  is related to the number of holes  $N_h$ , their radial position  $R$  and the output torque value considered.

The effect of the radial position of holes is illustrated by the cases "8R34", "8R30" and "8R27". Indeed, Fig. IV.20 and Fig. IV.21 show that the amplitude of the component  $H_{N_h}$  is larger when the radius  $R$  is increased, which means when the holes are close to the tooth root radius.

The effect of the number of holes is illustrated by the pair cases ("10R34", "8R34") and ("8R30", "6R30"). Figures IV.20 and IV.21 show for a given radial position of holes that increasing the number of holes reduces the STE fluctuations.

The effect of the output torque is also identified. STE fluctuations of the standard gear pair are governed by the micro-geometry modification for a low output torque  $T_{low} = 20 \text{ N m}$ . Whereas STE fluctuations are governed by the gear deformation for the optimal output torque  $T_{opt} = 115 \text{ N m}$ . The amplitude of the low frequency fluctuations associated with the  $H_{N_h}$  component is thus increased.

The critical modes for which the strain energy at the gear mesh is the highest are governed by the mean value of the mesh stiffness. Designing holes in the gear blanks decreases the mean value and the fluctuations of the mesh stiffness (Fig. IV.20 and Fig. IV.21). As a consequence, the critical frequencies are reordered. The fluctuations of the mesh stiffness are modified compared to the standard gear pair. These changes have thus important influence on the parametric resonances observed for the dynamic response [131].

## 6 Conclusion

This chapter applies the proposed methodology detailed the previous chapter on several gear design. First of all, gear pairs with micro-geometry modification is used. Examples of tip relief and crowning are well supported. Then, the addition of flexible shafts and thin rim is treated. The proposed methodology is able to handle the effect of the misalignment induced by flexible shafts on the STE and the contact pressure distribution. Indeed, the shape and the peak-to-peak amplitude of the STE is modified.

We showed that the proposed methodology can also compute the STE of a complete gearbox including flexible shafts, bearings and the housing. The simulation is speed up with the use of Guyan condensation for shafts, bearing and the housing. A comparison has been done for long and short shafts and a standard gear pair. Both gearboxes modify the shape of the STE and increase the peak-to-peak amplitude. This increase is more significant for the gearbox with long shafts.

In the second part of the chapter, a particular attention has been paid to holed gear blanks. The

effect of holed gear blanks on the STE and the mesh stiffness is illustrated. Indeed, the frequency content is enriched with a low frequency component corresponding to the number of holes and with sidebands around mesh frequencies. The computation of such systems is demanding since the presence of holes extend the periodicity of the system. To reduce the computation time, we derived an original 2D decomposition method based on the substructuring of the holed gear bodies and the remainder of the gear pair. The approach bypasses the computation of the full nonlinear multibody system while considering the contribution of holes. The efficiency of our approach was assessed by considering the fully finite element approach as a reference for the computation of static transmission error and the mesh stiffness fluctuations. The decomposition procedure reduces considerably the elapsed computing time, which enables fast parametric studies of gears with holes. Thanks to a parametric study, this work features the effects of holed gear blanks on the static transmission error and the mesh stiffness fluctuations. It shows that different effects appear according to the radial position and number of holes and the output torque considered. An additional low frequency component corresponding to the existence of holes is observed. Then, the amplitude of the component  $H_{N_h}$  is increased with the operating output torque and with the radial position  $R$ . On the other hand, increasing the number of holes for a given radial position  $R$ , reduce the STE fluctuations. The mean values of the different mesh stiffness are reduced compared with the standard gear pair and the fluctuations are significantly modified. Holes in gear blanks can be thus a design strategy to reduce the mesh stiffness mean value and fluctuations. The observed effects cannot be set apart because they have important consequences on the parametric and dynamic responses.

This chapter demonstrates the potential of the proposed methodology to compute the static transmission error and the mesh stiffness of any type of gear system. These physical quantities are essential to simulate the dynamic response. So, the objective of the next chapter is to use the fully flexible multibody simulations for the simulation of gear dynamics. Two different strategies are carried out. The first strategy relies on the STE and mesh stiffness excitation. The second strategy employs model order reduction techniques for solving the fully multibody systems in operating dynamic conditions.

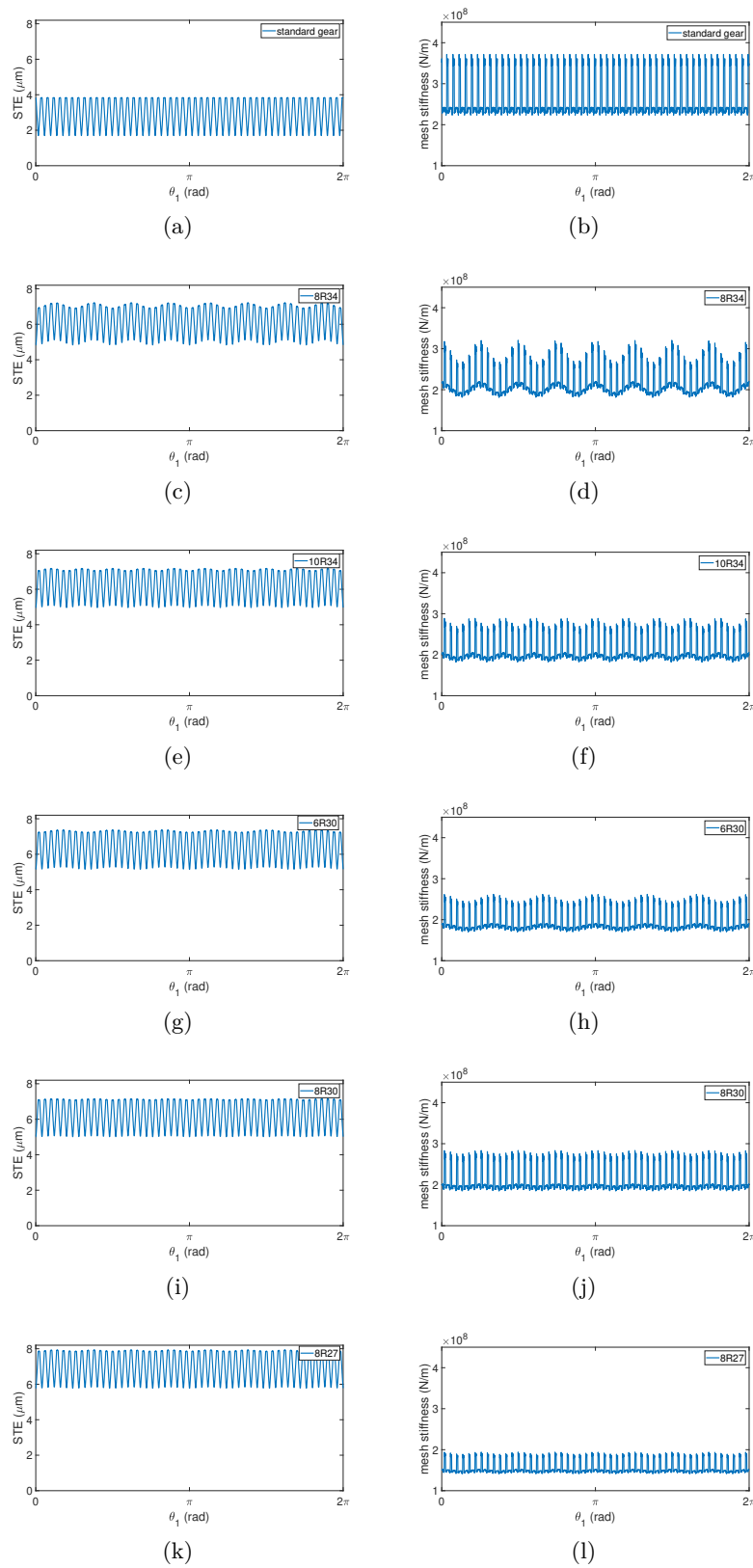


Figure IV.20: Time evolution of the STE and the mesh stiffness for an output torque  $T = 20 \text{ N m}$ : (a,b) standard gear, (c,d) case 8R34, (e,f) case 10R34, (g,h) case 6R30, (i,j) case 8R30, (k,l) case 8R27.

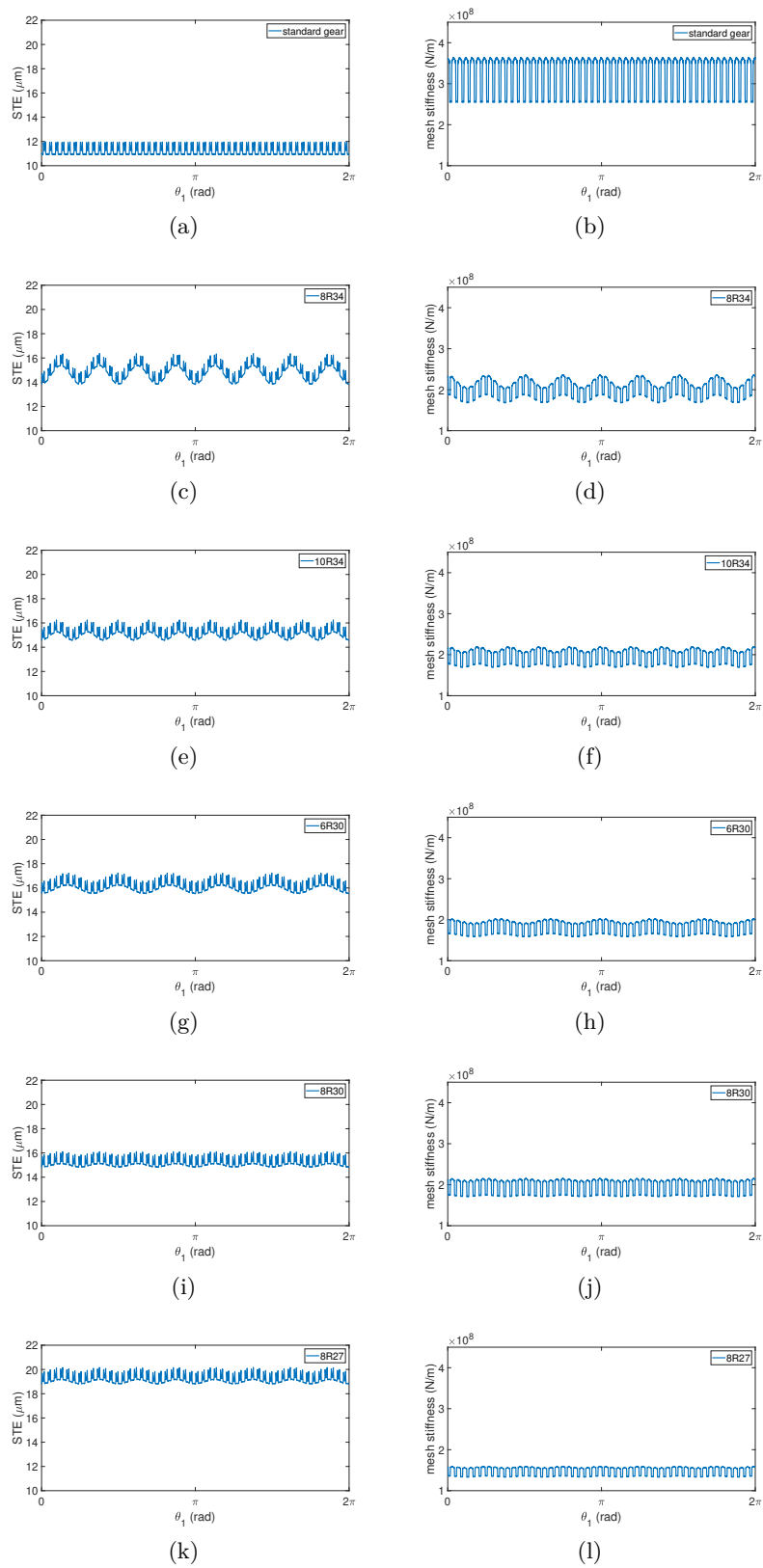


Figure IV.21: Time evolution of the STE and the mesh stiffness for an output torque  $T = 115 \text{ N m}$ : (a,b) standard gear, (c,d) case 8R34, (e,f) case 10R34, (g,h) case 6R30, (i,j) case 8R30, (k,l) case 8R27.



# V

## Prediction of the dynamic gear behaviour

---

### Introduction

---

This chapter proposes firstly an introduction to the concept of model order reduction. The main approaches used in structural dynamics are presented. The reduced order models obtained enable the solve of large finite element models. Hereafter, we propose to use a condensed model for the flexible shafts, the bearings and the housing, and parametric excitations are considered to couple the input/output gears. This reduced model is retained to solve the stationary response of a complete gearbox. Besides, the Harmonic Balance Method (HBM) is employed. Additionally, for a fully FE-based contact approach, the number of degrees of freedom does not allow to use condensed model of the gear pair. Thus, a flexible multibody framework coupled with model order reduction is proposed. The model of a gear pair is treated and the method is applied to the case of transient dynamic response. The reduced order model is based on the Proper Orthogonal Decomposition (POD) or

Krylov subspace.

---

## Contents

1	Model order reduction . . . . .	96
1.1	Introduction . . . . .	96
1.2	Galerkin projection based method . . . . .	98
1.3	Review of model order reduction techniques . . . . .	101
1.4	Choice for the gear reduced order models . . . . .	112
2	Stationary dynamic response . . . . .	113
2.1	Computation procedure . . . . .	113
2.2	Numerical strategy in the frequency domain . . . . .	118
2.3	Results and discussion . . . . .	120
3	Transient dynamic response . . . . .	123
3.1	Equation of motion of flexible multibody dynamics . . . . .	124
3.2	Proposed reduced order models . . . . .	131
3.3	Integration of the equations of motions for nonsmooth mechanics . . . . .	143
3.4	Proposed strategy for the contact . . . . .	147
4	Conclusion . . . . .	151

---

## 1 Model order reduction

### 1.1 Introduction

The growth in complexity of industrial systems, the advancement of engineering tools and the move to zero physical prototyping promoted the increase in the size of models and the demands for higher processing power to solve these derived models. In order to solve these models in a reasonable, in particular during design iterations, reduced order modelling can be an option while maintaining the physical significance that the engineer is trying to predict.

In structural dynamics, the accuracy of the results often comes with the convergence of the mesh, thus with an increasing model size. The challenge consists in building a reduced order model that

allows real-time evaluation while retaining the accuracy of the prediction. Here, we focus on model order reduction of contact problems with emphasis on flexible multibody gear dynamics.

In this manuscript, reducing a model will first consist in finding the solution of the dynamical system in a finite dimensional space by decomposing the reconstructed solution as a linear time and space combination of elements of the reduced basis. Mathematically, the displacement field is expressed as follows:

$$\mathbf{x}(t) \approx \mathbf{\Psi}\mathbf{q}(t)$$

where  $\mathbf{\Psi}$  is a matrix representing the reduced basis and  $\mathbf{q}(t)$  are the new unknowns of the problem.  $\mathbf{\Psi}$  are also the so-called spatial modes and  $\mathbf{q}(t)$  are the modal amplitudes corresponding to the contributions of each mode of  $\mathbf{\Psi}$  over time. The equations of motion are then projected in a subspace in order to reduce the size of the system.

The literature [8, 14, 48, 106] provides several formal techniques to carry out model order reduction for linear systems with many different goals in mind. By fully exploring the capabilities of the different methodologies and evaluating their fundamental concepts one can apply these methods effectively. However, several of the models and systems dealt with in industrial application carry a number of nonlinear behavior. For instance in this manuscript, we deal with a nonsmooth gear dynamics. So, nonlinearity of contact must be considered. The gear pair is connected by the contact between the gear

teeth with potential losses. The application of model order reduction for these nonsmooth systems is truly complex. Besides, small investigations are proposed in the literature [15, 20].

Determining a reduced basis  $\Psi$  with the least possible loss of information is at the core of the methods. The reduced basis can be build from different manner. Indeed, the reduced basis can be constructed from existing system data [60, 143] (for instance some previous simulations). The generation of the reduced basis can also be at the same time as the solution itself. In all possibilities, one must keep a critical regard on the error committed by the choice of such a subspace with respect to the solution of a complete system.

Hereafter, we will start by explaining the general framework of the Galerkin projection based method. Then, a review is proposed to describe in detail the different model order reduction techniques. Finally, two strategies will be proposed to reduced the system while taking into account the contact behaviour.

## 1.2 Galerkin projection based method

In the following, we start the deveopment from already a discretized finite element model. We remind the finite element equation of motion:

$$\mathbf{M}\ddot{\mathbf{x}} + \mathbf{C}\dot{\mathbf{x}} + \mathbf{K}\mathbf{x} + \mathbf{F}_{nl}(\mathbf{x}) = \mathbf{F}_{ext} \quad (\text{V.1})$$

The choice of the damping matrix  $\mathbf{C}$  will be explained later in this chapter. The Galerkin or Petrov-Galerkin projection based method consists in searching an approximation of the solution of the problem

belonging to the space  $\mathbf{W}_0$  III.2 of dimension  $n$  in a subspace  $\mathbf{W}_r$  of dimension  $r$  such that  $r \ll n$ . This method assumes a weak formulation of the mechanical problem as derived in 1.1. The main advantage of a Galerkin or Petrov-Galerkin method is to make the residual orthogonal to the approximation subspace  $\mathbf{W}_r$ . The approximation of the solution in the reduced subspace reads :

$$\mathbf{x}(t) \approx \Psi \mathbf{q}(t) \quad (\text{V.2})$$

this expression is used in the residual form of the equation of motion:

$$\mathbf{R}(\Psi \ddot{\mathbf{q}}(t), \Psi \dot{\mathbf{q}}(t), \Psi \mathbf{q}(t)) = \mathbf{M} \Psi \ddot{\mathbf{q}}(t) + \mathbf{C} \Psi \dot{\mathbf{q}}(t) + \mathbf{K} \Psi \mathbf{q}(t) + \mathbf{F}_{nl}(\Psi \mathbf{q}(t)) - \mathbf{F}_{ext}(t) \quad (\text{V.3})$$

Then, the left-multiplication by the transpose matrix of  $\Lambda$  which has the same dimension of  $\Psi$  yields:

$$\Lambda^T \mathbf{M} \Psi \ddot{\mathbf{q}}(t) + \Lambda^T \mathbf{C} \Psi \dot{\mathbf{q}}(t) + \Lambda^T \mathbf{K} \Psi \mathbf{q}(t) + \Lambda^T \mathbf{F}_{nl}(\Psi \mathbf{q}(t)) - \Lambda^T \mathbf{F}_{ext}(t) = \mathbf{0} \quad (\text{V.4})$$

if  $\Lambda = \Psi$  the projection is called Galerkin projection. if  $\Lambda \neq \Psi$  the projection is called Petrov-Galerkin projection. For some cases, Petrov Galerkin projection is a better choice. For instance if you deal with fluid dynamics [23] and/or unsymmetric matrices [47]. In the following, we consider the Galerkin projection with  $\Lambda = \Psi$ .

$$\Psi^T \mathbf{M} \Psi \ddot{\mathbf{q}}(t) + \Psi^T \mathbf{C} \Psi \dot{\mathbf{q}}(t) + \Psi^T \mathbf{K} \Psi \mathbf{q}(t) + \Psi^T \mathbf{F}_{nl}(\Psi \mathbf{q}(t)) - \Psi^T \mathbf{F}_{ext}(t) = \mathbf{0} \quad (\text{V.5})$$

The reduced matrices and the reduced load vector are therefore:

$$\mathbf{M}_r = \Psi^T \mathbf{M} \Psi \quad \mathbf{C}_r = \Psi^T \mathbf{C} \Psi \quad \mathbf{K}_r = \Psi^T \mathbf{K} \Psi \quad \mathbf{f}_{nl}(\mathbf{q}(t)) = \Psi^T \mathbf{F}_{nl}(\Psi \mathbf{q}(t)) \quad \mathbf{f}_r = \Psi^T \mathbf{F}_{ext} \quad (\text{V.6})$$

These matrices are dimensionally much smaller than the finite element matrices expressed in the physical space. The reduced equation of motion are thus:

$$\mathbf{M}_r \ddot{\mathbf{q}}(t) + \mathbf{C}_r \dot{\mathbf{q}}(t) + \mathbf{K}_r \mathbf{q}(t) + \mathbf{f}_{nl}(\mathbf{q}(t)) = \mathbf{f}_r \quad (\text{V.7})$$

However, for the contact problem a particular attention must be given to the term:

$$\mathbf{f}_{nl}(\mathbf{q}(t)) = \Psi^T \mathbf{F}_{nl}(\Psi \mathbf{q}(t)) \quad (\text{V.8})$$

Indeed, the contact detection (see Fig. V.1) and resolution has to be performed in the physical space using Signorini conditions (III.18). Then, the contact forces are projected in the reduced space for solving the dynamics. This process has to be performed at each time step. Further details will be done in the section 3.

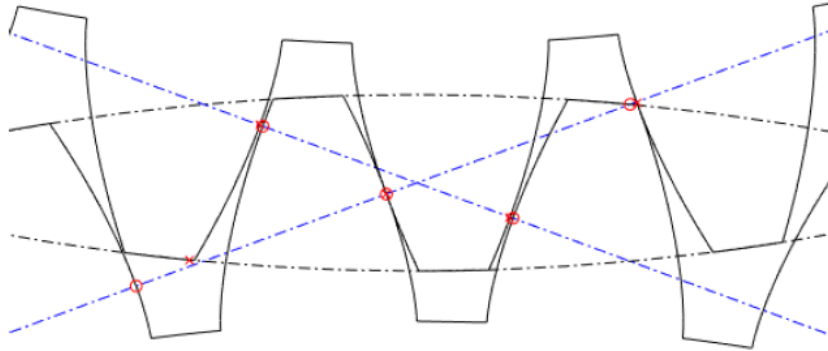


Figure V.1: Description of the tooth contact point.

The Galerkin based projection method is used in the following developments to apply model order reduction techniques on the equation of motion. Thus, the next section review the main model order reduction techniques especially with emphasis on contact problems.

### 1.3 Review of model order reduction techniques

This section proposes a detailed description of model order reduction techniques generally used in structural dynamics with a particular attention on the application for contact problems. The objectives are thus to present the theory of the reduction methods and the advantages of such methods in order to propose a reduction method strategy for the gear contact dynamic. The model order reduction techniques considered in this manuscript belong to the class of Galerkin projection based methods.

#### 1.3.1 Modal superposition method

In all the following methods and in linear vibration field, structural modes are fundamental to analyze the general behavior of structures because they provide a basis for the dynamical system and the most general motion of the system is a superposition of its normal modes. In that case, the reduction is performed according to this essential dynamical property as developed in the literature [14, 90]. The subspace considered is spanned by the dominant normal modes of the flexible body. The normal modes (mode shapes and associated frequencies) are obtained by solving an eigenvalue problem. The precision of the basis is directly related to the number of mode shapes retained. Hereafter, we derive the equation while neglecting the gyroscopic and the centrifugal effects. This is the mode shapes of uncoupled structure. For instance, in gear the input/output gears are not coupled. Also, the mode shapes are assumed to be isolated in frequency with respect to the resonances and the damping of the system is low.

In the frequency domain, the equation of motion III.22 as the linear form reads:

$$(\mathbf{K} + i\omega_j\mathbf{C} - \omega_j^2\mathbf{M})\phi_j = 0 \quad (\text{V.9})$$

where  $\omega_j$  the eigenvalue and  $\phi_j$  the associated eigenvectors called mode shape. Generally, the damping term is ignored and the eigenvalue problem becomes:

$$(\mathbf{K} - \omega_j^2\mathbf{M})\phi_j = 0 \quad (\text{V.10})$$

The equation V.10 stands for modal analysis of the structure. Solving the equation V.10 provides orthogonality of the mode shapes  $\phi_j$ . Usually, mode shapes are normalized with respect to the mass in order to facilitate the computation of the transfer function. Generally, the model of viscous damping is retained. So, the reduced basis  $\Psi$  is chosen as the  $r$  first truncated mode shapes. Considering a viscous damping and the mass normalized and orthogonal mode shapes provide the following properties:

$$\mathbf{M}_r = \Psi^T \mathbf{M} \Psi = \mathbf{I}_{r \times r}$$

$$\mathbf{C}_r = \Psi^T \mathbf{C} \Psi = \text{diag}(2\xi_j\omega_j) \text{ for } j \in [1 \dots r]$$

$$\mathbf{K}_r = \Psi^T \mathbf{K}_{av} \Psi = \text{diag}(\omega_j^2) \text{ for } j \in [1 \dots r]$$

$$\mathbf{f}_r = \Psi^T \mathbf{F}_{ext}$$

with  $\xi_j$  the modal damping. The transfer function as a serie of modal contributions is:

$$H_j(\omega_i) = \frac{\phi_j \phi_j^T}{\omega_i^2 + 2\xi_j\omega_j\omega_i + \omega_j^2} \quad (\text{V.11})$$

This transfer function can be reduced by considering only the  $r$  mode shapes in the interested range of frequency for the analysis. However, the high frequency mode shapes have also a contribution at low frequency. The transfer function becomes:

$$H(\omega) \approx \sum_{j=1}^r \frac{\phi_j \phi_j^T}{\omega^2 + 2\xi_j \omega_j \omega + \omega_j^2} + \sum_{j=r+1}^n \frac{\phi_j \phi_j^T}{\omega_j^2} \quad (\text{V.12})$$

$n$  is the number of degrees-of-freedom of the considered problem. The second term of the transfer function doesn't depend on frequency, this is the static correction or also called the residual flexibility and this term is the contribution at low frequency of high frequency modes. A good approximation is to enhance the truncated mode shapes by this term. The static correction can be determined in space as follows:

$$H(0) = \mathbf{K}^{-1} \mathbf{F}_{ext} \approx \sum_{j=1}^r \frac{\phi_j \phi_j^T}{\omega_j^2} + \sum_{j=r+1}^n \frac{\phi_j \phi_j^T}{\omega_j^2}$$

then,

$$\sum_{j=r+1}^n \frac{\phi_j \phi_j^T}{\omega_j^2} \approx \mathbf{K}^{-1} \mathbf{F}_{ext} - \sum_{j=1}^r \frac{\phi_j \phi_j^T}{\omega_j^2}$$

Consequently, a better choice of the reduced basis is to enhance the  $r$  first truncated mode shapes with the static correction. The reduced basis becomes:

$$\Psi = \left[ \phi_1 \quad \dots \quad \phi_r \quad \mathbf{K}^{-1} \mathbf{F}_{ext} - \sum_{j=1}^r \frac{\phi_j \phi_j^T}{\omega_j^2} \right] \quad (\text{V.13})$$

This approach is well adapted for linear system but it becomes more complex to represent properly nonlinearities. Muravyov *et al* [100] proposed the Stiffness Evaluation Procedure (STEP) for dealing with geometric nonlinearities. The nonlinear term is approximated by  $\mathbf{F}_{nl}(\mathbf{q})_j = \sum_j \tilde{k}_{i,j}^1 \mathbf{q}_j + \sum_{i,j,k} \tilde{k}_{i,j,k}^2 \mathbf{q}_j \mathbf{q}_k +$

$\sum_{i,j,k,l} \tilde{k}_{i,j,k,l}^3 \mathbf{q}_j \mathbf{q}_k \mathbf{q}_l$  using the modal superposition method. A serie of static analyses is then used to identify the coefficients  $\tilde{k}_{i,j}^1$ ,  $\tilde{k}_{i,j,k}^2$  and  $\tilde{k}_{i,j,k,l}^3$ . However, for contact problems, the deformation at the contact area induce local deformation which represent high frequency modes. Thus, the high number of mode shapes required to represent this local deformation prevent the application of the modal superposition method as investigated in [155].

### 1.3.2 Component mode synthesis method (CMS)

Component mode synthesis (CMS) methods are substructuring techniques which involve partitioning of the entire structure into several substructures. A central piece of CMS is to derive the behavior of the entire structure from its components. There are several variations of cms, we can quote the methods of Rubin, Craig-Chang, Craig-Martinez [36, 37, 113]. In this section, the CMS method refers to the Craig Bampton [36] formulation which is the most employed approach in the literature due to its implementation convenience and robustness. This approach can be seen as an extension of the Guyan condensation [56].

Following the Craig and Bampton CMS strategy requires:

- the static boundary modes represented by the Guyan modes. They can be obtained by imposing successively a unit displacement to each boundary degree of freedom.
- a reduced set of fixed interface modes (clamped modes).

So, the idea of the CMS reduction is to consider two sets of degrees-of-freedom (DOF), one for

master DOF and another for complementary DOF. Master DOF represents DOF for which loads and constraints are applied and complementary DOF are all the other DOF of the considered system. The dynamic response of the system is then approximated within a subspace spanned by a combination of Guyan modes and fixed interface modes. The partition of the stiffness matrix is obtained by splitting the matrix into four blocs as:

$$\begin{bmatrix} \mathbf{K}_{AA} & \mathbf{K}_{AC} \\ \mathbf{K}_{CA} & \mathbf{K}_{CC} \end{bmatrix} \quad (\text{V.14})$$

Where the indexes A and C states for the active (master) and complementary (slave) degree of freedom, respectively. Guyan modes  $\Phi_s$  represent the static contribution of the system and they can be derived using the equation III.23:

$$\Phi_s = \begin{bmatrix} \mathbf{I} \\ -\mathbf{K}_{CC}^{-1} \mathbf{K}_{CM} \end{bmatrix} \quad (\text{V.15})$$

The fixed interface modes  $\Phi_d$  represent the dynamic behaviour of the structure. They are computed by ensuring a fixed displacement field at the master DOF locations and then performing a modal analysis of the complete system. The dynamical part of the basis can be collected in the following matrix:

$$\Phi_d = \begin{bmatrix} \mathbf{0} \\ \Phi_{FIM} \end{bmatrix} \quad (\text{V.16})$$

$\Phi_{FIM}$  are the contribution of the fixed interface modes at the slave DOF location. The combination of the Guyan modes  $\Phi_s$  and the fixed interface modes  $\Phi_d$  leads finally to the CMS reduction matrix

$\Psi$  of the form:

$$\Psi = \begin{bmatrix} \mathbf{I} & \mathbf{0} \\ \mathbf{K}_{CC}^{-1}\mathbf{K}_{CM} & \Phi_{FIM} \end{bmatrix} = [\Phi_s \quad \Phi_d] \quad (\text{V.17})$$

The substructure is obtained by projecting the finite element matrices on  $\Psi$ . In a finite element environment, they constitute a "superelement" which can be assembled with the remainder of the structure. The CMS approach is widely deployed in solid mechanics, it's a general and modular method and the CMS is simple to execute thanks to the choice of "physical coordinates". This model order reduction technique has been used in the literature for solving the gear contact dynamics [138, 120].

However, the applications were on coarse meshes in the contact area. The studies were not accounting for micro-geometry modifications and hertzian-like deformation. When dealing with a fine mesh in the contact zone, the method become inefficient as discussed in the section III.4.3 for Guyan modes.

### 1.3.3 Krylov subspace

The objective of Krylov subspace also called "Moment Matching Method" [8, 14, 48, 106] is to provide a subspace allowing the approximation of the system's transfer function which describes the input-output relationship. Generally, Krylov subspaces are built with a state space representation of the equation of motion. However, recently [11, 12, 96], a Krylov subspace derived from the second order form of the equation of motion have been introduced. This technique is usually applied for a large scale dynamical system since the dimension of the manipulated matrices are two times smaller than the one using the state space representation. Many approaches can be followed to solve second order dynamical systems. Indeed, Interpolatory model order reduction methods like Multi-point Pade Approximation,

Krylov-based Galerkin projection and the Derivative-based Galerkin projection. A quick overview of the theoretical part are explained and applied in [10, 13, 14, 40, 65, 106].

The transfer function  $H(s)$  of a linear discretized finite element model using the second order form of the equation of motion is:

$$H(s) = (s^2\mathbf{M} + s\mathbf{C} + \mathbf{K})^{-1}\mathbf{F}_{ext} \quad (\text{V.18})$$

with  $s$  the Laplace variable. We can thus show easily that the transfer function can be expressed as a Mac-Laurin development by:

$$H(s) = \sum_{p=0}^{\infty} (-1)^p \mathcal{M}_p(s_0) (s - s_0)^p \quad (\text{V.19})$$

where  $\mathcal{M}_p(s_0)$  is called Markov moment around  $s_0$ . To approximate the transfer's function, the equation V.19 can be truncated at the order  $r$  as:

$$H(s) = \sum_{p=0}^r (-1)^p \tilde{\mathcal{M}}_p(s_0) (s - s_0)^p + o((s - s_0)^r) \quad (\text{V.20})$$

This expression respects the moment matching property :

$$\text{for } p = 1 \dots r, \quad \tilde{\mathcal{M}}_p(s_0) = \mathcal{M}_p(s_0) \quad (\text{V.21})$$

The Krylov method is based on the procedure to calculate the Markov moment matching coefficient  $\tilde{\mathcal{M}}_p(s_0)$ . In addition, the precision of the method depends on the expansion point  $s_0$  whereby the transfer function is approximated. Krylov subspace  $\mathcal{K}_r$  are presented as defined by Bai *et al.* [11, 12, 96] which is one of the latest form in the literature according to our knowledge. For an expansion point

$s_0 = 0$ , it yields:

$$\mathcal{K}_r(\mathbf{A}_1, \mathbf{A}_2, \mathbf{R}_0) = \left\{ \mathbf{R}_0, \mathbf{R}_1, \dots, \mathbf{R}_{r-1} \right\} \quad (\text{V.22})$$

$$\text{for } p \geq 2, \quad \mathbf{R}_p = \mathbf{A}_1 \mathbf{R}_{p-1} + \mathbf{A}_2 \mathbf{R}_{p-2}$$

$$\mathbf{A}_1 = -\mathbf{K}^{-1} \mathbf{C},$$

$$\mathbf{A}_2 = -\mathbf{K}^{-1} \mathbf{M},$$

$$\mathbf{R}_0 = -\mathbf{K}^{-1} \mathbf{F}_{ext}$$

$$\mathbf{R}_1 = \mathbf{A}_1 \mathbf{R}_0$$

Krylov subspace for contact problems haven't been considered in the literature. The main reason is that this model order reduction technique is derived for a good approximation of input-output system behaviour. And for contact problems, the input-output relation is modified by the fluctuation of the contact forces.

In this manuscript, in section 3, a strategy is devised and proposes to use Krylov subspaces in the context of gear contact dynamics.

### 1.3.4 Proper Orthogonal Decomposition (POD)

The proper orthogonal decomposition (POD) [107] is a method that allows to obtain an optimal reduced basis from a sample of solutions. The name of the method depends on the field of application.

In its general framework, the method can be found under the name of Karhunen-Loève decomposition [82, 95]. In the field of statistics, it is called principal component analysis [76] and in mathematics, it

also called singular value decomposition (SVD) [16].

The POD method requires a collection of data from which dominant component are extracted. To illustrate the method, we consider a set of  $N$  finite element solution in space and time known for each degree of freedom considering the equation of motion used for the gear simulation (see III.22) as:

$$\mathbf{u}(t_i) \quad \forall i \in [1...N]$$

For instance, it can be the displacement field at various points in time in a transient structural analysis.

Similarly, in fluid dynamics data can refer to the field of pressure for different velocities [111, 139].

These data are called snapshots. The objective of the POD is to find a subspace  $\mathbf{W}_r$  of dimension  $r$  included in the full finite element solution subspace such that  $r \ll n$ . For a given solution  $\mathbf{u}_i$ , we define the orthogonal projection on  $\mathbf{W}_r$  noted  $\Pi^r$  by:

$$\Pi^r \mathbf{u}_i = \sum_{j=1}^r \langle \mathbf{u}_i, \Psi_j \rangle \Psi_j \quad (\text{V.23})$$

with  $\langle, \rangle$  the scalar product. So, the problem to solve can be written as:

$$\text{Find } \Psi \in \mathbf{W}_r, \text{ Min } \frac{1}{2} \left( \sum_{i=1}^N \|\mathbf{u}_i - \Pi^r \mathbf{u}_i\|^2 \right) \quad (\text{V.24})$$

Including V.23 in V.24, the problem yields:

$$\sum_{i=1}^N \left\| \mathbf{u}_i - \sum_{j=1}^r \langle \mathbf{u}_i, \boldsymbol{\Psi}_j \rangle \boldsymbol{\Psi}_j \right\|^2 = \sum_{i=1}^N \left( \langle \mathbf{u}_i - \sum_{j=1}^r \langle \mathbf{u}_i, \boldsymbol{\Psi}_j \rangle \boldsymbol{\Psi}_j, \mathbf{u}_i - \sum_{j=1}^r \langle \mathbf{u}_i, \boldsymbol{\Psi}_j \rangle \boldsymbol{\Psi}_j \rangle \right) \quad (\text{V.25})$$

$$= \sum_{i=1}^N \|\mathbf{u}_i\|^2 - 2 \sum_{i=1}^N \sum_{j=1}^r \langle \mathbf{u}_i, \langle \mathbf{u}_i, \boldsymbol{\Psi}_j \rangle \boldsymbol{\Psi}_j \rangle + \sum_{i=1}^N \sum_{j=1}^r \langle \mathbf{u}_i, \boldsymbol{\Psi}_j \rangle^2 \quad (\text{V.26})$$

$$= \sum_{i=1}^N \|\mathbf{u}_i\|^2 - 2 \sum_{i=1}^N \sum_{j=1}^r \langle \mathbf{u}_i, \boldsymbol{\Psi}_j \rangle^2 + \sum_{i=1}^N \sum_{j=1}^r \langle \mathbf{u}_i, \boldsymbol{\Psi}_j \rangle^2 \quad (\text{V.27})$$

$$= \sum_{i=1}^N \|\mathbf{u}_i\|^2 - \sum_{i=1}^N \sum_{j=1}^r \langle \mathbf{u}_i, \boldsymbol{\Psi}_j \rangle^2. \quad (\text{V.28})$$

The equation V.24 is thus equivalent to:

$$\text{Max} \sum_{i=1}^N \sum_{j=1}^r \langle \mathbf{u}_i, \boldsymbol{\Psi}_j \rangle^2 \Leftrightarrow \text{Max} \sum_{i=1}^N \sum_{j=1}^r \boldsymbol{\Psi}_j^T \left( \sum_{i=1}^n \mathbf{u}_i \mathbf{u}_i^T \right) \boldsymbol{\Psi}_j \quad (\text{V.29})$$

Finally, the problem reads:

$$\text{Find } \boldsymbol{\Psi} \in \mathbf{W}_r \text{ that, } \text{Max} \left( \sum_{j=1}^r \boldsymbol{\Psi}_j^T (\mathbf{S}\mathbf{S}^T) \boldsymbol{\Psi}_j \right) \quad (\text{V.30})$$

where  $\mathbf{S}$  is the matrix of the collection of snapshots  $\mathbf{u}_i$ . The term  $\mathbf{S}\mathbf{S}^T$  is thus the auto-correlation (or covariance) matrix of  $\mathbf{S}$ . Quotient of Rayleigh V.30 is maximum for the eigenvector associated to the maximum eigenvalue of  $\mathbf{S}\mathbf{S}^T$ . In practice, the use of factorization techniques such as the singular value decomposition method enable the extraction of the reduced basis  $\boldsymbol{\Psi}$  from  $\mathbf{S}$  ( $n \times N$ ) or  $\mathbf{S}\mathbf{S}^T$  ( $n \times n$ ) or even  $\mathbf{S}^T\mathbf{S}$  ( $N \times N$ ). A good selection of this matrices will be discussed in the section V.3.

The proper orthogonal decomposition is a method with proven efficiency in the field of parametric and nonlinear systems reduction [43, 49, 87, 92]. Actually, the method is applied as linear form with the

Galerkin procedure but the parametric and nonlinear properties of the field of interest are taken into account in the snapshots. So, for parametric or nonlinear analyses, it requires substantial numerical effort, via the complete simulation of the system, to obtain the snapshots. For best results, fine time sampling is required, which can lead to very large matrices.

In the section 3, a strategy for using the POD for gear contact dynamics is proposed.

### 1.3.5 Proper Generalized Decomposition (PGD)

The proper orthogonal decomposition (POD) is a reduction technique developed firstly by Ladevèze under the name of LARge Time INcrement (LATIN) method in the 1980s [89]. The method was a part of non-incremental and non-linear solver. The name of proper generalized decomposition appeared later with the work of Chinesta [33, 32], Ammar [6] and Nouy [104] for solving mechanical problems, fluid dynamics and stochastic problems, respectively.

The idea of the PGD consists in expressing the solution with separate variable as follows:

$$\mathbf{u}^r(\mu_1, \dots, \mu_d) \approx \sum_{j=1}^r \prod_{i=1}^d \boldsymbol{\lambda}^j(\mu_i) \quad (\text{V.31})$$

The separation variable can be in space and in time but also as parameter of the system. The core of this method relies on an algorithm that allows to enrich the solution. The enrichment process that allows to find  $\mathbf{u}^r(\mu_1, \dots, \mu_d) \approx \mathbf{u}^{r-1}(\mu_1, \dots, \mu_d) + \prod_{i=1}^d \boldsymbol{\lambda}^r(\mu_i)$  is based on the fixed point algorithm [33].

The PGD method is efficient for systems with nonlinearities. However, This reduction method is

truly complex to implement for industrial software because it requires algorithmic iteration at the solver level. That's the reason that this approach was not retained for our developments.

#### 1.4 Choice for the gear reduced order models

The previous section presents some model order reduction techniques. These techniques differ by the way to generate the reduced basis  $\Psi$  in a subspace  $\mathbf{W}_r$  dimensionally much smaller than  $\mathbf{W}_0$  of the complete space of the solution. Modal superposition methods, Component mode synthesis method and Krylov subspace are strategies exploiting the structural matrices obtained by finite element. In practice, the methods need the access to a finite element solver at a deep level to extract these matrices. On the contrary, proper orthogonal decomposition is independent from the  $\mathbf{M}$ ,  $\mathbf{C}$  and  $\mathbf{K}$  matrices. Indeed, the method requires a set of data obtained by simulations. However, these simulation data can be complex to generate. Concerning the PGD, the use of the method is still complex to be implemented in a commercial software.

Model order reduction techniques must be selected considering the type of finite element modelling being used. In this chapter, section [V.2](#), a model is proposed to compute the stationary dynamic response of gearboxes. The model consists of parametric excitations (STE and mesh stiffness fluctuations) to couple the lumped masses of the input/output gears. Additionally, the flexible shafts, the bearings and in the housing are condensed to master nodes using component mode synthesis method. The CMS is well suited for this model since the coupling with STE and the mesh stiffness replace the

gear contact interactions. In the section [V.3](#), a flexible multibody model of a gear pair is proposed to compute the transient gear contact dynamics. In this context, the CMS reduction method requires very large interfaces, thus it becomes inefficient. We introduce thus two strategies to reduce the flexible multibody model. Firstly, we consider a reduced basis with POD and mode shapes of the system, and then, we propose a strategy based on Krylov subspace.

## 2 Stationary dynamic response

This section presents the strategy retained to compute the stationary dynamic response of a complete gearbox. Hereafter, the gear coupling is performed using the STE and the mesh stiffness and the flexible shafts and the housing are condensed using the CMS approach. The gearbox model is described and the resulting parametric equations of motion in the physical and reduced space are derived. Firstly, preliminary validations for the CMS in this context is validated and then the stationary dynamic response for two cases of study is presented.

### 2.1 Computation procedure

A detailed description of the gearbox modelling approach and the numerical strategy in the frequency domain for the dynamic response is put forward. The gearbox is composed of lumped masses and inertia for the gear pair, stiffness elements for bearings and 3D finite element for shafts and the housing. The gearbox is driven with a rotational speed through the input shaft and the output torque is applied to the output shaft. The same gearboxes presented in [Fig. IV.6](#) and [Fig. IV.7](#) are used.

### 2.1.1 Description of the gearbox's model

The gear mesh is modelled by a parametric excitation along the line of action. The line of action is the line tangent to the base circles along which theoretical contact points are located. The gear mesh element is modelled as represented in Fig. II.3. The input and output gear consist of lumped masses with 6 degrees-of-freedom (3 translations and 3 rotations) for each and a control node defined at each gear centre. The housing and the flexible shafts are discretized with FE method using tetra and hexa-linear elements and they are connected with bearings considered as additional radial stiffness elements. The corresponding values of the radial stiffness elements are outlined in the Table V.1. A tip relief modification is introduced to smooth the meshing process and to minimize STE fluctuations for an output torque  $T = 115$  N m.

Table V.1: Characteristics of the radial stiffness elements

Bearings	$k_{xx}$	$k_{yy}$	$k_{zz}$	Unit
Input shaft	9e7	1.5e8	1.8e7	N/m
Output shaft	9e7	1.5e8	1.8e7	N/m

### 2.1.2 Equation of motion

The equation of motion for describing the dynamic response of the discretized FE model of the gearbox is derived. STE and mesh stiffness fluctuations are introduced as an internal excitation for a given output torque  $T$ . Gear mesh forces are linearized by the first-order Taylor-Young expansion around a static state as follows:

$$\mathbf{F}_{nl}(\mathbf{x}) \approx \mathbf{F}_{nl}(\mathbf{x}_s) + \frac{\partial \mathbf{F}_{nl}}{\partial \mathbf{x}_s}(\mathbf{x} - \mathbf{x}_s) \quad (\text{V.32})$$

where  $\mathbf{x}$  contains the generalised displacement of each degree-of-freedom and  $\mathbf{F}_{nl}$  are the gear mesh forces.  $\mathbf{x}_s$  represents the solution of the static equilibrium:

$$\mathbf{K}\mathbf{x} + \mathbf{F}_{nl}(\mathbf{x}) = \mathbf{F}_s \quad (\text{V.33})$$

and  $\mathbf{F}_s = \mathbf{T}/R_{b1}$  corresponds to the transmitted load. The dynamic equation of motion is thus linearized:

$$\mathbf{M}\ddot{\mathbf{x}} + \mathbf{C}\dot{\mathbf{x}} + \mathbf{K}\mathbf{x} + \mathbf{F}_{nl}(\mathbf{x}_s) + \frac{\partial \mathbf{F}_{nl}}{\partial \mathbf{x}_s}(\mathbf{x} - \mathbf{x}_s) = \mathbf{F}_s \quad (\text{V.34})$$

$\mathbf{M}$ ,  $\mathbf{C}$ ,  $\mathbf{K}$  are respectively the mass, damping and stiffness matrix of the complete gearbox. Using the eq. V.33 we obtain:

$$\mathbf{M}\ddot{\mathbf{x}} + \mathbf{C}\dot{\mathbf{x}} + \mathbf{K}(\mathbf{x} - \mathbf{x}_s) + \frac{\partial \mathbf{F}_{nl}}{\partial \mathbf{x}_s}(\mathbf{x} - \mathbf{x}_s) = 0 \quad (\text{V.35})$$

The STE is determined using the geometrical column vector  $\mathbf{G}$  in the reference frame  $(O_1, \vec{\mathbf{x}}_0, \vec{\mathbf{y}}_0, \vec{\mathbf{z}}_0)$  associated with the gear design parameters (see Fig. V.2). This vector  $\mathbf{G}$  as defined in II.2 has 12 non-zero values that couple the 6 degrees-of-freedom of the input gear with the 6 degrees-of-freedom of the output gear. The corresponding STE  $\delta_s(t)$  which is a time-dependant static solution is defined by:

$$\delta_s(t) = \mathbf{G}^T \mathbf{x}_s(t) \quad (\text{V.36})$$

similarly the dynamic transmission error (DTE)  $\delta_d(t)$  can be expressed as:

$$\delta_d(t) = \mathbf{G}^T \mathbf{x}(t) \quad (\text{V.37})$$



with  $\mathbf{K}^{av}$  the global time-averaged stiffness matrix:

$$\mathbf{K}^{av} = \mathbf{K} + [\mathbf{G}\mathbf{G}^T k_{av}] \quad (\text{V.42})$$

For the sake of completeness, the static contribution of the gearbox is represented by the static deflection of the entire gearbox considering the loaded gear pair. For this purpose, the static transmission error is calculated considering the entire gearbox as presented for the model Fig. IV.7. Additionally, in this dissertation, the work focuses on the whining noise which is generated by the fluctuation of the DTE.

### 2.1.3 Component mode synthesis reduction

The discretized FE model of the gearbox is a large-scale FE model. The objective of this section is to approximate the solution of the equation of motion V.41 with the CMS method as described in section 1.3.2. The generalized displacement  $\mathbf{x}$  is related to the reduced displacement  $\mathbf{q}$  thanks to the approximation  $\mathbf{x} = \mathbf{\Psi}\mathbf{q}$ , where  $\mathbf{\Psi}$  stands for the reduced transformation basis. The reduced basis  $\mathbf{\Psi}$  must be built to span a subspace for which the solution of the full model is well approximated. The equation of motion in the reduced space can be written as follows:

$$\mathbf{M}_r \ddot{\mathbf{q}} + \mathbf{C}_r \dot{\mathbf{q}} + \mathbf{K}_r^{av} (\mathbf{q} - \mathbf{q}_s) + [\mathbf{L}\mathbf{L}^T g(t)] (\mathbf{q} - \mathbf{q}_s) = 0 \quad (\text{V.43})$$

where the reduced matrices take the form:

$$\mathbf{M}_r = \mathbf{\Psi}^T \mathbf{M} \mathbf{\Psi} \quad \mathbf{C}_r = \mathbf{\Psi}^T \mathbf{C} \mathbf{\Psi} \quad \mathbf{K}_r^{av} = \mathbf{\Psi}^T \mathbf{K}^{av} \mathbf{\Psi} \quad \mathbf{L} = \mathbf{\Psi}^T \mathbf{G} \quad (\text{V.44})$$

## 2.2 Numerical strategy in the frequency domain

The aim of this section is to obtain the stationary dynamic response of the parametric equation of motion V.43. The strategy employed is to derive the equation of motion in the frequency domain. The strategy is equivalent to the Harmonic Balance Method [4, 5, 51, 50, 101]. The time varying quantities  $\ddot{\mathbf{q}}(t)$ ,  $\dot{\mathbf{q}}(t)$ ,  $\mathbf{q}(t)$ ,  $\mathbf{q}_s(t)$  and  $g(t)$  are thus expressed as truncated Fourier series. Solving the equation of motion in the frequency domain using the CMS reduction method allows a fast computation of the stationary dynamic response compared to time integration methods and/or direct inversion of the full system. The equation V.43 can be re-written as follows:

$$\mathbf{M}_r \ddot{\mathbf{q}} + \mathbf{C}_r \dot{\mathbf{q}} + \mathbf{K}_r^{av} \mathbf{q} + [\mathbf{L}\mathbf{L}^T g(t)] \mathbf{q} = \mathbf{S}(t) \quad (\text{V.45})$$

The truncated Fourier series of the time varying quantities are for  $H$  harmonics:

$$\mathbf{q}(t) \approx \mathbf{q}_0 + \sum_{p=1}^H \mathbf{q}_a^p \cos(p\omega t) + \mathbf{q}_b^p \sin(p\omega t) \quad (\text{V.46})$$

$$g(t) \approx \sum_{m=1}^H g_a^m \cos(m\omega t) + g_b^m \sin(m\omega t) \quad (\text{V.47})$$

The term  $\mathbf{S}(t) = [\mathbf{L}\mathbf{L}^T g(t)] \mathbf{q}_s(t) + \mathbf{K}_r^{av} \mathbf{q}_s$  can be pre-computed since the STE and mesh stiffness fluctuations are known at this stage. The associated Fourier coefficients are stored in  $\tilde{\mathbf{S}}(\omega)$ . The term  $[\mathbf{L}\mathbf{L}^T g(t)] \mathbf{q}(t)$  is developed by means of the Fourier serie product in order to reduce the time cost. Indeed, the Fourier serie product enables the creation of a matrix  $\mathbf{A}$  that can be pre-determined and

used at each frequency. Developments leads to:

$$\begin{aligned}
[\mathbf{L}\mathbf{L}^T g(t)]\mathbf{q}(t) &= \left( [\mathbf{L}\mathbf{L}^T \sum_{m=1}^H g_a^m \cos(m\omega t) + g_b^m \sin(m\omega t)] \right) \left( \mathbf{q}_0 + \sum_{p=1}^H \mathbf{q}_a^p \cos(p\omega t) + \mathbf{q}_b^p \sin(p\omega t) \right) \\
&= \mathbf{q}_0 \left( [\mathbf{L}\mathbf{L}^T \sum_{m=1}^H g_a^m \cos(m\omega t) + g_b^m \sin(m\omega t)] \right) + \\
&\frac{1}{2} \sum_{m=1}^H \left( [\mathbf{L}\mathbf{L}^T g_a^m] \sum_{p=1}^H \left( \mathbf{q}_a^p (\cos((p-m)\omega t) + \cos((p+m)\omega t)) + \mathbf{q}_b^p (\sin((p+m)\omega t) + \cos((p-m)\omega t)) \right) \right. \\
&\left. + [\mathbf{L}\mathbf{L}^T g_b^m] \sum_{p=1}^H \left( \mathbf{q}_a^p (\sin((p+m)\omega t) - \sin((p-m)\omega t)) + \mathbf{q}_b^p (\cos((p-m)\omega t) - \cos((p+m)\omega t)) \right) \right)
\end{aligned}$$

Assembling the equation per terms gives:

$$\begin{aligned}
[\mathbf{L}\mathbf{L}^T g(t)]\mathbf{q}(t) &= \mathbf{q}_0 \left( [\mathbf{L}\mathbf{L}^T \sum_{m=1}^H g_a^m \cos(m\omega t) + g_b^m \sin(m\omega t)] \right) \\
&+ \frac{1}{2} \sum_{m=1}^H \left( \sum_{p=1}^H \left( ([\mathbf{L}\mathbf{L}^T g_a^m] \mathbf{q}_a^p + [\mathbf{L}\mathbf{L}^T g_b^m] \mathbf{q}_b^p) \cos((p-m)\omega t) \right. \right. \\
&+ ([\mathbf{L}\mathbf{L}^T g_a^m] \mathbf{q}_b^p - [\mathbf{L}\mathbf{L}^T g_b^m] \mathbf{q}_a^p) \sin((p-m)\omega t) + ([\mathbf{L}\mathbf{L}^T g_a^m] \mathbf{q}_a^p - [\mathbf{L}\mathbf{L}^T g_b^m] \mathbf{q}_b^p) \cos((p+m)\omega t) \\
&\left. \left. + ([\mathbf{L}\mathbf{L}^T g_a^m] \mathbf{q}_b^p + [\mathbf{L}\mathbf{L}^T g_b^m] \mathbf{q}_a^p) \sin((p+m)\omega t) \right) \right) \\
&= [\mathbf{L}\mathbf{L}^T \otimes \mathbf{A}_g] \tilde{\mathbf{q}}(\omega)
\end{aligned}$$

with:

$$\mathbf{A}_g = \begin{bmatrix} 0 & \frac{g_a^1}{2} & \frac{g_b^1}{2} & \frac{g_a^2}{2} & \frac{g_b^2}{2} & \dots & \frac{g_a^{H-1}}{2} & \frac{g_b^{H-1}}{2} & \frac{g_a^H}{2} & \frac{g_b^H}{2} \\ g_a^1 & \frac{g_a^2}{2} & \frac{g_b^2}{2} & \frac{g_a^1}{2} + \frac{g_a^3}{2} & \frac{g_b^1}{2} + \frac{g_b^3}{2} & \dots & \frac{g_a^{H-2}}{2} + \frac{g_a^H}{2} & \frac{g_b^{H-2}}{2} + \frac{g_b^H}{2} & \frac{g_a^{H-1}}{2} & \frac{g_b^{H-1}}{2} \\ g_b^1 & \frac{g_b^2}{2} & -\frac{g_a^2}{2} & -\frac{g_b^1}{2} + \frac{g_b^3}{2} & \frac{g_a^1}{2} - \frac{g_a^3}{2} & \dots & -\frac{g_b^{H-2}}{2} + \frac{g_b^H}{2} & \frac{g_a^{H-2}}{2} - \frac{g_a^H}{2} & -\frac{g_b^{H-1}}{2} & \frac{g_a^{H-1}}{2} \\ g_a^2 & \frac{g_a^1}{2} & -\frac{g_b^1}{2} & \frac{g_a^3}{2} & \frac{g_b^3}{2} & \dots & \frac{g_a^{H-3}}{2} + \frac{g_a^H}{2} & \frac{g_b^{H-3}}{2} + \frac{g_b^H}{2} & \frac{g_a^{H-2}}{2} & \frac{g_b^{H-2}}{2} \\ g_b^2 & \frac{g_b^1}{2} & \frac{g_a^1}{2} & \frac{g_b^3}{2} & -\frac{g_a^3}{2} & \dots & -\frac{g_b^{H-3}}{2} + \frac{g_b^H}{2} & \frac{g_a^{H-3}}{2} - \frac{g_a^H}{2} & -\frac{g_b^{H-2}}{2} & \frac{g_a^{H-2}}{2} \\ \dots & \dots \\ g_a^{H-1} & \frac{g_a^{H-2}}{2} & -\frac{g_b^{H-2}}{2} & \frac{g_a^{H-3}}{2} & -\frac{g_b^{H-3}}{2} & \dots & \frac{g_a^H}{2} & \frac{g_b^H}{2} & \frac{g_a^1}{2} & \frac{g_b^1}{2} \\ g_b^{H-1} & \frac{g_b^{H-2}}{2} & \frac{g_a^{H-2}}{2} & \frac{g_b^{H-3}}{2} & \frac{g_a^{H-3}}{2} & \dots & \frac{g_b^H}{2} & -\frac{g_a^H}{2} & -\frac{g_b^1}{2} & \frac{g_a^1}{2} \\ g_a^H & \frac{g_a^{H-1}}{2} & -\frac{g_b^{H-1}}{2} & \frac{g_a^{H-2}}{2} & -\frac{g_b^{H-2}}{2} & \dots & \frac{g_a^1}{2} & -\frac{g_b^1}{2} & 0 & 0 \\ g_b^H & \frac{g_b^{H-1}}{2} & \frac{g_a^{H-1}}{2} & \frac{g_b^{H-2}}{2} & \frac{g_a^{H-2}}{2} & \dots & \frac{g_b^1}{2} & \frac{g_a^1}{2} & 0 & 0 \end{bmatrix}$$

and  $\otimes$  is the Kronecker product. The substitution of the truncated Fourier series into the equation of motion V.45 conducts to:

$$[\mathbf{Z}(\omega)]\tilde{\mathbf{q}}(\omega) + [\mathbf{L}\mathbf{L}^T \otimes \mathbf{A}_g]\tilde{\mathbf{q}}(\omega) = \tilde{\mathbf{S}}(\omega) \quad (\text{V.48})$$

where  $\tilde{\mathbf{q}}(\omega)$  contains the Fourier coefficients of  $\mathbf{q}(t)$ . The matrix  $[\mathbf{Z}(\omega)]$  is built by assembling submatrices. This submatrices  $[\mathbf{Z}_p(\omega)]$  are expressed to each harmonic as follows:

$$[\mathbf{Z}_p(\omega)] = \begin{bmatrix} \mathbf{K}_{av}^r - (p\omega)^2\mathbf{M}_r & p\omega\mathbf{C}_r \\ -p\omega\mathbf{C}_r & \mathbf{K}_r^{av} - (p\omega)^2\mathbf{M}_r \end{bmatrix}, \quad 1 \leq p \leq H \quad (\text{V.49})$$

The equation of motion V.45 consists of well-conditioned matrices which allows us to use an iterative solving procedure. Solutions are obtained at mesh frequency and its harmonics. These solutions are then used to reconstruct the time history solutions using the inverse Fourier transform.

## 2.3 Results and discussion

This section is a dynamic analysis of the gearboxes considering the models described in Fig. IV.7.

The objective hereafter is firstly to validate the CMS method and then to discuss the results for these particular cases. For this purpose, stationary dynamic responses of the gearboxes for the model

in the physical space (full model/without reduction) and the CMS reduced model are computed and compared. The full model is solved on a cluster using CPU resources (1 computer node = 16 cores, 2.6 GHz and 64 Go RAM) in order to achieve the simulation. 4 computer nodes (64 cores) are retained for the computation. In contrast, the simulation of the CMS reduced model is performed with a personal computer (8 cores, processor intel Xeon E5-1607 V3 3,10GHz, 16 Go RAM). Simulations are conducted for a rotational input speed  $\Omega$  from  $\Omega = 1$  rpm to  $\Omega = 9000$  rpm. The static transmission error and the mesh stiffness fluctuations as displayed in Fig. V.3 are the internal excitations.

The ratio  $A_{SD}$  of the standard deviation of the dynamic transmission error  $DTE_{SD}$  with respect to the standard deviation of the static transmission error  $STE_{SD}$  is the quantity used for the comparison:

$$A_{SD} = \frac{DTE_{SD}}{STE_{SD}} \quad (\text{V.50})$$

where SD states for standard deviation.

The full model represents the large scale FE model of the gearbox without reduction. The CMS reduced model features the FE model of the gearbox using the CMS method and 408 fixed interface modes are retained. The location of the master nodes for the CMS method are the center of the gear pair and the center of the face where the housing is fixed. This choice takes into account the complete energetic contribution of the gearbox. 100 and 300 discrete computed frequencies are considered for the full model and the CMS reduced model, respectively.

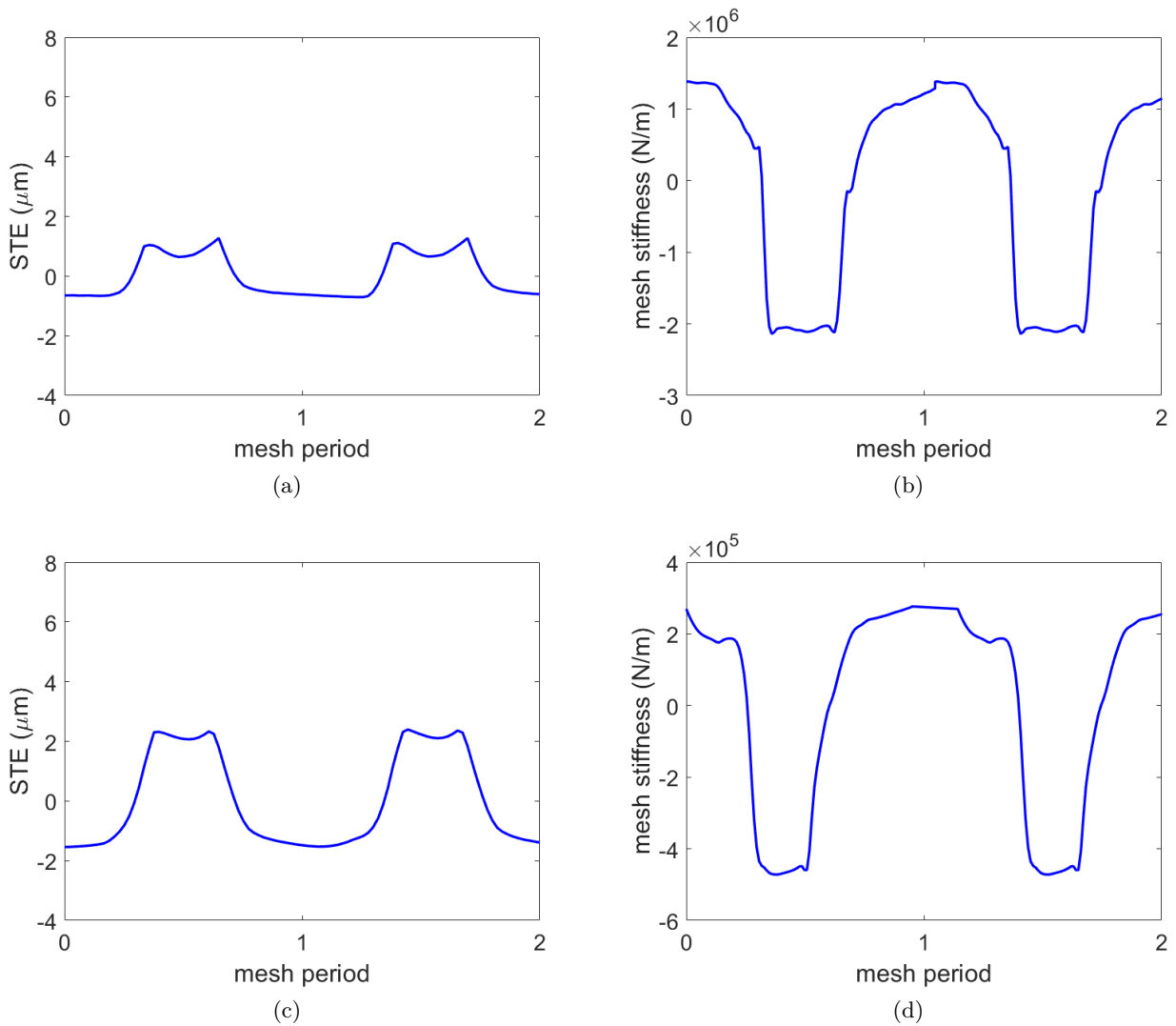


Figure V.3: (a,b) represents the static transmission error and mesh stiffness fluctuations for the short gearbox (see IV.7b). (c,d) represents the static transmission error and mesh stiffness fluctuations for the long gearbox (see IV.7a).

Figure V.4 displays the ratio  $A_{SD}$  for an output torque  $T = 115$  N m. The associated time needed to solve for the full model and the CMS reduced model are 15 hours and 35 minutes, respectively. It appears parametric resonances at the critical frequencies identified in Fig. V.5. Results of the CMS reduced model match perfectly with those of the full model (see Fig. V.5). This CMS reduced model of the gearbox enables therefore the fast computation of the dynamic response with great accuracy.

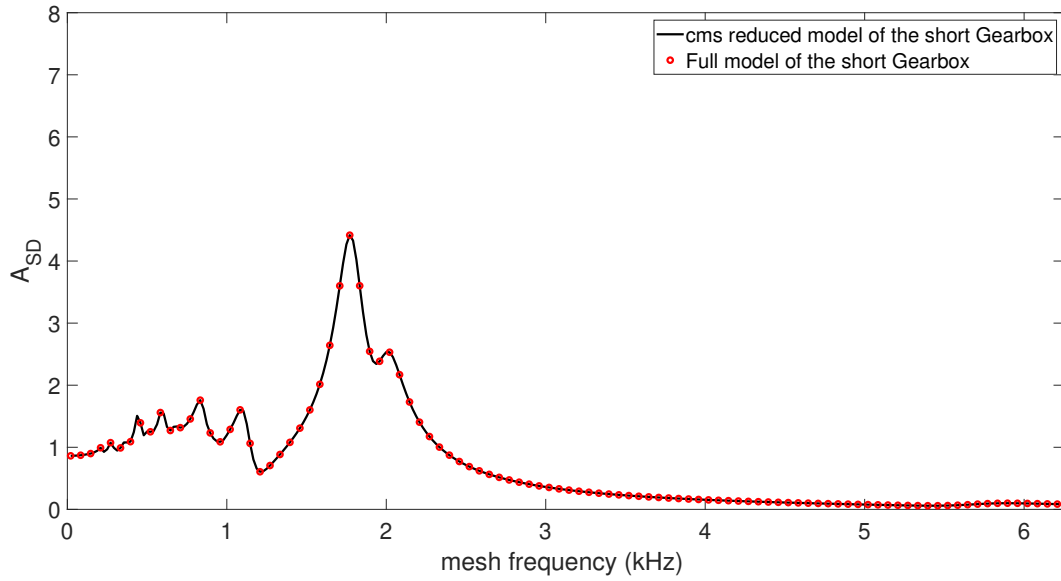


Figure V.4: Dynamic response of the gearbox for the full model (●) and the CMS reduced model (—) for an output torque  $T = 115$  N m..

The CMS reduced model allows the fast computation of the dynamic response of the short and long gearbox. Dynamical responses are computed for the optimal output torque of the standard gear pair  $T = 115$  N m. One can see that long gearbox compared to the short gearbox re-organized the critical frequencies of the gearbox. Indeed, critical frequencies are shifted to lower frequencies. Additionally, the long gearbox induced higher amplitude of the parametric resonances. For instance, considering the primary resonance for the long and short gearbox  $A_{SD} = 5.5$  and  $A_{SD} = 4.4$  respectively.

### 3 Transient dynamic response

This section investigates the potential of using a multibody framework coupled with model order reduction for the computation of the transient gear dynamics. Thus, the equation of multibody dynamics including flexible bodies are derived. The strategies for reducing the model are presented

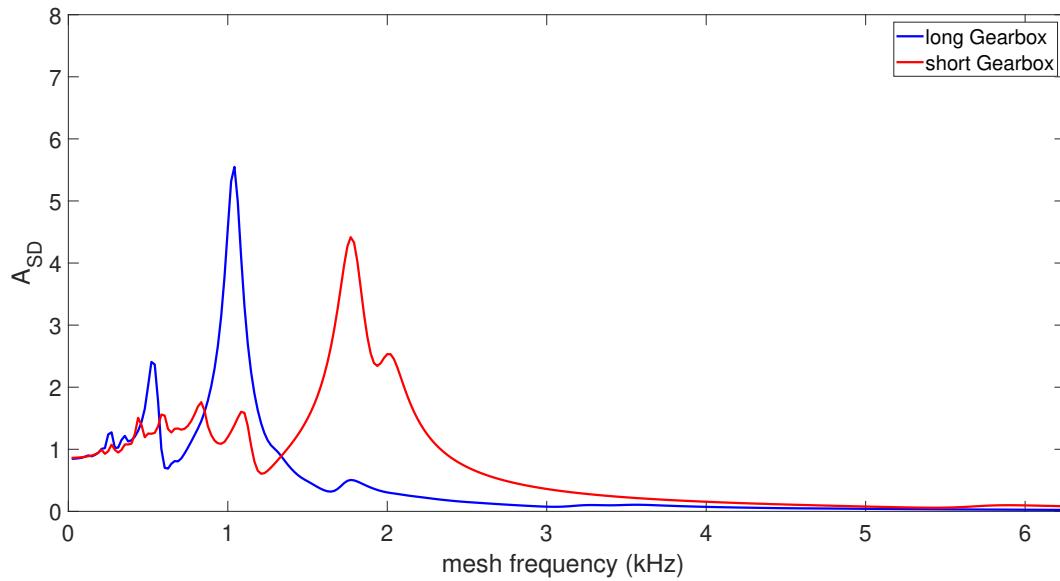


Figure V.5: Dynamic response of the short gearbox (—) and the long gearbox (—) for an output torque  $T = 115$  N m.

and preliminary validations are proposed. Then, an original model for considering gears in a multibody framework is described and the resolution of motion equations is achieved. Moreover, a particular attention to the numerical method used for the integration of the equation of motion is enforced.

### 3.1 Equation of motion of flexible multibody dynamics

Multibody dynamics is the study of the motion of assemblies of bodies, rigid or flexible, that undergo large motion in the 3D space (see Fig. V.6). The free motion of bodies is restrained by joints. Every joint links two bodies in two points. These joints are idealizations of the contact between the two bodies. Joints are characterized by the motion that they allow between the two bodies that they connect. The primary unknowns of a multibody dynamics solution are the translation and rotation of each body and the motion in the joints themselves. The output quantities on rigid bodies are the forces that develop in the joints and flow through the rigid bodies. Flexible bodies can be included

in a multibody analysis. These flexible bodies will have both joint forces and stress and strain results.

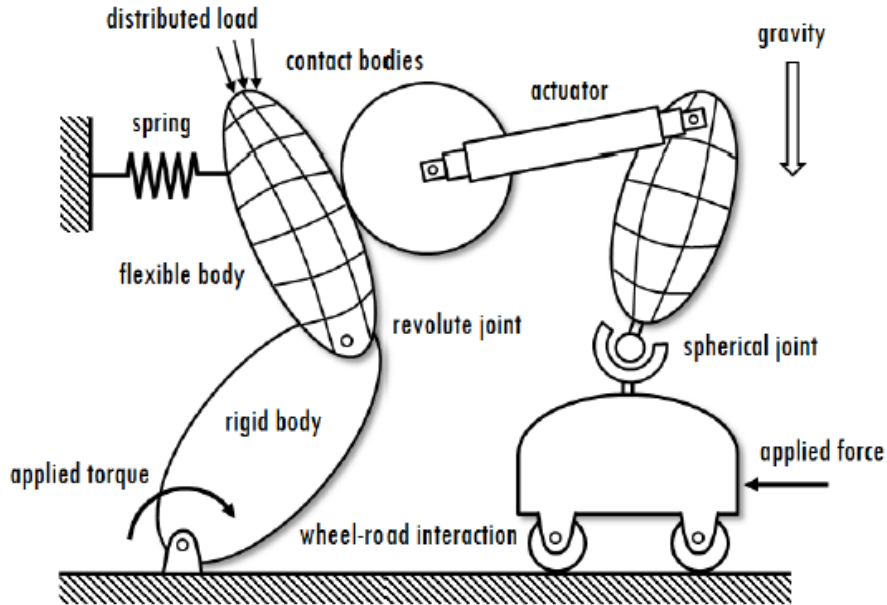


Figure V.6: Schematic representation of a multibody system.

The absolute position of a given body  $k$  is determined by the position of a point  $M_k$  of the considered body, and the orientation of the body with respect to a fixed reference frame  $(O, e_x, e_y, e_z)$ . A material frame  $(O_k, e_{xk}, e_{yk}, e_{zk})$  is attached to the rigid body  $k$ , with its origin (reference point) located at the center of mass. An arbitrary point  $M_k$  attached to this material frame has material coordinates  $(x_k, y_k, z_k)$ . So, from initial to current configuration, time-dependent rotation of the body  $k$  occurs in the material frame. The absolute position of the body  $k$  considered as rigid is thus expressed as:

$$\mathbf{OM}_k = \mathbf{OO}_k + \mathbf{O}_k \mathbf{M}_k \quad (\text{V.51})$$

In multibody dynamics, the main source of nonlinearities are large relative translations and rotations between bodies. The flexibility of the body can be taken into account by assuming that inside the body, its elastic behaviour remains linear within a local frame. In other words, the body undergoes small elastic deformations. So, the strain tensor is linearized as follows:

$$\boldsymbol{\varepsilon}_L(\mathbf{u}) = \frac{1}{2}(\nabla\mathbf{u} + (\nabla\mathbf{u})^T) \quad (\text{V.52})$$

Fig. V.7 introduces the notion of parent body. This flexible multibody framework is used hereafter. Additionally, in this dissertation, the flexibility of the body is introduced to the equation V.51 using model order reduction. Indeed, the generalized position of  $M'_k$  associated to the flexible body becomes:

$$\mathbf{O}\mathbf{M}'_k = \mathbf{O}\mathbf{O}_k + \mathbf{O}_k\mathbf{M}_k + \mathbf{M}_k\mathbf{M}'_k = \mathbf{O}\mathbf{O}_k + \mathbf{O}_k\mathbf{M}_k + \boldsymbol{\Psi}\mathbf{q} \quad (\text{V.53})$$

Point  $O_k$  is a joint or the center of gravity the body  $k$ . The generalized velocity of  $M'_k$  is expressed by:

$$\mathbf{V}_{M'_k/O} = \mathbf{V}_{O_k/O} + \boldsymbol{\Omega}_{k/O} \wedge \mathbf{O}_k\mathbf{M} + \boldsymbol{\Omega}_{k/O} \wedge \boldsymbol{\Psi}\mathbf{q} + \boldsymbol{\Psi}\dot{\mathbf{q}} \quad (\text{V.54})$$

where  $\boldsymbol{\Omega}_{k/O}$  is the angular velocity of the body  $k$  with respect to the ground. Similarly,  $\mathbf{V}_{O_k/O}$  is the velocity of the body  $k$  with respect to the ground  $(O, e_x, e_y, e_z)$ . The concept of recursive calculation of the generalized velocities is introduced. The generalized velocities on body  $k$  can be computed by adding the contribution of the parent joint to the generalized velocities of body  $L(k)$ . The contribution of each joint in the chain between body  $k$  and the ground  $(O, e_x, e_y, e_z)$  can be found by expressing

- : Joint between bodies
- $L(k)$  : Parent body of the body  $k$

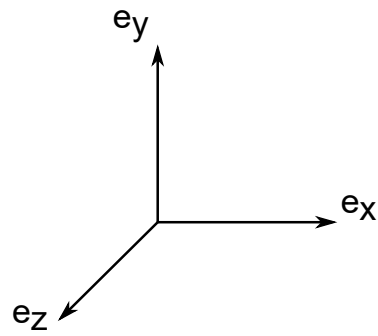
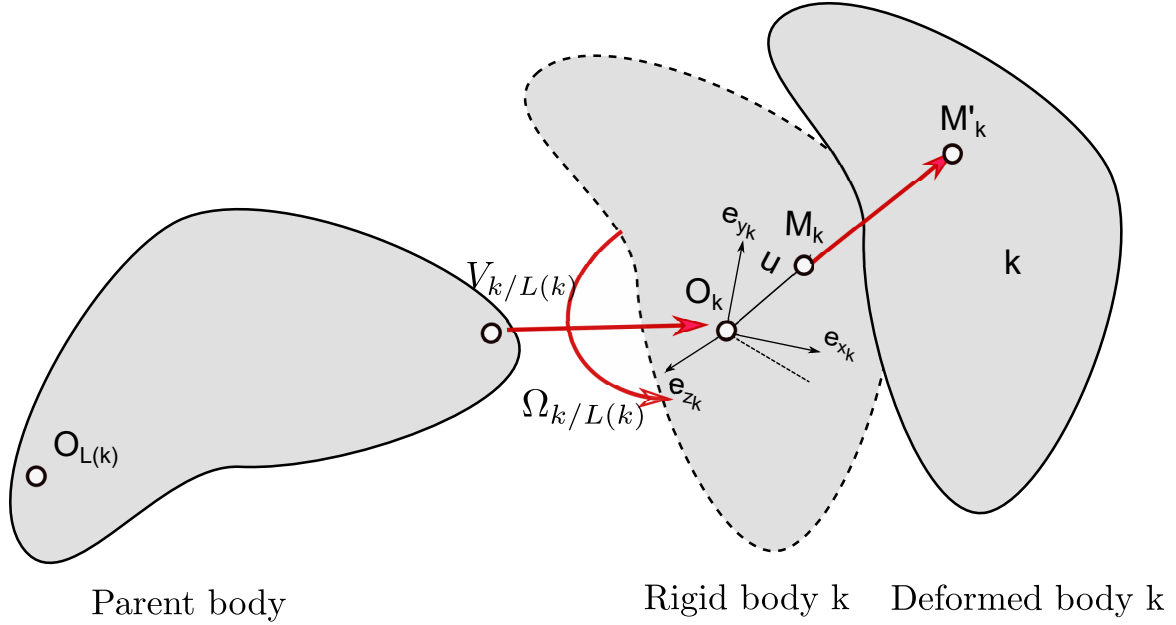


Figure V.7: Schematic representation of flexible multibody systems

the velocity and the angular velocity as:

$$\mathbf{V}_{M_k/O} = \sum_l^{N_b} \mathbf{V}_l \dot{\eta}_l \tag{V.55}$$

$$\boldsymbol{\Omega}_{k/O} = \sum_l^{N_b} \boldsymbol{\Omega}_l \dot{\eta}_l \tag{V.56}$$

Where  $N_b$  is the number of bodies between body  $k$  and the ground  $(O, e_x, e_y, e_z)$ .  $\mathbf{V}_l$  and  $\boldsymbol{\Omega}_l$  are called partial velocity and partial angular velocity associated to the kinematic variable  $\eta_l$  at point

$M_k$ , respectively. They can be seen as rigid shape functions. For the sake of simplicity, the Einstein convention is used, which gives:  $\mathbf{V}_{M_k/O} = \mathbf{V}_l \dot{\eta}_l$  and  $\boldsymbol{\Omega}_{k/O} = \boldsymbol{\Omega}_l \dot{\eta}_l$ . Thus, the equation V.54 yields:

$$\mathbf{V}_{M'_k/O} = \mathbf{V}_l \dot{\eta}_l + \boldsymbol{\Omega}_l \dot{\eta}_l \wedge (\mathbf{O}_k \mathbf{M} + \boldsymbol{\Psi} \mathbf{q}) + \boldsymbol{\Psi} \dot{\mathbf{q}} \quad (\text{V.57})$$

Compared to the rigid case, the generalized position and velocity are modified to be expressed at the flexible point location  $M'_k$ , through the contributions of  $\boldsymbol{\Psi} \mathbf{q}$  and  $\boldsymbol{\Psi} \dot{\mathbf{q}}$  that reflects the flexible part. The reduced basis  $\boldsymbol{\Psi}$  is obtained in the following thanks to a reduced order method as described in the section V.1.

To derive the equation of motion of flexible multibody dynamics, different approaches can be used. The most popular methods are based on the Hamilton's principle or the virtual work. Here, we formulate the equation of motion using the virtual work as proposed in [1, 80, 110, 144, 121] which is equivalent to the d'Alembert principle. The derivation of the generalized velocity (eq. V.57) gives the generalized acceleration of the point  $M'_k$ :

$$\boldsymbol{\Gamma}_{M'_k/O} = \mathbf{V}_l \ddot{\eta}_l + \dot{\mathbf{V}}_l \dot{\eta}_l + (\boldsymbol{\Omega}_l \ddot{\eta}_l + \dot{\boldsymbol{\Omega}}_l \dot{\eta}_l) \wedge (\mathbf{O}_k \mathbf{M} + \boldsymbol{\Psi} \mathbf{q}) + \boldsymbol{\Omega}_l \dot{\mathbf{q}} \wedge (\boldsymbol{\Omega}_l \dot{\eta}_l \wedge \mathbf{O}_k \mathbf{M}') + 2 \cdot \boldsymbol{\Omega}_l \dot{\eta}_l \wedge (\boldsymbol{\Psi} \dot{\mathbf{q}}) + \boldsymbol{\Psi} \ddot{\mathbf{q}} \quad (\text{V.58})$$

The principle of virtual power can be formulated by:

$$\begin{cases} \text{Find } (\eta, \mathbf{q}) \in \mathcal{B} \\ \forall (\eta^*, \mathbf{q}^*) \in \mathcal{B}, \quad \delta \mathcal{W}_a(\eta, \mathbf{q}, \eta^*, \mathbf{q}^*) = \delta \mathcal{W}_{ext}(\eta, \mathbf{q}, \eta^*, \mathbf{q}^*) \end{cases} \quad (\text{V.59})$$

$\delta \mathcal{W}_a$  and  $\delta \mathcal{W}_{ext}$  are the virtual work of the acceleration and the virtual work of the external forces,

respectively.  $(\eta^*, \mathbf{q}^*)$  are the virtual fields for the kinematic and flexible variables.  $\mathcal{B}$  is the collection of rigid and flexible bodies. The virtual displacement of a point  $M'_k$  of the body  $k$  reads:

$$\mathbf{r}_{M'_k/O}^* = \mathbf{V}_m \eta_m^* + \boldsymbol{\Omega}_m \eta_m^* \wedge (\mathbf{O}_k \mathbf{M} + \boldsymbol{\Psi} \mathbf{q}^*) + \boldsymbol{\Psi} \mathbf{q}^* \quad (\text{V.60})$$

the virtual work can be formed and integrated over body  $k$ , and summed over the bodies. The virtual works are thus:

$$\delta \mathcal{W}_a(\eta, \mathbf{q}, \eta^*, \mathbf{q}^*) = \sum_k \int_{\mathcal{B}_k} \boldsymbol{\Gamma}_{M'_k/O} \cdot \mathbf{r}_{M'_k}^* d\mathcal{V}_k \quad (\text{V.61})$$

$$\delta \mathcal{W}_{ext}(\eta, \mathbf{q}, \eta^*, \mathbf{q}^*) = \sum_k \int_{\mathcal{B}_k} \mathbf{F}_{V,M'_k/O}^{ext} \cdot \mathbf{r}_{M'_k/O}^* d\mathcal{V}_k + \sum_k \int_{\partial \mathcal{B}_k} \mathbf{F}_{S,M'_k/O}^{ext} \cdot \mathbf{r}_{M'_k/O}^* d\mathcal{S}_k \quad (\text{V.62})$$

The terms  $\mathbf{F}_{V,M'_k/O}^{ext}$  and  $\mathbf{F}_{S,M'_k/O}^{ext}$  are the field of volume density of forces and field of surface density of forces, respectively. In the presence of flexible bodies, the equations of motion can be partitioned into 2 sets of terms. Terms that involve only the set of rigid degrees of freedom. The reason is that this leads to the well known rigid body formulation. Then adding the flexible dofs introduces new terms. In practice, to deal with flexible bodies in a multibody framework, the multibody solver needs to be coupled with a finite element solver for modelling the flexible part and computing therefore the flexible matrices. These matrices are the reduced basis  $\boldsymbol{\Psi}$ , the reduced matrices  $\mathbf{M}_r$ ,  $\mathbf{K}_r$ ,  $\mathbf{C}_r$ , the reduced load vector  $\mathbf{f}_r$  and the lumped mass matrix  $\mathbf{M}^l$  which is obtained from the full finite element mass matrix  $\mathbf{M}$  of the flexible bodies. The lumped matrix is a diagonal matrix that simplify the matrix vector product. In the approach used in this dissertation, the equilibrium is written on the current (deformed) configuration, the mass matrix and right hand side terms (RHS) depend on the flexible

degrees of freedom. To avoid having to go back to the finite element solver to compute these integrals during the transient simulation, these terms are decomposed over a basis of invariant terms, which are computed only once before the resolution of the equation of motion using the reduced basis and the lumped mass matrix. We consider 6 dofs per nodes and the lumped mass matrix  $\mathcal{M}^l$  is diagonal with these properties:

$$m_k = \begin{cases} \mathcal{M}_{6k,6k}^l = \mathcal{M}_{6k+1,6k+1}^l = \mathcal{M}_{6k+2,6k+2}^l \\ \mathcal{M}_{6k+3,6k+3}^l = \mathcal{M}_{6k+4,6k+4}^l = \mathcal{M}_{6k+5,6k+5}^l = 0 \end{cases} \quad (\text{V.63})$$

These invariant terms are expressed for each mode. Mode  $j$ , component  $i$  at node  $k$  is expressed as:

$$\Psi_{k,i}^j = \Psi_{6k+i}^j$$

with

$$\Psi_k^j = \begin{pmatrix} \Psi_{k,0}^j \\ \Psi_{k,1}^j \\ \Psi_{k,2}^j \end{pmatrix}$$

The invariant terms are thus formulated as:

$$\mathcal{I}_1 = \sum_{k=0}^{nbNodes-1} m_k \Psi_{k,i}^j, i = 0..2, j = 0..nbModes - 1 \quad (nbModes \times 3) \quad (\text{V.64})$$

$$\mathcal{I}_2 = \sum_{k=0}^{nbNodes-1} m_k \left( \mathbf{P}_k \wedge \Psi_k^j \right)_i, i = 0..2, j = 0..nbModes - 1 \quad (nbModes \times 3) \quad (\text{V.65})$$

with  $\mathbf{P}_k$  the coordinates of the node  $k$  in the global coordinate system.

$$\mathcal{I}_3 = \sum_{k=0}^{nbNodes-1} m_k \left( \mathbf{P}_k \cdot \Psi_k^j \right), i = 0..2, j = 0..nbModes - 1 \quad (nbModes \times 1) \quad (\text{V.66})$$

$$\mathcal{I}_4 = \sum_{k=0}^{nbNodes-1} m_k \left( \Psi_{k,0}^j \mathbf{P}_k \right), j = 0..nbModes - 1 \quad (nbModes \times 1) \quad \textit{respectively for } \Psi_{k,1}^j \textit{ and } \Psi_{k,2}^j. \quad (\text{V.67})$$

$$\mathcal{I}_5 = \sum_{k=0}^{nbNodes-1} m_k \left( P_{k,0} \Psi_k^j \right), j = 0 \dots nbModes - 1 \quad (nbModes \times 1) \text{ respectively for } P_{k,1} \text{ and } P_{k,2}. \quad (\text{V.68})$$

$$\mathcal{I}_6 = \sum_{k=0}^{nbNodes-1} m_k \left( \Psi_k^i \cdot \Psi_k^j \right), i = 0 \dots nbModes - 1, j = 0 \dots nbModes - 1 \quad (nbModes \times nbModes) \quad (\text{V.69})$$

$$\mathcal{I}_7 = \sum_{k=0}^{nbNodes-1} m_k \left( \Psi_k^i \wedge \Psi_k^j \right), i = 0 \dots nbModes - 1, j = 0 \dots nbModes - 1 \quad (nbModes \times nbModes \times 3) \quad (\text{V.70})$$

The equation of motion for multibody system is subjected to constraint stemming from joints and the contact between bodies. These constraint equations ( $\mathbf{B}$ ,  $\mathbf{G}$ ) are introduced through lagrange multiplier  $\lambda$  constitute thus an algebraic system as follows:

$$\begin{cases} \mathbf{M}\ddot{\boldsymbol{\eta}} + \lambda \mathbf{B}^T = \mathbf{F} \\ \mathbf{B}\ddot{\boldsymbol{\eta}} = \mathbf{G} \end{cases} \quad (\text{V.71})$$

$\mathbf{M}$ ,  $\mathbf{B}$ ,  $\mathbf{F}$ , and  $\mathbf{G}$  can be formed from a set of known geometric variables and kinematic variable values.

$\ddot{\boldsymbol{\eta}}$  is the vector of acceleration. The Lagrange multiplier  $\lambda$  can be interpreted as constraint forces, equivalent to the amount of force needed to enforce constraint equations.

A this stage, strategies for reducing flexible bodies has to be carry out. This is reflected in finding an appropriate reduced basis  $\Psi$ . Strategies are proposed with preliminary validations in the next section.

### 3.2 Proposed reduced order models

Herein two strategies are proposed to reduce the gear pair. These strategies are based on a high fidelity model. A high fidelity model is a fine (large) finite element model solved in the physical space for which validations have been established. For gears, validations can be in terms of displacements, stresses,

static transmission error and mesh stiffness. Then, this model is used to generate the reduced space.

In this dissertation, naturally, we retained as high fidelity model the model proposed in the section 3.

This model is well adapted for the static transmission error, the mesh stiffness, the displacement field and the stress field computation. Beside, some comparison for the contact with Hertz theory promote the model.

### **3.2.1 Proper orthogonal decomposition (POD) enhanced with eigenmodes**

The objective is to build a reduced basis that contains the static and the dynamic behaviour of the gear. To this end, the reduced basis is generated in two parts. The first part represents the static behaviour and the second part focus on the dynamic behaviour.

The separation of the static and the dynamic behaviour is possible because the gear behaviour can be different between the tooth level and the gear body level. Indeed, the first natural frequency  $f_1$  of two teeth in contact is the order of  $10^5$ Hz as shown in Fig. V.8. It's even higher when considering the tooth itself. Certainly, this frequency value depends on the gear design but it appears that the tooth mode shapes are very high frequencies. For this reason, we assume in this section that the tooth itself has only quasi-static behaviour. On the contrary, gear bodies have static and dynamic behaviour which is accentuated with lightweigh gears. For instance, a thin rim with holes drops down the natural frequencies of the gear body and it affects the static deflection since the compliance is modified. An example of the first gear body mode of a thin rimmed gear with holes for the first natural frequency

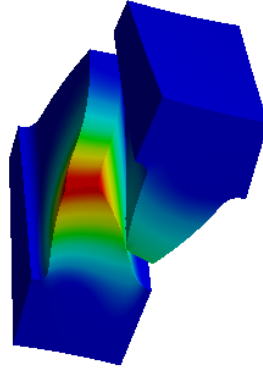


Figure V.8: Example of the first contact mode shape ( $f_1 \approx 10^5$  Hz)

$f_1 \approx 3270$  Hz is depicted in Fig. V.9. In the transportation domain, especially for automotive, the natural frequencies of lightweigh gear bodies is even much smaller, in the order of magnitude of 100 Hz. In this case, the dynamic behaviour of the gear body has to be taken into account. Another

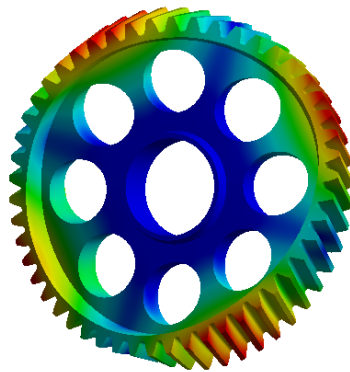


Figure V.9: Example of the gear body mode shape of a thin rimmed gear with holes ( $f_1 \approx 3270$  Hz)

complexity is to consider in the reduced basis the contact behaviour of the gear pair. This procedure for building the static part and the dynamic part of the reduced basis taking into account the contact between the gear pair is detailed below.

**Static behaviour:** the main steps to build up the static part of the reduced basis are presented.

The procedure relies on the proper orthogonal decomposition method (POD):

The high fidelity model based on a finite element analysis of the gear pair in quasi-static operating conditions is used at this stage. This finite element analysis is detailed in III.4. An output torque  $T = 115 \text{ N m}$  is applied for the gear pair considered in table III.1 and the simulation employed for the computation of the static transmission error allows the generation of the snapshots. Indeed, for the input and the output gear, the displacement fields are extracted for each position of  $\theta_1$  as displayed in Fig. V.10.

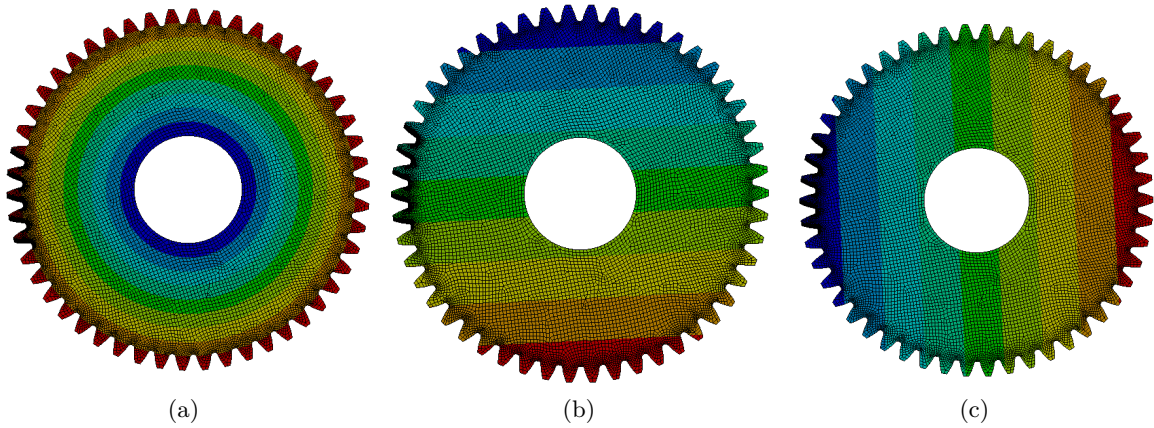


Figure V.10: Example of the displacement field at a given driving angle  $\theta_1$ . (a) total displacement, (b) displacement in x direction, displacement in y direction.

The collected snapshots include rigid body motion, and for the multibody framework, the reduced basis represents only the flexibility as explained by the equation V.51. So, the rigid body motion is removed from the snapshots using a minimization between rigid body modes and the strain tensor.

Let us consider the collection of the elastic part of the snapshots as  $\mathbf{S}$ :

$$\mathbf{S} = [\mathbf{u}(\theta_1, t_1) \in \mathbb{R}^n \quad \mathbf{u}(\theta_1, t_2) \in \mathbb{R}^n \quad \dots \quad \mathbf{u}(\theta_1, t_N) \in \mathbb{R}^n] \quad (\text{V.72})$$

where  $n$  is the number of degree of freedom and  $N$  the number of snapshots retained with  $N \ll n$ . The number of snapshots and the time/angle step used for the collection are important parameters, they directly affect the precision. Here, we have chosen a time/angle step for which the static transmission error has converged. So, the elastic field at each time/angle step is retrieved in  $\mathbf{S}$ .

As explained in 1.3.4, different approaches can be used to extract the relevant modes from  $\mathbf{S}$ ,  $\mathbf{S}\mathbf{S}^T$  and  $\mathbf{S}^T\mathbf{S}$ . Generally, the SVD is employed. Working directly on  $\mathbf{S}$  or  $\mathbf{S}\mathbf{S}^T$  is computationally demanding since the size of these matrices are  $n \times N$  and  $n \times n$ , respectively. Indeed, applying the SVD on  $\mathbf{S}$  gives:

$$SVD(\mathbf{S}) = \mathbf{Z}\mathbf{\Sigma}\mathbf{V}^T \quad (\text{V.73})$$

where  $\mathbf{Z}$  and  $\mathbf{V}$  are orthogonal matrices ( $\mathbf{Z}\mathbf{Z}^T = \mathbf{I}_n$  and  $\mathbf{V}\mathbf{V}^T = \mathbf{I}_N$ ) having respectively the dimension  $n \times n$  and  $N \times N$ .  $\mathbf{\Sigma} \in \mathbb{R}^{n \times N}$  is diagonal matrix containing the singular values which are arranged in decreasing order. Then, substituting the equation V.73 in  $\mathbf{S}\mathbf{S}^T$  it reads:

$$\mathbf{S}\mathbf{S}^T = \mathbf{Z}\mathbf{\Sigma}(\mathbf{V}^T\mathbf{V})\mathbf{\Sigma}^T\mathbf{Z}^T = \mathbf{Z}(\mathbf{\Sigma}\mathbf{\Sigma}^T)\mathbf{Z}^T = \mathbf{Z} \begin{bmatrix} \text{diag}(\sigma_p^2) & 0 \\ 0 & 0 \end{bmatrix} \mathbf{Z}^T, \quad (n \times n) \quad (\text{V.74})$$

where the subscript  $p$  is the number of nonzero singular values.

Similarly with  $\mathbf{S}^T\mathbf{S}$ , we obtain:

$$\mathbf{S}^T\mathbf{S} = \mathbf{V}\mathbf{\Sigma}^T(\mathbf{Z}^T\mathbf{Z})\mathbf{\Sigma}\mathbf{V}^T = \mathbf{V}(\mathbf{\Sigma}^T\mathbf{\Sigma})\mathbf{V}^T = \mathbf{V}\text{diag}(\sigma_p^2)\mathbf{V}^T, \quad (N \times N) \quad (\text{V.75})$$

The nonzero singular values of  $\mathbf{S}\mathbf{S}^T$  are also considered in  $\mathbf{S}^T\mathbf{S}$ . We thus apply the SVD on the matrix

$\mathbf{S}^T \mathbf{S}$  of size  $N \times N$  instead of  $\mathbf{S} \mathbf{S}^T$  to build the POD modes  $\mathbf{\Upsilon}$  also called POMs. The SVD gives:

$$SVD(\mathbf{S}^T \mathbf{S}) = \mathbf{V} \mathbf{diag}(\sigma_p^2) \mathbf{V}^T \quad (\text{V.76})$$

then, let's consider  $\mathbf{u}(\theta_1, t_i)$  the snapshot number  $i$  as  $\mathbf{u}_i$  to simplify the formula of the POMs which are expressed for  $m$  snapshots as follows:

$$\mathbf{\Upsilon}_p = \frac{1}{\sqrt{\lambda_p}} \sum_{i=0}^n (\mathbf{V}^p)_i \mathbf{u}_i \quad (\text{V.77})$$

where  $\lambda_p = \sigma_p^2$ . Thus, the equation [V.77](#) defines the POMs generated by the POD method. Firstly, the auto-correlation matrix  $\mathbf{S}^T \mathbf{S}$  is computed for snapshots over two mesh periods to make us confident that the entire static behaviour of the gear contact is captured. We can identify clearly in the [Fig. V.11a](#) the periodicity of the system. This picture ([Fig. V.11a](#)) is for the displacement field of the output gear but the same behaviour is obtained for the driving gear. Moreover, the number of modes  $r$  of  $\mathbf{\Upsilon}_p$  to keep for the analysis is important for the precision and efficiency of the reduced basis. Error estimator can be used to know how many mode to keep, they can be based on the residual or even the energy. Here, we decide to consider the modal energy for each POMs (see [V.78](#)) to truncate the reduced basis. This criteria is well adapted for mechanical problems where the behaviour is driven by the strain energy. The criteria is thus for the mode  $i$ :

$$\mathcal{E}_i = \frac{\lambda_i}{\sum_k \lambda_k} \quad (\text{V.78})$$

With  $\lambda_i = \sigma_i^2$  the eigenvalue of the mode  $i$ . The POMs modal energies are displayed in [Fig. V.11b](#).

We can see that the modal energy decrease rapidly. It means that only some vectors of  $\mathbf{\Upsilon}_p$  are

required to capture the static behaviour of the contacting gears. The number of POMs retained  $r$  is for  $\sum_i^r \mathcal{E}_i \geq 0.99$ . Generally in the literature, for the POD method, 99% of the energy is sufficient to capture the entire behaviour of the snapshot data. The first five resulting POMs that represents the

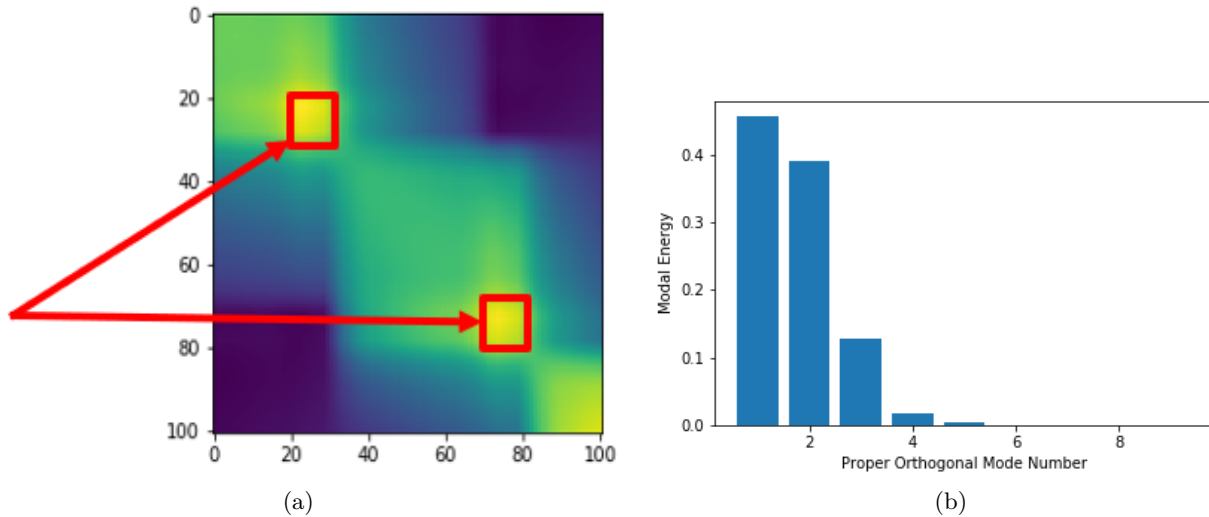


Figure V.11: (a) Auto-correlation matrix representation of 100 snapshots (b) POMs energy chart for the output gear.

static behaviour are presented in Fig. V.12. We can see that the POMs 1, 2 and 3 feature mostly the tooth bending i.e. the global deformation of the tooth. The deformation of the adjacent teeth is also taken into account. The POMs 4 and 5 reflect local tooth deformation which is hertzian-like deformation induced by the contact between the gear teeth. The shape of these POMs patterns make us confident to catch the static behaviour of the mating gear teeth. The strategy for the generation of the POMs is summarized in Fig. V.13. **Dynamic behaviour:** The use of the POD method on the high fidelity model enables us to provide robust static modes. These POMs capture the global and local deformation at the tooth level. We thus address the static behaviour of the gear pair but to consider also the dynamic behaviour, the POD reduced basis must be enhanced. We decide to enhance

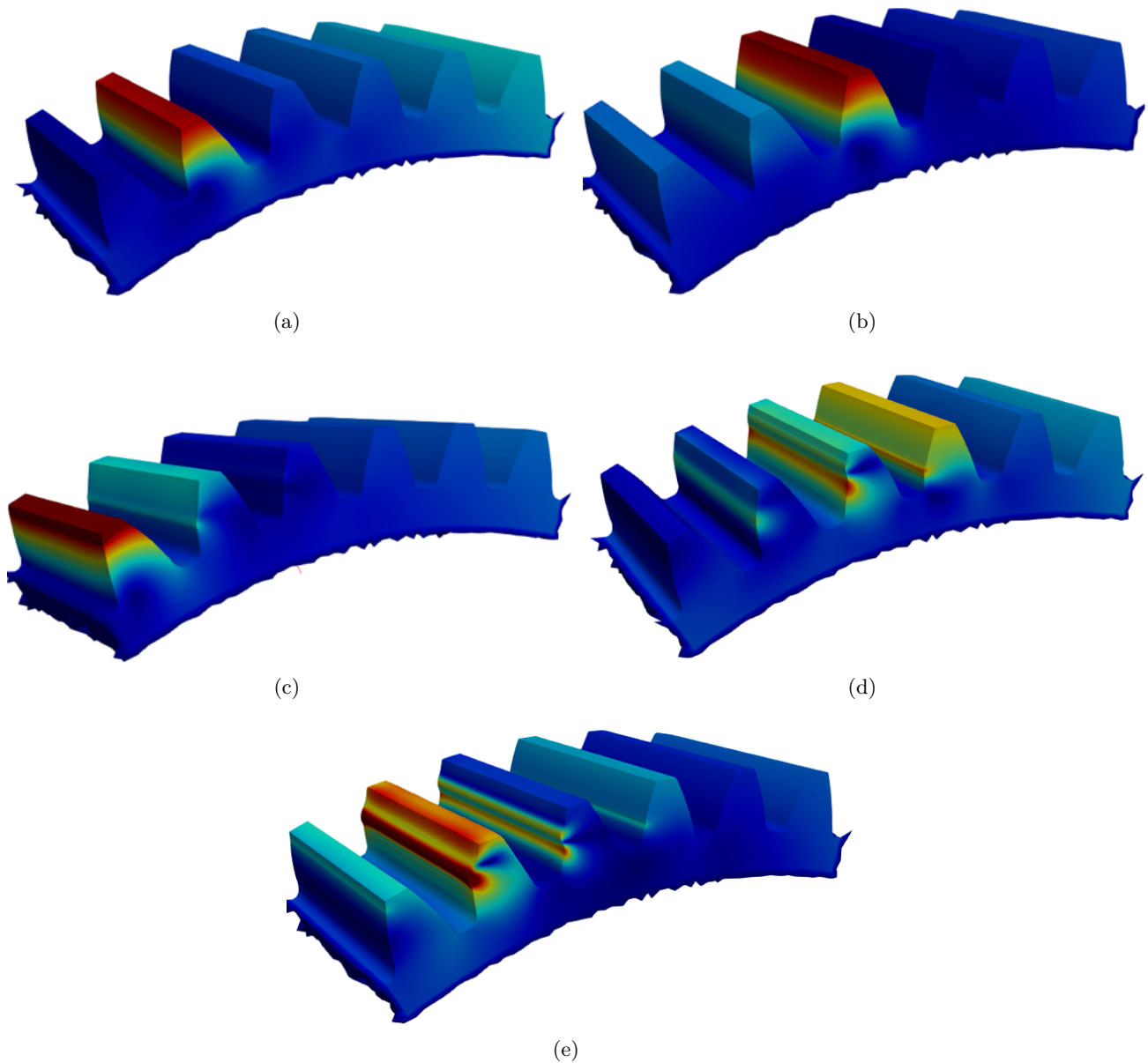


Figure V.12: Example of the first five POMs. (a) POMs 1, (b) POMs 2, (c) POMs 3, (d) POMs 4 and (e) POMs 5.

the POMs with the eigenmodes  $\Phi$ . These eigenmodes are obtained by performing a modal analysis of each gear (input and output gear). In practice, the equation V.10 is solved for a range from 0 Hz to 20000 Hz. An example of these eigenmodes are displayed in Fig. V.14 The strategy proposed in this section for building the reduced basis relies on the POD method enhanced with eigenmodes. So, the

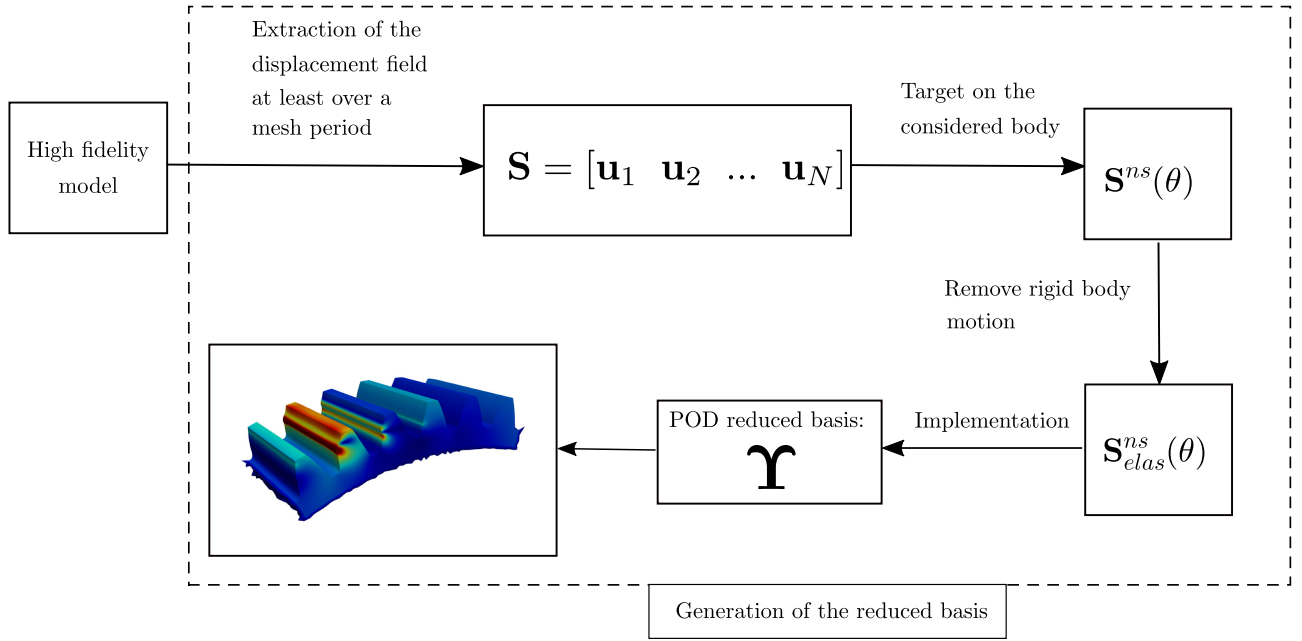


Figure V.13: Summary of the strategy for the POD method.

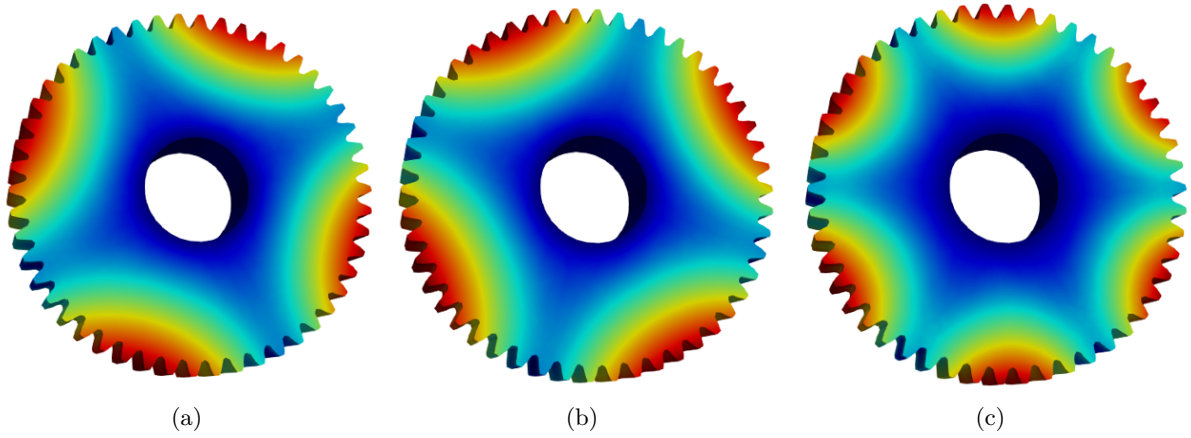


Figure V.14: Example of eigenmodes.

reduced basis  $\Psi$  can be expressed as the concatenation of POMs and eigenmodes:

$$\Psi = [\Upsilon \ \Phi] \quad (\text{V.79})$$

The next section proposed another strategy based on Krylov subspace to build the reduced basis.

### 3.2.2 Krylov subspace based on the Two level Orthogonal ARnoldi algorithm (TOAR)

The objective of this section is to propose another strategy for building a reduced basis that describes the gear dynamical problem. Unlike the previous method, the static and the dynamic behaviour is not separated during the generation of the reduced basis. Hereafter, the strategy relies on the use of Krylov subspaces to build the static and the dynamic behaviour of the gear pair. To this end, an original approach is proposed. The original strategy derives the reduced basis using a high fidelity model. The quasi-static model III.4 which is used for the previous section is also retained for the Krylov method.

Krylov subspaces are generated according to external forces as shown in the definition of the subspaces V.22, the term  $\mathbf{R}_0$  is the induced deflection. These subspaces have never been adapted for contact problems. The reason is the treatment of contact forces which are not considered during the generation of Krylov subspaces. In this dissertation, we propose to generate the Krylov subspaces by introducing the contact forces computed with the quasi-static model. These contact forces are the result of solving the Signorini conditions (III.18) with the augmented lagrangian formalism. In practice, considering contact forces in Krylov subspaces it's equivalent to consider the gear pair as two bodies excited by the contact forces. The term  $\mathbf{R}_0 = -\mathbf{K}^{-1}\mathbf{F}_{ext}$  becomes  $\mathbf{R}_0 = -\mathbf{K}^{-1}\mathbf{F}_n$  where  $\mathbf{F}_n$  are the space varying contact forces. This is the main originality of the proposed strategy. The procedure is explained in detail below.

The high fidelity model based on a quasi-static modelling III.4 is used at this stage. This is finite element analysis of the gear pair operating in quasi-static operating conditions. An output torque  $T = 115 \text{ N m}$  is applied for the gear pair considered in table III.1 and the simulation employed for the computation of the static transmission error allows the generation of the snapshots. As opposed to the POD method, the field of contact forces are extracted for each position of  $\theta_1$  as displayed in Fig.

V.15 instead of the displacement field. The collection of the contact forces are stored as  $\mathcal{F}$ :



Figure V.15: Example of the field of contact forces for a given position of the driving gear (a) and another position (b)

$$\mathcal{F} = [\mathbf{F}_n(\theta_1, t_1) \in \mathbb{R}^n \quad \mathbf{F}_n(\theta_1, t_2) \in \mathbb{R}^n \quad \dots \quad \mathbf{F}_n(\theta_1, t_N) \in \mathbb{R}^n] \quad (\text{V.80})$$

The Fig. V.16 display the auto-correlation matrix of the contact forces  $\mathcal{F}$  which is  $\mathcal{F}^T \mathcal{F}$ . We can identify clearly the periodicity in the contact forces. At this stage, the generation of the Krylov subspaces must take into account the variation of the field of contact forces over a mesh period at

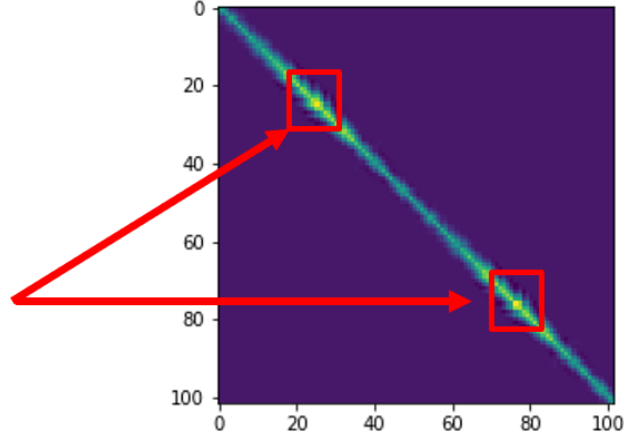


Figure V.16: Auto-correlation matrix representation for the contact forces.

least. And Krylov subspaces are built by considering one field of the input forces, here it has to be a serie of fields of the contact forces over a mesh period. For this reason, we must consider as many subspaces as many field of contact forces we have. The set of Krylov subspace as described in V.22 is modified as follows:

$$\mathcal{K}_r(\mathbf{A}_1, \mathbf{A}_2, \mathbf{R}_0^i) = \left\{ \mathbf{R}_0^i, \mathbf{R}_1^i, \dots, \mathbf{R}_{r-1}^i \right\} \quad (\text{V.81})$$

$$\text{for } p \geq 1, \mathbf{R}_p^i = \mathbf{A}_1 \mathbf{R}_{p-1}^i + \mathbf{A}_2 \mathbf{R}_{p-2}^i$$

$$\mathbf{A}_1 = -\mathbf{K}^{-1} \mathbf{C},$$

$$\mathbf{A}_2 = -\mathbf{K}^{-1} \mathbf{M},$$

$$\mathbf{R}_0^i = -\mathbf{K}^{-1} \mathbf{F}_n^i$$

$$\mathbf{R}_1^i = \mathbf{A}_1 \mathbf{R}_0^i$$

where the subscript  $i$  states for the contact force considered  $\mathbf{F}_n(\theta_1, t_i)$  and  $r$  is the order of the subspace.

The concatenation of the successive Krylov subspaces becomes:

$$\mathcal{T}_m(\mathbf{A}_1, \mathbf{A}_2, \mathbf{R}_0^1, \mathbf{R}_0^2, \dots, \mathbf{R}_0^m) = \left\{ \mathcal{K}_r(\mathbf{A}_1, \mathbf{A}_2, \mathbf{R}_0^i), \text{ for } i \in [1, m] \right\} \quad (\text{V.82})$$

with  $m$  the number of snapshot to be considered in  $\mathcal{F}$ . So, the size of the concatenation of Krylov subspaces  $\mathcal{T}_m$  is  $m \times r$ . The Krylov subspaces considered here are derived for an expansion point  $s_0 = 0$  in order to catch the static behaviour and the order  $r$  will be responsible for the good approximation of the dynamic behaviour. Here we perform a convergence study of frequency responses from 0Hz to 20000Hz by exciting the gear with some contact forces in  $\mathcal{F}$ . This enables us to choose  $r = 4$ .

At this stage, we have build  $\mathcal{T}_m$  which is a concatenation of Krylov subspaces taking into account the current contact forces. To extract an efficient basis from  $\mathcal{T}_m$  we will use an SVD procedure. We obtain thus the final Krylov reduced basis. The strategy for the generation of the Krylov subspaces is summarized in Fig. [V.17](#).

### 3.3 Integration of the equations of motions for nonsmooth mechanics

The simulation of the dynamics of multibody systems must be carried out with care. Mainly because of complexity to take into account the joints, using constraints and subjected to multiple contact (bilateral and unilateral). Choosing the right integration scheme is key to achieve a solution. This section discusses the advantages and drawbacks of the time integration methods commonly used for the computation of the dynamics of multibody systems. For our gear problem, a particular attention to the treatment of nonsmooth events induced by the contact is fulfilled. There are two major techniques

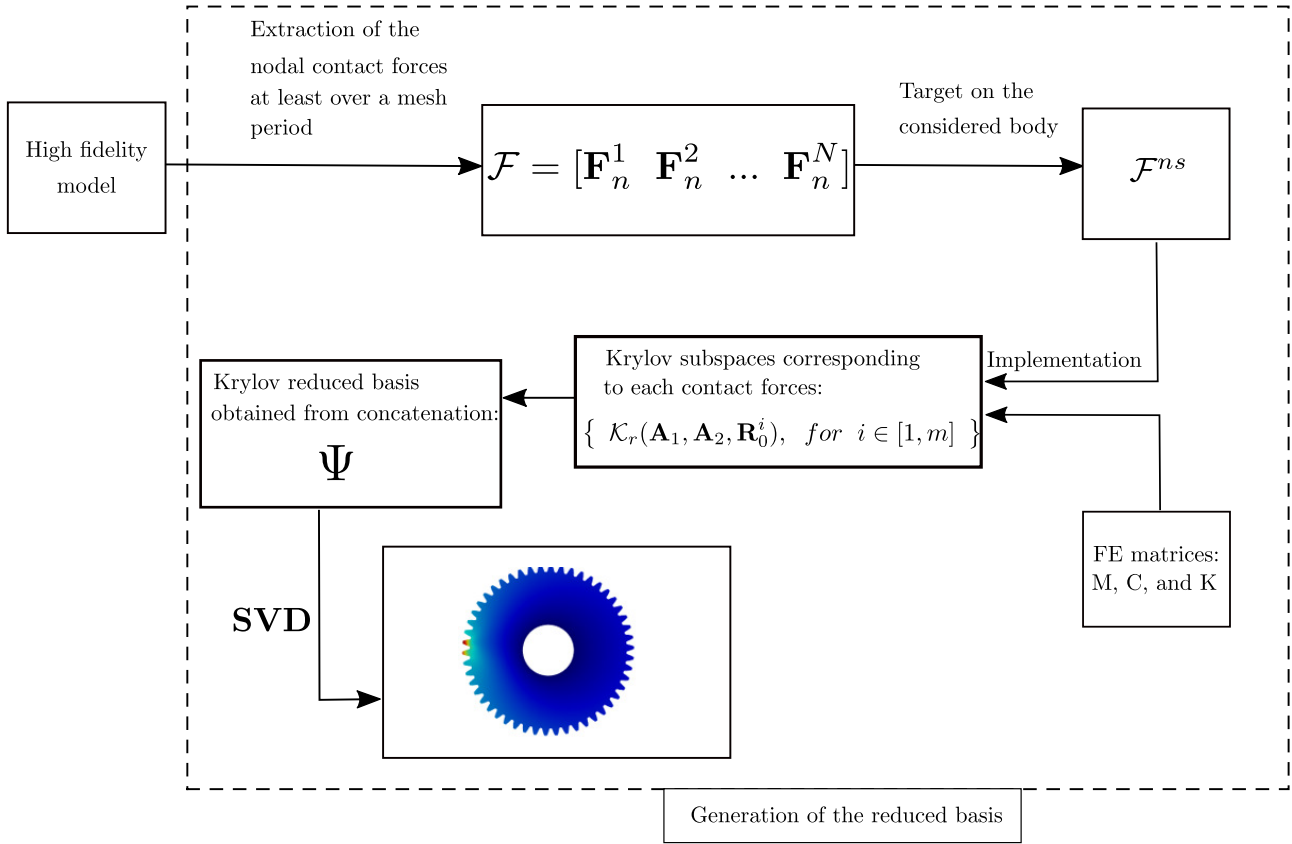


Figure V.17: Summary of the strategy for the krylov subspaces.

for the simulation of the dynamics of multibody systems subjected to non-smooth events such as impacts, **event-driven schemes and time-stepping schemes**. The description of these schemes will drive our following choice for the solve of the gear dynamics.

### 3.3.1 Event-driven schemes

The event-driven schemes treat the nonsmooth dynamics (at discrete time) and the smooth dynamics separately [2, 3, 110]. For instance, the detection of an impact is considered as an event. This is the main step to be achieved since the time step of events must be defined very precisely to maintain the order of the consistency of the method. The smooth dynamics occurs between two successive events, it's described by DAE and it can be integrated with classical numerical scheme [58, 59]. The

energy redistribution associated to the event - a shock for example - is computed and then a new smooth step starts. The main drawback of the event-driven schemes is the difficulties of handling finite accumulations of impacts. Indeed, when many events occur in a very short time interval, the simulation becomes slow because every single event has to be handled within the event-driven strategy.

### 3.3.2 Time-stepping schemes

The time-stepping schemes use a formulation of the dynamics that enables to simultaneously handle the nonsmooth dynamics and the smooth dynamics [68, 69, 70, 71, 72, 73, 74]. For this reason, we have chosen to use the time-stepping schemes and particularly the Moreau-Jean method. The main idea of this scheme is to formulate the smooth dynamics as a **differential inclusion** [3, 68, 72] considering unilateral constraints as:

$$\begin{cases} \dot{\boldsymbol{\eta}} = \mathbf{v} \\ \mathbf{M} \frac{d\mathbf{v}}{dt} = \mathbf{F} + d\mathbf{i} \\ \mathbf{0} \leq \boldsymbol{\eta} \perp d\mathbf{i} \geq \mathbf{0} \end{cases} \quad (\text{V.83})$$

where  $d\mathbf{i}$  is the **reaction measure**.

### 3.3.3 Moreau-Jean time-stepping method

In the Moreau-Jean method, the unilateral contact is modeled with a Signorini condition at the velocity level, that is a complementarity between the contact impulse and the relative velocity, which ensures the impenetrability. In order to handle several contacts, with possibly changing status, an implicit algorithm is chosen to integrate the dynamics. For the simplicity, let's consider the equation V.83 with  $\mathbf{F} = -\mathbf{C}\dot{\boldsymbol{\eta}} - \mathbf{K}\boldsymbol{\eta}$  and  $\mathbf{M}(g) = \mathbf{M}$ . The discrete form of the equation of motion over the interval

$]t_i, t_{i+1}]$  with  $h = t_{i+1} - t_i > 0$  yields:

$$\begin{cases} \boldsymbol{\eta}(t_{i+1}) = \boldsymbol{\eta}(t_i) + \int_{]t_i, t_{i+1}] } \mathbf{v}^+ dt \\ \mathbf{M}(\mathbf{v}^+(t_{i+1}) - \mathbf{v}^+(t_i)) = \int_{t_i}^{t_{i+1}} (-\mathbf{C}\mathbf{v} - \mathbf{K}\boldsymbol{\eta} + \mathbf{F}_{ext})dt + \int_{]t_i, t_{i+1}] } \mathbf{d}\mathbf{i} \end{cases} \quad (\text{V.84})$$

The smooth terms can be discretized using a  $\theta$ -method [41, 44] as follows:

$$\begin{cases} \boldsymbol{\eta}(t_{i+1}) = \boldsymbol{\eta}(t_i) + h[\theta\mathbf{v}_{i+1} + (1 + \theta)\mathbf{v}_i] \\ \int_{t_i}^{t_{i+1}} (-\mathbf{C}\mathbf{v} - \mathbf{K}\boldsymbol{\eta})dt = h[\theta(\mathbf{C}\mathbf{v}_{i+1} + \mathbf{K}\boldsymbol{\eta}_{i+1}) + (1 - \theta)(\mathbf{C}\mathbf{v}_i + \mathbf{K}\boldsymbol{\eta}_i)] \\ \int_{t_i}^{t_{i+1}} \mathbf{F}_{ext}dt = h[\theta\mathbf{F}_{ext, i+1} + (1 + \theta)\mathbf{F}_{ext, i}] \end{cases} \quad (\text{V.85})$$

The equations become:

$$\begin{cases} \boldsymbol{\eta}(t_{i+1}) = \boldsymbol{\eta}(t_i) + h[\theta\mathbf{v}_{i+1} + (1 + \theta)\mathbf{v}_i] \\ \hat{\mathbf{M}} = \mathbf{M} + h\theta\mathbf{C} + h^2\theta^2\mathbf{K} \\ \mathbf{v}_{free} = \mathbf{v}_i + \hat{\mathbf{M}}^{-1}[-h\mathbf{C}\mathbf{v}_i - h\mathbf{K}\boldsymbol{\eta}_i - h^2\theta\mathbf{K}\mathbf{v}_i + h[\theta\mathbf{F}_{ext, i+1} + (1 + \theta)\mathbf{F}_{ext, i}]] \\ \mathbf{v}_{i+1} = \mathbf{v}_{free} + \hat{\mathbf{M}}^{-1}\mathbf{p}_{i+1} \end{cases} \quad (\text{V.86})$$

with  $\mathbf{p}_{i+1} \approx \int_{]t_i, t_{i+1}] } \mathbf{d}\mathbf{i}$  is the approximation of the impulse over the time step. We can notice that the

acceleration of the system is never explicitly computed because it becomes infinite for impulsive forces.

Moreover, a Newton impact law relating the pre- and post-impact velocities,  $\mathbf{v}^i$  and  $\mathbf{v}^{i+1}$  respectively,

through a restitution coefficient  $e \in [0, 1]$  might be required for the uniqueness of the solution. It can

be expressed by:

$$\mathbf{v}^{i+1} = -e\mathbf{v}^i \quad (\text{V.87})$$

For each contact node of the system, this law is implicitly introduced in the previous equations. It's

represented by:

$$\begin{cases} d_{i+1} \leq 0 \Rightarrow 0 \leq v_{i+1} + ev_i \perp p_{i+1} \geq 0 \\ d_{i+1} > 0 \Rightarrow p_{i+1} = 0 \end{cases} \quad (\text{V.88})$$

where  $d_{i+1}$  is the gap between two contact nodes at  $t_{i+1}$ .

For our gear problem, we will use time-stepping scheme and particularly, the Moreau-Jean method.

This approach is faster than event driven schemes when several events have to be considered. The main weakness of the Moreau-Jean method is that Signorini conditions are written at velocity level and it requires a small time step to avoid penetration during the contact phase.

The next section presents the use of the Moreau-Jean method coupled to model order reduction in order to compute the dynamic transmission error. Additionally, in this section, we pay attention to the modelling for handling the contact and the periodicity of the gear.

### **3.4 Proposed strategy for the contact**

The generation of the reduced basis is achieved using the high fidelity model. This model uses the periodicity of the gear (mesh periodicity) to refine the mesh only on 4 teeth for the driving and the output gear. These teeth are possibly in contact during the simulation over 2 mesh period. We obtain a reduced basis for which the validity is on this mesh period. However, the full transient simulation will cover multiple revolutions of the wheel. For this purpose, we introduce the following strategy: for a gear pair, we will consider a fictitious gear pair which is used for performing the true revolutions, this means this fictitious gear pair is operating over a rotation of  $2k\pi$ . Whereas the real gear pair for which the reduced basis has been generated is operating only over 2 mesh periods (this is the angular

position where the mesh is refined). This fictitious gear pair is linked with the "real" gear pair by constraint relation. So, in practice, two gear pairs (fictitious and real) are used as shown in Fig. V.20. At the solver level, we use the "real" gear pair and we apply a modulo on the driving and output angles,  $\theta_1$  and  $\theta_2$  respectively. This enables us to use the reduced basis always in the mesh area where the validity must be achieved. So, we apply on  $\theta_1$  and  $\theta_2$ :

$$\theta_{1,2} \equiv 0 \pmod{\frac{2k\pi}{Z}} \quad (\text{V.89})$$

with  $Z \in \mathbb{N}$ .

The fictitious gear pair is considered in the simulation for the contact detection phase and for the visualization. To accelerate the contact detection phase, we make the assumption that the contact can be determined on the undeformed mesh. This allows us to obtain the contact point location rapidly assuming small deformations. Then, the flexible velocities must be computed for all contact points using the equation V.57 in order to form the generalized forces. At this stage, since we use surface-to-surface detection instead of node-to-node detection for better precision as explained in III.3.1, the reduced basis which represents nodal quantities has to be interpolated at the contact point (see Fig. V.18). The Radial Basis Function (RBF) is retained to perform this interpolation because it allows also to extrapolate points.

After the computation of the flexible velocities, the contact force is determined by solving the Signorini

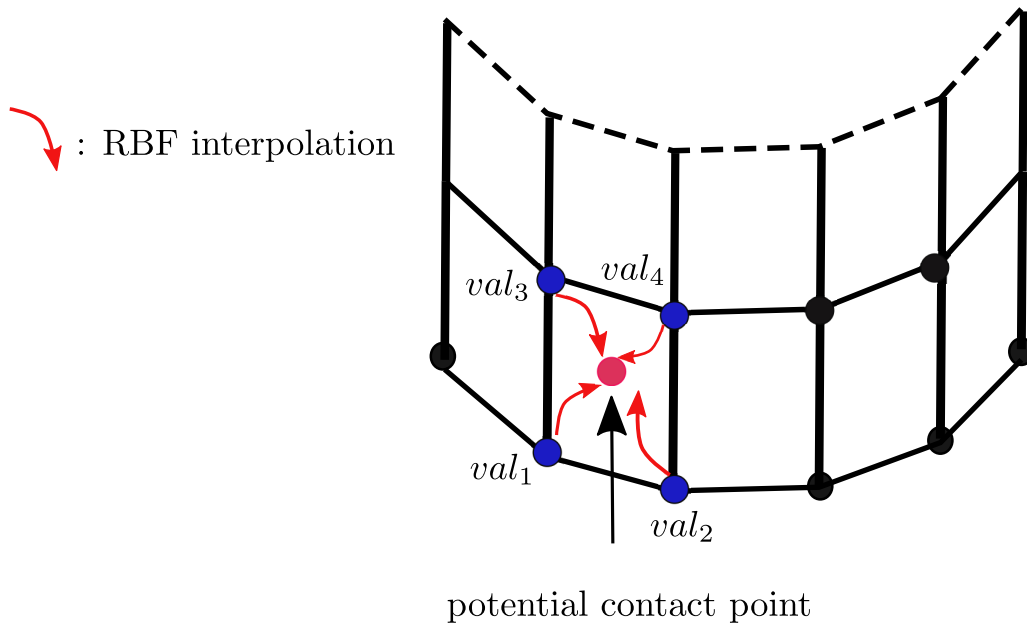


Figure V.18: Schematic representation of the RBF interpolation of the reduced basis at the contact points.

conditions at the velocity level (see eq. V.88) during the time integration.

### 3.4.1 Numerical application

In this section preliminary results are presented. The results are obtained by considering the following process: firstly, the high fidelity model for the gear pair is established. From this model, the reduced basis based on the POD enhanced with eigenmodes is derived. This reduced basis is used to approximate the flexible behaviour of the gear. Additionally, the equation of motion using a multibody framework are used. At this time, the Moreau-Jean time stepping method is considered for the integration of the equation of motion. Finally, the periodicity of the system is considered using a fictitious gear pair and when a contact occurs, the RBF interpolation is applied to interpolate the reduced basis at the contact point location. The Fig. V.19 summarized the complete procedure which is applied. The dynamical model is displayed in Fig. V.20. The Fig. V.21 compares the STE obtained

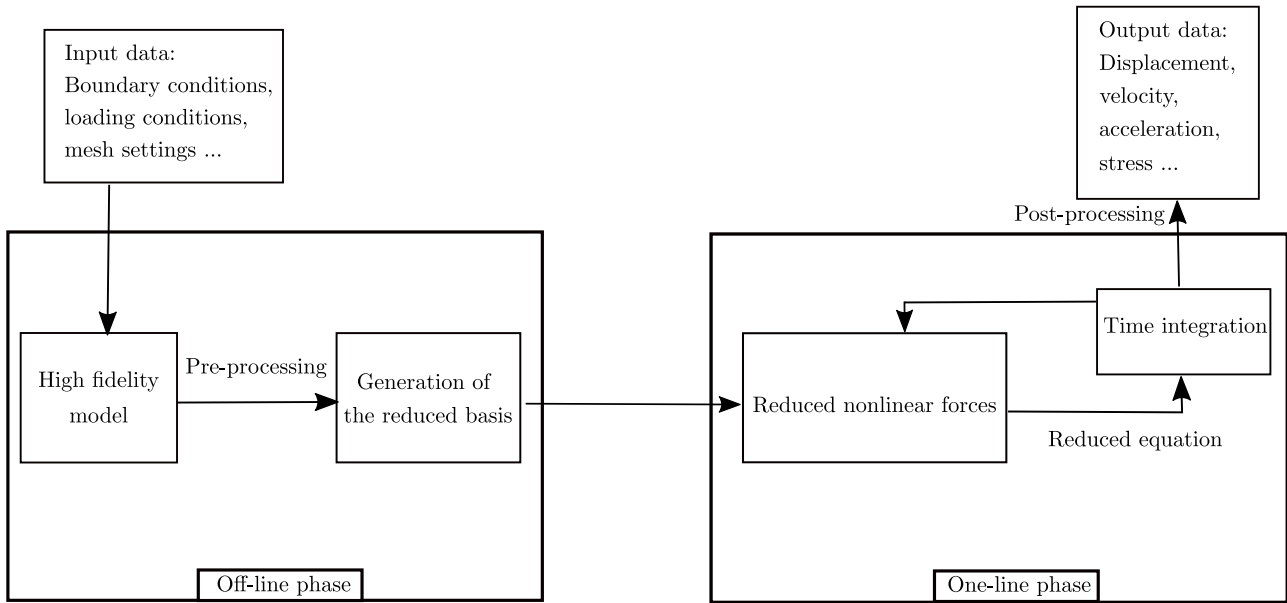


Figure V.19: Summary of the complete procedure.

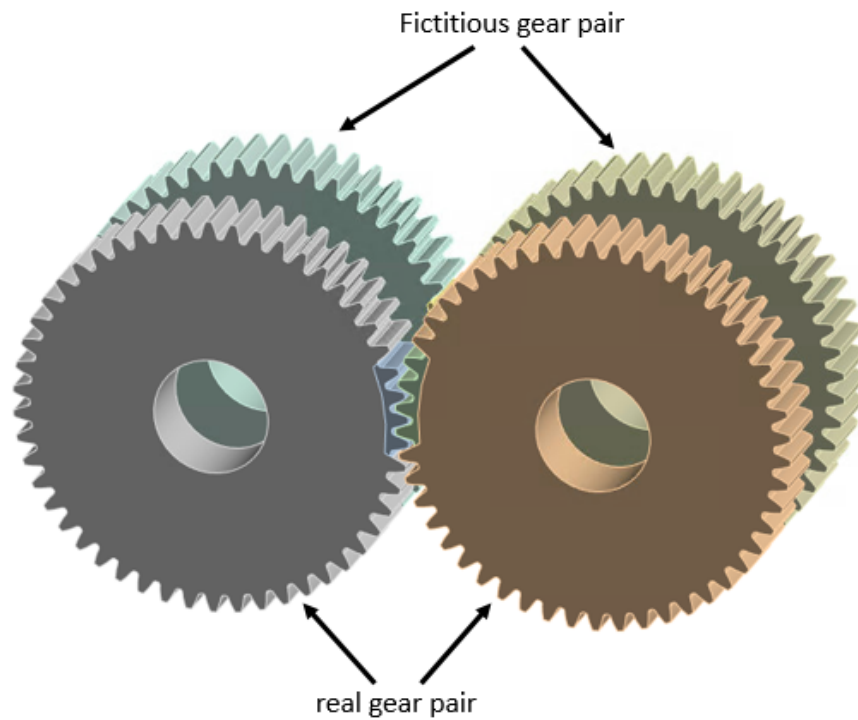


Figure V.20: Dynamical gear pair model with the fictitious body.

from the high fidelity model and the reduced model. The curves match well, the amplitude of the fluctuation are well described and the micro-geometry is well characterized. The reduced model is also

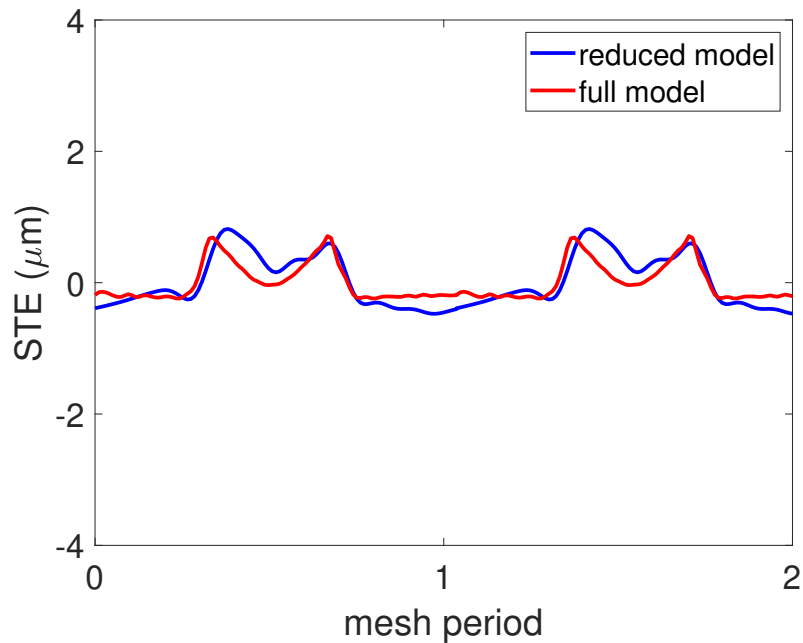


Figure V.21: Comparison of the fluctuation of the static transmission error of the POD reduced model (—) and the full model (—).

used to compute the dynamic transmission error for an input velocity of 1500 rpm. The Fig. V.22 shows the transient phase until  $\theta_1 = 0.2 \text{ rad}$  and then two periods of the dynamic transmission error are visible.

## 4 Conclusion

This chapter provides an insight of model order reduction techniques in the field of structural dynamics, with emphasis on gear contact dynamics. From this observation, two strategies are considered.

The first strategy is based on the modelling of complete gearboxes by introducing the STE and the mesh stiffness fluctuations as internal excitations. Then, the flexible shafts, bearing and housing are condensed using the CMS method and the resolution is performed in the frequency domain using the HBM method. The static transmission error and the mesh stiffness fluctuations were computed while

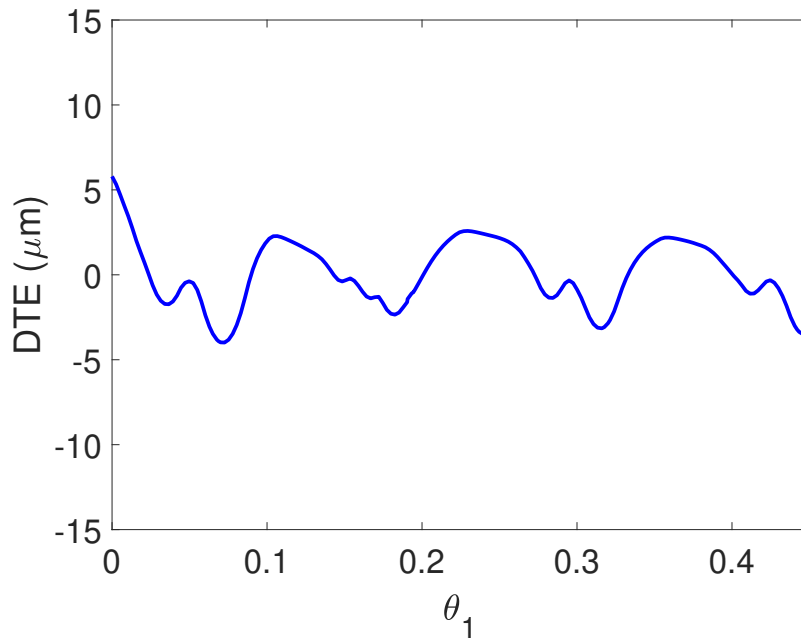


Figure V.22: Fluctuation of the dynamic transmission error for the POD reduced model.

considering the flexible contribution of the entire gearbox. Results show the importance of considering the entire flexibility of the gearboxes. Indeed, the critical frequency of the primary resonance of the long gearbox is two time lower than the one of the short gearbox. Also, The ratio  $A_{SD}$  of the long gearbox is higher than the one of the short gearbox (about one micrometer).

The second strategy considers a high fidelity model for building reduced bases. Two reduced bases are generated, One using the Proper Orthogonal Decomposition (POD) method enhanced with eigenmodes, the other one uses Krylov subspaces. For the sake of time, preliminary results are proposed for the POD enhanced with eigenmodes. Firstly, the obtained static transmission error is validated with the high fidelity model and then the dynamic transmission error is computed for an input velocity of 1500 rpm. Results are obtained for a gear pair and a FE-based contact is considered. The elapsed

computing time is 30 minutes. The method is thus promising.



# VI

### 1 Conclusion

This dissertation summarized the work during the Phd in collaboration between the Laboratory of Tribology and System Dynamics (LTDS, <http://ltds.ec-lyon.fr/spip/>) and the publisher of numerical simulation software ANSYS (<http://www.ansys.fr/>). The main objective of this thesis was to develop methodologies and models for the simulation of gear dynamics. For this purpose, many strategies have been followed:

As opposed to what we can find in the literature, the gear geometry that we have considered in this work was generated with high precision using NURBS with high number of control points. Besides, an accuracy of 1 micrometer in the involute profile were achieved. This high order characterization of the gear geometry generation allows thus the introduction of micro-geometric modifications directly in the involute tooth profile.

Then, a fully FE methodology was proposed to compute the internal excitations (static transmission error and mesh stiffness fluctuations). This methodology relies on a FE-based contact using an augmented lagrangian method for the solve while considering a quasi-static behavior of the gear pair.

Results were compared to results obtained with classical strategies and we have shown differences in the mean and peak-to-peak values of the STE and mesh stiffness. In addition, we demonstrate the possibility to deal with thin rimmed gear with holes. Knowing that holed gear blanks are rarely considered in state of the art techniques during the computation of the STE and the mesh stiffness, which is due to the complexity in the implementation to integrate the holed gear blank stiffness variation in classical approaches. Similarly, the proposed methodology was properly applied to complete gearboxes (gears, shafts, bearings and the housing) which is never the case in the literature. Moreover, to accelerate the simulation of gears with holed blanks, we derive in 2D a decomposition method which is based on the separation of the gear blank deformation and the tooth deformation. The approach has been successfully applied for parametric studies in terms of number and radial position of holes in the gear blanks.

Furthermore, reduced order models have been proposed to predict gear dynamic responses:

The first approach was to model complete gearboxes. The strategy relies on a condensed model of the shafts, bearings, and the housing whereas the gear pair is modelled by lumped inertia. The internal excitations of the STE and the mesh stiffness were considered in the model. The global approach is widely spread in the literature, the main difference is in the way to compute the STE and the mesh stiffness. Indeed, here we have computed the STE and mesh stiffness while considering the contribution of all the component of the gearbox which is not something performed in the literature. We have had consider in real time the misalignment induced by flexible shafts.

The second approach is based on the use of reduced order models in a multibody dynamic framework. Reduced order models are obtained from a high (FE) fidelity model. Indeed, the proper orthogonal

decomposition (POD) is applied to the displacement field over the time. This POD method captures vectors which represent contact patterns. Then, these vectors are enhanced using free mode shapes in order to add the global dynamic behaviour of the gear pair. As opposed to the literature approaches, the obtained reduced basis allows the achievement of a fully FE-based contact in dynamic operating conditions. Additionally, to accelerate the simulation, the contact detection is performed on the undeformed mesh and then the flexible contact forces are projecting the reduced space. Results for low input velocity match well with results obtained from the high fidelity model in terms of static transmission error. Dynamic transmission error is also provided with the method. In the same vein, Krylov subspaces have been generated using the field of contact forces over the time from the high fidelity model but unfortunately for the sake of time, the obtained reduced basis has not been applied.

## 2 Perspectives

The work provided in this dissertation arises new ideas and insights for further research opportunities. It would be interested to assess the obtained reduced basis based on Krylov subspaces. Indeed, a comparison with the POD method will enable the selection of the most convenient approach. it would also be interesting to improve the understanding and the quality of noise prediction, by leading complete analyses of gearboxes in transient dynamic operating conditions. For instance, the quasi-static simulations used to compute static transmission error of gearboxes can be considered to generate POD and Krylov reduced basis in dynamic operating conditions. Thus, the same workflow used for the gear pair is applicable.

Furthermore, the 2D quasi-static decomposition method should be enhanced to 3D in order to introduce thin rim with holes in the gear blank. For this, 3D field of displacement with potential motion out of the tooth plane has to be considered at the interface between the holed gear blank and the teeth. The addition of this enhancement will enable fast handling of complex holed gear blank.

One of the main perspective of this work is also the experimental validation of the proposed models.

Methods proposed in this dissertation can be directly applied to industrial cases and therefore it would be interested to confront results with experimental data.

Finally, the proposed methods should be integrated for commercialization in the software ANSYS.

## Bibliography

---

- [1] A variable order runge-kutta method for initial value problems with rapidly varying right-hand sides. 16,p.201-222.
- [2] M. Abadie. Dynamic simulation of rigid bodies: Modelling of frictional contact. *In B. Brogliato, Impacts in Mechanical Systems, volume 551 of Lecture Notes in Physics, Springer*, pages 61–144, 2000.
- [3] V. Acary and B. Brogliato. Numerical methods for nonsmooth dynamical systems: Applications in mechanics and electronics. *volume 35 of Lecture Notes in Applied and Computational Mechanics. Springer Verlag*, 2008.
- [4] A. Al-shyyab and A. Kahraman. Non-linear dynamic analysis of a multi-mesh gear train using multi-term harmonic balance method : period-one motions. *Journal of Sound and Vibration*, 284(1-2),151–172,, 2005.
- [5] A. Al-shyyab and A. Kahraman. Non-linear dynamic analysis of a multi-mesh gear train using multi-term harmonic balance method : sub-harmonic motions. *Journal of Sound and Vibration*, 279(1-2),417–451,, 2005.
- [6] A. Ammar, B. Mokdad, F. Chinesta, and R. Keunings. A new family of solvers for some classes of multidimensional partial differential equations encountered in kinetic theory modeling of complex fluids. *Journal of non-Newtonian fluid Mechanics*, 39(3):153–176, 2006.
- [7] A. Andersson and L. Vedmar. A dynamic model to determine vibrations in involute helical gears. *Journal of Sound and Vibration*, 260(2):195–212, February 2003.

- 
- [8] A.C. Antoulas. Approximation of large-scale dynamical systems. *Rice University, Houston, Texas*, 2005.
- [9] M. H. Arafa and M. M. Megahed. Evaluation of spur gear mesh compliance using the finite element method. *Proceedings of the Institution of Mechanical Engineers, Part C: Journal of Mechanical Engineering Science*, 213(6), 569-579, 1999.
- [10] P. Avery, C. Farhat, and G. Reese. Fast frequency sweep computations using a multipoint padbased reconstruction method and an efficient iterative solver. *International Journal for Numerical Methods in Engineering*, 69(13), 2848-2875, 2007.
- [11] Z. Bai. Krylov subspace techniques for reduced-order modeling of large-scale dynamical systems. *Applied numerical mathematics.*, 2002.
- [12] Z. Bai and Y. Su. A second-order arnoldi method for the solution of the quadratic eigenvalue problems. *SIAM Journal on Matrix Analysis and Applications.*, 2005.
- [13] C. Beattie and S. Gugercin. Interpolatory projection methods for structure preserving model reduction. *Systems Control Letters*, 58(3), 225-232, 2009.
- [14] B. Besselink, U. Tabak, A. Lutowska, N. Van de Wouw, H; Nijmeijer, D.J. Rixen, M.E. Hochstenbach, and W.H.A Schilders. A comparison of model reduction techniques from structural dynamics, numerical mathematics and systems and control. *Journal of Sound and Vibration*, 332(19):4403–4422, 2013.
- [15] B. Blockmans, T. Tamarozzi, F. Naets, and W. Desmet. A nonlinear parametric model reduction method for efficient gear contact simulations. *INTERNATIONAL JOURNAL FOR NUMERICAL METHODS IN ENGINEERING*, 2014.
- [16] V. Buljak. Inverse analyses with model reduction: proper orthogonal decomposition in structural mechanics. *Springer Science Business Media*, 2011.

- 
- [17] Y. Cai. Simulation on the rotational vibration of helical gears in consideration of the tooth separation phenomenon (a new stiffness function of helical involute tooth pair). *Journal of mechanical design*, 117, 1995.
- [18] Y. Cai. Simulation on the Rotational Vibration of Helical Gears in Consideration of the Tooth Separation Phenomenon (A New Stiffness Function of Helical Involute Tooth Pair). *Journal of Mechanical Design*, 117(3):460–469, September 1995. American Society of Mechanical Engineers Digital Collection.
- [19] Y. Cai and T. Hayashi. The linear approximated equation of vibration of a pair of spur gears (theory and experiment). *Journal of mechanical design*, 116, 1994.
- [20] Niccolò Cappellini, Tommaso Tamarozzi, Bart Blockmans, Jakob Fiszer, Francesco Cosco, and Wim Desmet. Semi-analytic contact technique in a non-linear parametric model order reduction method for gear simulations. *Meccanica*, 53(1):49–75, January 2018.
- [21] Alexandre Carbonelli, Joël Perret-Liaudet, Emmanuel Rigaud, and Alain Le Bot. Particle Swarm Optimization as an Efficient Computational Method in order to Minimize Vibrations of Multimesh Gears Transmission. *Advances in Acoustics and Vibration*, 2011, June 2011.
- [22] Alexandre Carbonelli, Emmanuel Rigaud, and Joël Perret-Liaudet. Vibro-Acoustic Analysis of Geared Systems—Predicting and Controlling the Whining Noise. *In Automotive NVH Technology (pp. 63-79)*, 2016.
- [23] K. Carlberg, C. Bou-Mosleh, and C. Farhat. Efficient non-linear model reduction via a least-squares petrov–galerkin projection and compressive tensor approximations. *International Journal for Numerical Methods in Engineering*, 86(2):155–181, 2011.
- [24] P. G. Catera, F. Gagliardi, D. Mundo, L. De Napoli, A. Matveeva, and L. Farkas. Multi-scale modeling of triaxial braided composites for FE-based modal analysis of hybrid metal-composite gears. *Composite structures*, 182, 116-123, 2017.
- [25] P. G. Catera, D Mundo, A. Treviso, F. Gagliardi, and A. Visroli. On the design and simulation of hybrid metal-composite gears. *Applied Composite Materials*, 26(3), 817-833, 2019.
-

- [26] S. Cescotto and R. Charlier. Frictional contact finite elements based on mixed variational principles. *International Journal for Numerical Methods in Engineering*, 36(10)(10):1681–1701, 1993.
- [27] S. Cescotto and Y. Y. Zhu. Large strain dynamic analysis using solid and contact finite elements based on a mixed formulation; application to metal forming. *Journal of Materials Processing Technology*, 45(1-4)(1):657–663, September 1994.
- [28] L. Chang, G. Liu, and L. Wu. A robust model for determining the mesh stiffness of cylindrical gears. *Mechanism and Machine Theory*, 87,93-114, 2015.
- [29] Z. Chen, Z. Zhou, W. Zhai, and K. Wang. Improved analytical calculation model of spur gear mesh excitations with tooth profile deviations. *Mechanism and machine theory*, 149, 103838, 2020.
- [30] Zaigang Chen and Yimin Shao. Dynamic simulation of spur gear with tooth root crack propagating along tooth width and crack depth. *Engineering Failure Analysis*, 18(8)(8):2149–2164, December 2011.
- [31] ZaiGang Chen, WanMing Zhai, YiMin Shao, and KaiYun Wang. Mesh stiffness evaluation of an internal spur gear pair with tooth profile shift. *Science China Technological Sciences*,, 59(9):1328–1339, September 2016.
- [32] F Chinesta, A. Ammar, and E. Cueto. Proper generalized decomposition of multiscale models. *International Journal for Numerical Methods in Engineering*, 83(8-9):1114–1132, 2010.
- [33] F Chinesta, A. Ammar, and E. Cueto. Recent advances and new challenges in the use of the proper generalized decomposition for solving multidimensional models. *Archives of Computational methods in Engineering*, 17(4):327–350, 2010.
- [34] T. F. Conry and A. Seireg. A Mathematical Programming Technique for the Evaluation of Load Distribution and Optimal Modifications for Gear Systems. *Journal of Engineering for Industry*, 95(4):1115–1122, November 1973.

- 
- [35] C. G. Cooley, C. Liu, X. Dai, and R. G. Parker. Gear tooth mesh stiffness: A comparison of calculation approaches. *Mechanism and machine theory*, 105, 540-533, 2016.
- [36] R.R. Craig, C. Mervyn, and C. Bampton. Coupling of substructures for dynamic analyses. *AIAA Journal*, 6(7), 1314-1319, 1968.
- [37] R.R. Craig, C. Mervyn, and C. Bampton. Component mode synthesis methods using interface modes. application to structures with cyclic symmetry. *Computers Structures*, 79, 209-222, 2000.
- [38] T. Duan, J. Wei, A. Zhang, Z. Xu, and T. C. Lim. Transmission error investigation of gearbox using rigid-flexible coupling dynamic model: Theoretical analysis and experiments. *Mechanism and Machine Theory*, 157, 2021.
- [39] D.W Dudley. *Handbook of practical gear design*. 1984.
- [40] R.W. Freund. Model reduction methods based on krylov subspaces. *Acta Numerica*, 12, 267-319, 2003.
- [41] K. Funk and F. Pfeiffer. A time-stepping algorithm for stiff mechanical systems with unilateral constraints. *PAMM*, 2(1):228–229, 2003.
- [42] Pierre Garambois, Joël Perret-Liaudet, and Emmanuel Rigaud. NVH robust optimization of gear macro and microgeometries using an efficient tooth contact model. *Mechanism and Machine Theory*, 117:78–95, November 2017.
- [43] G. Gobat, A. Opreni, S. Fresca, A. Manzoni, and A. Frangi. Reduced order modeling of nonlinear microstructures through proper orthogonal decomposition. *Mechanical Systems and Signal Processing*, 171, 108864, 2022.
- [44] S. Greenhalgh, V Acary, and B. Brogliato. On preserving dissipativity properties of linear complementarity dynamical systems with the -method. *Numerische Mathematik*, 125(4):601–637, 2013.

- 
- [45] J. A. Greenwood, J. B. P. Williamson, and Frank Philip Bowden. Contact of nominally flat surfaces. *Proceedings of the Royal Society of London. Series A. Mathematical and Physical Sciences*, 295(1442):300–319, December 1966. Royal Society.
- [46] R. W. Gregory, S. L. Harris, and R. G. . Munro. Dynamic behaviour of spur gears. *Proceedings of the Institution of Mechanical Engineers 178*, pp. 207-226, 1963.
- [47] D.F. Griffiths and J. Lorenz. An analysis of the petrov—galerkin finite element method. *Computer Methods in Applied Mechanics and Engineering*, 14(1), 39-64, 1978.
- [48] E.J. Grimme. Krylov projection methods for model reduction. *PhD thesis, Citeseer*, 1997.
- [49] A. Grolet and F. Thouverez. On the use of the proper generalised decomposition for solving nonlinear vibration problems. *ASME International Mechanical Engineering Congress and Exposition, American Society of Mechanical Engineers*, Vol. 45202, pp. 913-920, 2022.
- [50] G.V. Groll and D.J. Emins. The harmonic balance method with arc-length continuation in rotor/stator contact problems. *Journal of Sound and Vibration*, 241(2), 223–233, 2001.
- [51] M. Gruin. Dynamique non-linéaire d’une roue de turbine basse pression soumise à des excitations structurales d’un turboréacteur. *PhD thesis, Ecole centrale de Lyon*, 2012.
- [52] B. Guilbert, P. Velex, and P. Cutili. Static and dynamic analyses of thin-rimmed gears with holes. *VDI, International Conference on Gears*, pages 623–633, 2017.
- [53] B. Guilbert, P. Velex, and P. Cutili. Quasi-static and dynamic analyses of thin-webbed high-speed gears: Centrifugal effect influence. *Proceedings of the Institution of Mechanical Engineers, Part C: Journal of Mechanical Engineering Science*, 233(21-22), 7282-7291, 2019.
- [54] B. Guilbert, P. Velex, D. Dureisseix, and P. Cutili. Modular hybrid models to simulate the static and dynamic behaviour of high-speed thin-rimmed gears. *Journal of Sound and Vibration*, 438, 353-380, 2019.
- [55] B. Guilbert, P. Velex, D. Dureisseix, and P. Cutili. A Mortar-Based Mesh Interface for Hybrid Finite-Element/Lumped-Parameter Gear Dynamic Models—Applications to Thin-

- Rimmed Geared Systems. *Journal of Mechanical Design*, 138(12), December 2016. American Society of Mechanical Engineers Digital Collection.
- [56] ROBERT J. Guyan. Reduction of stiffness and mass matrices. *AIAA Journal*, 3(2), 380-380, May 1965.
- [57] K. H. Ha, J. P. Hong, G. T. Kim, K. C. Chang, and J. . Lee. Orbital analysis of rotor due to electromagnetic force for switched reluctance motor. *IEEE Transactions on Magnetics*, 36(4), 1407-1411, 2000.
- [58] E. Hairer, S.P. Norsett, and G. Wanner. Solving ordinary differential equations i, nonstiff problems. *Springer*, 2000.
- [59] E. Hairer and G. Wanner. Solving ordinary differential equations ii, stiff and differential-algebraic problems.. *Springer*, 2002.
- [60] S. Han and B. Feeny. Application of proper orthogonal decomposition to structural vibration analysis. *Mechanical Systems and Signal Processing*, 17(5):989–1001, 2003.
- [61] L. Harris. Dynamic loads on the teeth of spur gears. *Proceedings of the Institution of Mechanical Engineers 172*, 1958.
- [62] O. Harris, P. Langlois, and A. Gale. Electric vehicle whine noise-gear blank tuning as an optimization option. *Gear Technology*, 2019.
- [63] O. Harris, P. Langlois, and A. Gale. Gear blank tuning as an optimization option. *Gear Technology*, pp.64-73, 2019.
- [64] Stephen L. Harris. Dynamic Loads on the Teeth of Spur Gears. *Proceedings of the Institution of Mechanical Engineers*, 172(1), 87-112, February 1958.
- [65] U. Hetmaniuk, R. Tezaur, and C. Farhat. Review and assessment of interpolatory model order reduction methods for frequency response structural dynamics and acoustics problems. *International Journal for Numerical Methods in Engineering*, 90(13), 1636-1662, 2012.

- 
- [66] L. Hou, Y. Lei, Y. Fu, and J. Hu. Effects of lightweight gear blank on noise, vibration and harshness for electric drive system in electric vehicles. *Proceedings of the Institution of Mechanical Engineers, Part K: Journal of Multi-Body Dynamics*, 234(3), 447-464, 2008.
- [67] D. R. Houser. User's guide for the osu load distribution program (ldp), shaft analysis program, and rmc. 2011.
- [68] M. Jean. The non-smooth contact dynamics method. *Computer Methods in Applied Mechanics and Engineering*, 177(3):235–257, 1999.
- [69] M. Jean, V. Acary, and Y. Monerie. Non-smooth contact dynamics approach of cohesive materials. *Philosophical Transactions of the Royal Society of London. Series A: Mathematical, Physical and Engineering Sciences*, 359(1789):2497–2518, 2001.
- [70] M. Jean, V. Acary, and Y. Monerie. Simulation of non-smooth mechanical systems with many unilateral constraints. *Proceedings ENOC-2005 Eindhoven*, 2005.
- [71] M. Jean and J.J. Moreau. Numerical aspects of the sweeping process. *Computer Methods in Applied Mechanics and Engineering*, 177(3):329–349, 1999.
- [72] M. Jean and J.J. Moreau. Facing the plurality of solutions in nonsmooth mechanics. nonsmooth/nonconvex mechanics with applications in engineering ii. *II. NNMAE*, 2006:3–12, 2006.
- [73] M. Jean and J.J. Moreau. Dynamics in the presence of unilateral contacts and dry friction: A numerical approach. *Unilateral Problems in Structural Analysis, volume 304 of International Centre for Mechanical Sciences*, 151–196, 2019.
- [74] M. Jean and J.J. Moreau. Unilaterality and dry friction in the dynamics of rigid body collections. *In Proceedings of Contact Mechanics International Symposium*, 31–48, 2019.
- [75] K. L. Johnson. *Contact Mechanics*. Cambridge University Press, August 1987.

- [76] I. T. Jolliffe and J. Cadima. Principal component analysis : a review and recent developments. *Philosophical Transactions of the Royal Society A : Mathematical, Physical and Engineering Sciences.*, 374(2065) :20150202, 2016.
- [77] A. Kahraman. Natural modes of planetary gear trains. *Journal of Sound and Vibration*, 173, p. 125-130, 1994.
- [78] A. Kahraman and G. W. Blankenship. Effect of Involute Tip Relief on Dynamic Response of Spur Gear Pairs. *Journal of Mechanical Design*, 121(2):313–315, June 1999.
- [79] A. Kahraman and R. Singh. Interactions between time-varying mesh stiffness and clearance non-linearities in a geared system. *Journal of Sound and Vibration*, 146, p. 135-156, 1991.
- [80] T.R. Kane. Dynamics of nonholonomic systems. *Transactions of the ASME*, 28,p.574-578, 1961.
- [81] A. Karhaman, H.N. Ozguven, D.R. Houser, and J. Zakarajsek. Dynamic analysis of geared rotors by finite elements. *American Society of Mechanical Engineers.*, 114, p. 507-514, 1992.
- [82] K. Karhunen. Über lineare methoden in der wahrscheinlichkeitsrechnung. 1947.
- [83] S. Kocak, H. U. Akay, and A. Ecer. Parallel Implicit Treatment of Interface Conditions in Domain Decomposition Algorithms. *In Parallel Computational Fluid Dynamics 1998 (pp. 353-360)*, pages 353–360, January 1999.
- [84] G Koffel, F Ville, C Changenet, and P Velez. Investigations on the power losses and thermal effects in gear transmissions. *Proceedings of the Institution of Mechanical Engineers, Part J: Journal of Engineering Tribology*, 223(3), 469-479, 2009.
- [85] R. Kohler, A. Pratt, and A. M. . Thompson. Dynamics and noise of parallel axis gearing. *Proceedings of the Institution of Mechanical Engineers.*, 184, 111-121, 1969-1970.
- [86] J. A. Korta and D. Mundo. Multi-objective micro-geometry optimization of gear tooth supported by response surface methodology. *Mechanism and machine theory*, 109, 278-295, 2017.
- [87] B. Kramer and K.E. Willcox. Nonlinear model order reduction via lifting transformations and proper orthogonal decomposition. *AIAA Journal*, 57(6), 2297-2307, 2019.

- [88] Syuhei Kurokawa, Yasutsune Ariura, and Masaru Ohtahara. Transmission errors of cylindrical gears under load - influence of tooth profile modification and tooth deflection. *American Society of Mechanical Engineers, Design Engineering Division (Publication) DE*, 88:213–217, December 1996.
- [89] P. Ladeveze. Nonlinear computational structural mechanics : New approaches and non-incremental methods of calculation. *Mechanical Engineering Series. Springer-Verlag*, 1980.
- [90] S. Lammens, W. Heylen, and P. Sas. Modal analysis theory and testing. *PMA, KU Leuven, Faculty of Engineering, Department of Mechanical Engineering*, 14(1), 39-64, 2012.
- [91] T. A. Laursen and B. N. Maker. An augmented Lagrangian quasi-Newton solver for constrained nonlinear finite element applications. *International Journal for Numerical Methods in Engineering*, 38(21)(21):3571–3590, 1995.
- [92] V. Lenaerts, G. Kerschen, and J.C. Golinval. Proper orthogonal decomposition for model updating of non-linear mechanical systems. *Mechanical Systems and Signal Processing*, 15(1), 31-43, 2001.
- [93] J Lin and R.G. Parker. Analytical characterization of the unique properties of planetary gear free vibration. *Proceedings of the Institution of Mechanical Engineers*, p. 316-321, 1999.
- [94] F. L. Litvin, R. N. Goldrich, J. J. Coy, and E. V. . Zaretsky. Kinematic precision of gear trains. *Journal of Mechanisms Transmissions and Automation in Design, Transactions of ASME.*, 105, 317-326, 1983.
- [95] M. Loève. Probability theory : foundations, random sequences. 1955.
- [96] D. Lu, Y. Su, and Z. Bai. Stability analysis of the two-level orthogonal arnoldi procedure. *SIAM Journal on Matrix Analysis and Applications.*, 2016.
- [97] W. D. Mark. Tooth-meshing-harmonic static-transmission-error amplitudes of helical gears. *Mechanical systems and signal processing*, 98, 506-533, 2018.
- [98] G. W. Michalec. Precision gearing : theory and practice. *Wiley and sons, New York*, 1966.

- [99] R.G. Munro, N. Yildirim, and D.M. Hall. Optimum profile relief and transmission error in spur gears. *Gearbox noise and vibration*, (13):35–42, 1990.
- [100] A.A. Muravyov and S.A. Rizzi. Determination of nonlinear stiffness with application to random vibration of geometrically nonlinear structures. *Computers and Structures.*, 15,p. 1513-1523, 2003.
- [101] A. Mélot, Y. Benaïcha, E. Rigaud, J. Perret-Liaudet, and F. Thouverez. Effect of gear topology discontinuities on the nonlinear dynamic response of a multi-degree-of-freedom gear train. *Journal of Sound and Vibration*, 516 :116495,, 2022.
- [102] Jessica Neufond, Enora Denimal, Emmanuel Rigaud, Jöel Perret-Liaudet, and Alexandre Carbonelli. Whining noise computation of a planetary gear set induced by the multi-mesh excitations. *Proceedings of the Institution of Mechanical Engineers, Part C: Journal of Mechanical Engineering Science*, 233(21-22):7236 – 7245, 2019.
- [103] B. Ničeno and K. Hanjalić. Large eddy simulation (LES) on distributed memory parallel computers using an unstructured finite volume solver. *Parallel Computational Fluid Dynamics CFD 2000 Conference (p. 457), North-Holland*, January 2001.
- [104] A. Nouy. A generalized spectral decomposition technique to solve a class of linear stochastic partial differential equations. *Computer Methods in Applied Mechanics and Engineering*, 196(45-48):4521–4537, 2010.
- [105] H. Opitz and E. J. Richards. A discussion on the origin and treatment of noise in industrial environments - Noise of gears. *Philosophical Transactions of the Royal Society of London. Series A, Mathematical and Physical Sciences*, 263(1142):369–380, December 1968.
- [106] M. Papadrakakis, V. Papadopoulos, G. Stefanou, and V. Plevris. Model order reduction in structural dynamics. *VII European Congress on Computational Methods in Applied Sciences and Engineering*, 2016.
- [107] K. Pearson. On lines and planes of closest fit to systems of points in space. *The London, Edinburgh, and Dublin Philosophical Magazine and Journal of Science*, 2(11):559–572, 1901.

- 
- [108] J. Perret-liaudet. Etude des mécanismes de transfert entre l'erreur de transmission et la réponse dynamique des boîtes de vitesses d'automobile. *Doctoral dissertation, Ecully, Ecole centrale de Lyon.*, 1992.
- [109] E. P. Petrov and D. J. Ewins. Analytical Formulation of Friction Interface Elements for Analysis of Nonlinear Multi-Harmonic Vibrations of Bladed Disks. *J. Turbomach*, 125(2)(2):364–371, April 2003.
- [110] F. Pfeiffer and C. Glocker. Multibody dynamics with unilateral contacts. *Wiley*, 1996.
- [111] S.S. Ravindran. A reduced-order approach for optimal control of fluids using proper orthogonal decomposition. *International journal for numerical methods in fluids*, 34(5), 425-448, 2000.
- [112] E. Rigaud and D. Barday. Modelling and analysis of static transmission error. Effect of wheel body deformation and interactions between adjacent loaded teeth. *Proceedings of the 4th World Congress on Gearing and Power Transmission, Paris, Vol. 3, 1999, pp.1961-1972*, January.
- [113] D.J. Rixen. A dual craig-bampton method for dynamic substructuring. *Journal of Computational and applied mathematics*, 168, 383-391, 2004.
- [114] D. Rémond. Contribution à l'étude et l'analyse expérimentale du bruit d'engrènement. développement et application de la transformée en ondelettes rapide. *PhD thesis, INSA de Lyon.*, 1991.
- [115] Didier Rémond, Philippe Velex, and Jean Sabot. Comportement dynamique et acoustique des transmissions par engrenages : synthèse bibliographique. *p. 127, CETIM*, 1993.
- [116] P. Sainsot, P. Velex, and O. Duverger. Contribution of gear body to tooth deflections - A new bidimensional analytical formula. *J. Mech. Des.*, 126(4):748–752, 2004.
- [117] Loïc Salles, Bernard Staples, Norbert Hoffmann, and Christoph Schwingshackl. Continuation techniques for analysis of whole aeroengine dynamics with imperfect bifurcations and isolated solutions. *Nonlinear Dynamics*, 86(3)(3):1897–1911, November 2016.

- 
- [118] M. Sánchez, M. Pleguezuelos, and J. I. Pedrero. Influence of profile modifications on meshing stiffness, load sharing, and transmission error of involute spur gears. *Mechanism and machine theory*, 139, 506-525, 2019.
- [119] Roger A. Sauer. Enriched contact finite elements for stable peeling computations. *International Journal for Numerical Methods in Engineering*, 87(6)(6):593–616, 2011.
- [120] D. Schurr, P. Holzwarth, and P. Eberhard. Investigation of dynamic stress recovery in elastic gear simulations using different reduction techniques. *Computational mechanics*, 2018.
- [121] A. Shabana. Dynamics of multibody systems. *4th edition, Cambridge University Press*, 2013.
- [122] Shadi Shweiki, Antonio Palermo, and Domenico Mundo. A Study on the Dynamic Behaviour of Lightweight Gears. *Shock and Vibration*, 2017, October 2017.
- [123] Shadi Shweiki, Ali Rezayat, Tommaso Tamarozzi, and Domenico Mundo. Transmission Error and strain analysis of lightweight gears by using a hybrid FE-analytical gear contact model. *Mechanical Systems and Signal Processing*, 123, 573-590, January 2019.
- [124] J. C. Simo and T. A. Laursen. An augmented lagrangian treatment of contact problems involving friction. *Computers & Structures*, 42(1), 97-116(1), 1992.
- [125] Toshio Suzuki, Kiyohiko Umezawa, Haruo Houjoh, and Komang Bagiasna. Influence of Misalignment on Vibration of Helical Gear. *JSME international journal: bulletin of the JSME*,, 30(259), 201(477), 1987.
- [126] J. Szwedowicz, M. Kissel, B. Ravindra, and R. Kellerer. Estimation of Contact Stiffness and its Role in the Design of a Friction Damper. *In ASME Turbo Expo 2001: Power for Land, Sea, and Air. American Society of Mechanical Engineers Digital Collection*, July 2001.
- [127] M. S. Tavakoli and D. R. Houser. Optimum Profile Modifications for the Minimization of Static Transmission Errors of Spur Gears. *Journal of Mechanisms, Transmissions, and Automation in Design*, 108(1):86–94, March 1986.

- 
- [128] S. Thouviot. Optimisation multi-critères d'un système mécatronique en intégrant les problèmes vibro-acoustiques. *Ecole Centrale Paris*, 2013.
- [129] W.A. Tuplin. Gear-tooth stresses at high speed. *Proceedings of the Institution of Mechanical Engineers*, 163(1): 162-175, 1950.
- [130] S Ulaga, M Ulbin, and J Flašker. Contact problems of gears using Overhauser splines. *International Journal of Mechanical Sciences*, 41(4):385–395, April 1999.
- [131] K Umezawa, T Sato, and J Ishikawa. Simulation of rotational vibration of spur gear. *Bulletin of JSME*, 27(223), 102-109., 1984.
- [132] K. Umezawa, T. Suzuki, and T. Sato. Vibration of power transmission helical gears: approximate equation of tooth stiffness. *Bulletin of JSME*, 29(251), 1605-1611, 1986.
- [133] L. Vedmar and B. Henriksson. A general approach for determining dynamic forces in spur gears. *Journal of mechanical design*, 120, 1998.
- [134] P. Velez and F. Ville. An Analytical Approach to Tooth Friction Losses in Spur and Helical Gears—Influence of Profile Modifications. *Journal of Mechanical Design*, 131(10)(101008), September 2009.
- [135] S. M. Vijayakar. A combined surface integral and finite element solution for a three-dimensional contact problem. *International Journal for Numerical Methods in engineering*, 31(3), 525-545, 1991.
- [136] H. Vinayak and R. Singh. Multi-body dynamics and modal analysis of compliant gear bodies. *Journal of Sound and Vibration*, 210, 171-214, 1995.
- [137] H. Vinayak, R. Singh, and C. Padmanabhan. Linear dynamic analysis of multi-mesh transmissions containing external, rigid gears. *Journal of Sound and Vibration*, 185(1), 1995.
- [138] G. Virlez, O. Bruls, V. Sonneville, E. Tromme, P. Duysinx, and M. Gérardin. Contact model between superelements in dynamic multibody systems. *Proceedings of the ASME 2013 International Design Engineering Technical Conferences*, 2013.

- 
- [139] S. Walton, O. Hassan, and K. Morgan. Reduced order modelling for unsteady fluid flow using proper orthogonal decomposition and radial basis functions. *Applied Mathematical Modelling*, 37(20-21), 8930-8945, 2000.
- [140] J. Wang, R. Li, and X. Peng. Survey of nonlinear vibration of gear transmission systems. *Applied Mechanics Reviews*, 56, 309-329, 2003.
- [141] C. Weber and K. Banaschek. Formänderung und Profilrucknahme bei Gerad- und Schragverzahnten Antriebstechnik. Vieweg, Braunschweig, 11, 4, 1953.
- [142] D. B. Welbourn. Fundamental knowledge of gear noise: a survey, 1979. No. IMechE-C117/79.
- [143] K. Willcox and J. Peraire. Balanced model reduction via the proper orthogonal decomposition. *AIAA journal*, 40(11):2323–2330, 2002.
- [144] J. Wittenburg. Dynamics of systems of rigid bodies. 28,p.574-578, 1977.
- [145] Peter Wriggers. Discretization, Large Deformation Contact. *Computational Contact Mechanics (pp. 225-307)*. Springer, Berlin, Heidelberg, 2006.
- [146] Peter Wriggers. Discretization of the Continuum. *In Computational Contact Mechanics (pp. 157-182)*. Springer, Berlin, Heidelberg, 2006.
- [147] Peter Wriggers. Discretization, Small Deformation Contact. *Computational Contact Mechanics (pp. 183-224)*. Springer, Berlin, Heidelberg, 2006.
- [148] Peter Wriggers. Introduction to Contact Mechanics. *Computational Contact Mechanics (pp. 11-29)*. Springer, Berlin, Heidelberg, 2006.
- [149] Ling Xiang and Nan Gao. Coupled torsion–bending dynamic analysis of gear-rotor-bearing system with eccentricity fluctuation. *Applied Mathematical Modelling*, 50:569–584, October 2017.
- [150] C. Xie, L. Hua, X. Han, J. Lan, X. Wan, and X. Xiong. Analytical formulas for gear body-induced tooth deflections of spur gears considering structure coupling effect. *International Journal of Mechanical sciences*, 148,174-190, 2018.
-

- 
- [151] B. S. Yang, Y. H. Kim, and B. G. . Son. Instability and imbalance response of large induction motor rotor by unbalanced magnetic pull. *Journal of Vibration and Control*, 10(3), 447-460, 2004.
- [152] D. C. H. Yang and J. Y. Lin. Hertzian Damping, Tooth Friction and Bending Elasticity in Gear Impact Dynamics. *Journal of Mechanisms, Transmissions, and Automation in Design*, 109(2):189–196, June 1987.
- [153] Kiyoshi Yonekawa and Mutsuto Kawahara. Analysis of Tidal Flow Using Kalman Filter Finite Element Method with Domain Decomposition Method. *In Computational Mechanics—New Frontiers for the New Millennium (pp. 155-160)*. Elsevier, January 2001.
- [154] I. Yuruzume, H. Mizutani, and T. Tsubuku. Transmission Errors and Noise of Spur Gears Having Uneven Tooth Profile Errors. *Journal of Mechanical Design*, 101(2):268–273, April 1979.
- [155] P. Ziegler and P. Eberhard. Simulative and experimental investigation of impacts on gear wheels. *Computer Methods in Applied Mechanics and Engineering.*, 197,p. 4653-4662, 2008.
- [156] H. Özgüven and D. R. Houser. Mathematical models used in gear dynamics—A review. *Journal of Sound and Vibration*, 121(3):383–411, March 1988.

## **AUTORISATION DE SOUTENANCE**

Vu les dispositions de l'arrêté du 25 mai 2016 modifié par l'arrêté du 26 août 2022,

Vu la demande des directeurs de thèse

Messieurs F. THOUVEREZ et J. PERRET-LIAUDET

et les rapports de

M. J-L. DION

Professeur - Supméca Saint-Ouen, Vibration Acoustique et Structures, 3 rue Fernand Hainaut,  
93400 SAINT OUEN

et de

M. A. KAHRAMAN

Professeur - The Ohio State University, Department of Mechanical and Aerospace Engineering,  
201 W. 19th Avenue Columbus, OH 43210, USA

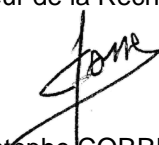
**Monsieur BENAICHA Youness**

est autorisé à soutenir une thèse pour l'obtention du grade de **DOCTEUR**

**Ecole doctorale** Mécanique, Energétique, Génie Civil, Acoustique

Fait à Ecully, le 2 mai 2023

Pour le directeur de l'Ecole centrale de Lyon  
Le directeur de la Recherche



Christophe CORRE